LABEL-FREE REFRACTIVE INDEX SENSING WITH FREE-SPACE COUPLED PHOTONIC CRYSTAL SLABS

by

YONGHAO LIU

Presented to the Faculty of the Graduate School of
The University of Texas at Arlington in Partial Fulfillment
of the Requirements
for the Degree of

DOCTOR OF PHILOSOPHY

THE UNIVERSITY OF TEXAS AT ARLINGTON
December 2017

Acknowledgements

First of all, I would like to thank my advisors Prof. Weidong Zhou and Prof. Yuze Sun for their guidance, support, patience and motivation throughout my graduate study here at UT Arlington. It is very lucky for me to have two advisors, and from them I have learned a lot about doing research and how to solve problems more efficiently and effectively.

I would also like to thank the other members of my dissertation committee: Prof. Robert Magnusson, Prof. Michael Vasilyev, and Prof. Jung-Chih Chiao for giving me valuable comments on my proposal and dissertation.

I am indebted to some senior students in the group who guide me in my research: Dr. Deyin Zhao, Dr. Hongjun Yang, Dr. Yichen Shuai and Dr. Arvinder Chadha. I would also like to thank some other group members for extensive discussion and cooperation: Dr. Shuling Wang, Dr. Shihchia Liu, Dr. Laxmy Menon, Dr. Xiaochen Ge, Dr. Wenjuan Fan, Dr. Jin Huang, Zhonghe Liu, Akhil Raj Kumar Kalapala, Priyanka Biswas, Prithviraj Palit, Han Zhang, and Chen Zhang.

I am also indebted to all the staffs at UT Arlington Nanfab: Dr. Nader Hozhabri, Dennis Bueno, Richard Kevin Chambers and Mick Nguyen.

I spent a few months in the MRC of UT Austin for device fabrication, where I got a lot of help from many other users and friends. Special thanks go to Dr. Xiaoling Wei who is very kind to let me stay in his apartment for a few months. I really appreciate his help. I also thank many staffs in MRC for their help: William Ostler, William James, Johnny Johnson, Ricardo Garcia, David Farnsworth, and Dr. Marylene Palard.

I am grateful for the funding support from NSF, ARO, and UTA EGTA scholarship. I would like to thank Dr. Howard Russell for hiring me as a GTA for his class, and Gail Paniuski for her administrative support for my study in EE department.

I would like to thank other friends who helped me in graduate school and their friendship: Dr. Jiangyan Wang, Dilin Wang, Dr. Qinggong Tang, Dr. Hai Yan, Dr. Gensheng Zhang, Dr. Nan Zhang, Dr. Chengdong Xu and many others whom I forget to mention here.

Last but not least, I would like to thank my parents and the rest of my family. I thank them for their love and support in my life. They are the most important people to me, no matter where I am and who I am.

November 8, 2017

Abstract

LABEL-FREE REFRACTIVE INDEX SENSING WITH FREE-SPACE COUPLED PHOTONIC CRYSTAL SLABS

Yonghao Liu, PhD

The University of Texas at Arlington, 2017

Supervising Professors: Weidong Zhou, Yuze Sun

Label-free optical resonance sensors can detect small changes of refractive index (RI), which could be used for biochemical molecular detection, drug screening or gas detection. One of the most critical parameters in these sensors is the sensor detection limit (*DL*). Reducing *DL* can be achieved by increasing the resonance quality factors (*Q*) and the spectral sensitivity (*S*). Another critical research challenge in these sensors is the sensing specificity.

In this thesis, based on Fano resonance principle in two-dimensional photonic crystal slabs (PCS) and the integration with gas separation columns, we investigated various free-space coupled on-chip optical resonance sensors for both liquid sensing and gas sensing/separation.

In Chapter 1, an introduction is given about the background and motivation of our work. The characteristics of Fano resonances in the PCS structures are discussed, followed by the discussions on bound state in the continuum (BIC) in 1D and 2D single layer PCS at wave vector $\boldsymbol{k} \approx 0$ and some discrete $\boldsymbol{k}$ points. Fabry-Perot BICs in coupled bi-layer PCS are also introduced. The state-of-the-art are also reviewed for various sensor configurations, such as surface plasmon resonance (SPR) sensors, ring resonators, grating, defect-free PCS, defect PCS cavity and slotted PCS.

In Chapter 2, a few PCS structures were proposed and designed to achieve high *Q* factor and high sensitivity simultaneously, based on bright guided resonance and quasi-BIC modes in single-layer and bi-layer PCS.

In Chapter 3, the fabrication processes were described, for both single-layer and double-layer PCS sensors. Polydimethylsiloxane (PDMS) microfluidic chambers were also built on the PCS devices for device characterization.

In Chapter 4, liquid sensing experimental results were presented for both single-layer and bi-layer PCS sensors. Various concentrations of ethanol/deionized water were employed to characterize the bulk sensitivities. Bright guided resonance and quasi-BIC modes in single-layer PCS and double-layer PCS are utilized for sensing. Quasi-BIC modes provide higher *Q* factor than regular bright guided resonance.

In Chapter 5, PCS sensors chemical vapor detection were introduced, where the PCS surface is coated with a layer of vapor-sensitive polymer. Vapor molecules will be adsorbed in the polymer layer and cause changes in its thickness and refractive index, which leads to the resonance spectral shift. The thickness of the polymer layer will affect the sensitivity and response time of the PCS sensors, which were investigated theoretically and experimentally. In the first integration scheme, the PCS sensor was integrated with a glass chamber and tested with hexane and ethanol vapors. In the second integration scheme, the PCS sensor was firstly transferred onto a glass substrate and then bonded with microfabricated silicon separation columns. The integrated device was tested with four different vapors: hexane, ethanol, benzene and toluene. The PCS sensitivity to different vapors and column separation of different vapors are demonstrated.

Finally a conclusion is given in Chapter 6, with major accomplishments summarized, along with suggestions on possible future research work.

Table of Contents

List of Illustrations

List of Tables

Chapter 1

Introduction

1.1 Motivation

Optical biosensors have wide applications in biomedical research, heath care, environmental monitoring, homeland security and battle field. They are immune to electromagnetic interference and can perform remote sensing. Optical biosensing can be divided into fluorescence-based detection and label-free detection, as illustrated in Figure 1-1(a). In fluorescence-based detection, the target molecules are labeled with fluorescent tags, and the fluorescence intensity indicates the existence of the target molecules. Fluorescence-based biosensors can provide high sensitivities, but it requires extensive and time-consuming labeling process. Label-free optical sensing can provide real time and rapid analysis and require minimal sample preparation without interfering with the function of biomolecule [1-3]. Label-free sensor could either detect refractive index (RI) change, absorption change or Raman signal induced by the presence of analyte [2].

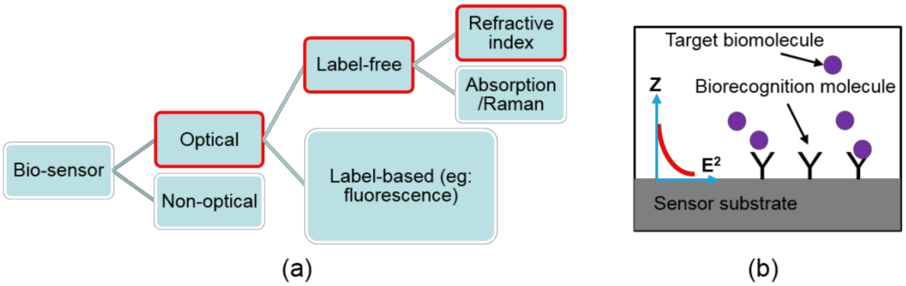

Figure 1-1: (a) Different types of biosensors classified by principles. (b) A sketch of a typical optical refractive index biosensor.

RI-based sensor can find applications in biochemical molecular interaction [4-8], drug detection[9], gas detection[10-12]. RI-based sensors can detect both the RI of bulk solution [13-18] and RI change due to molecule binding [4, 7]. A general configuration of RI-based biosensor is shown in Figure 1-1(b). A layer of biorecognition molecules, such as antibodies or aptamers, are immobilized on the sensor surface. The chamber above the sensor is filled with the buffer solution, and the target molecules is introduced and binds to the biorecognition molecules, which replaces the buffer solution molecules. The refractive index of the target molecules is different from the buffer solution molecules, which can be detected as a transduction signal for the sensor, due to the evanescent field which decay exponentially in z direction to around several hundred nanometers above the sensor surface.

In sensor development, achieving high sensitivity (*S*) is very important to measure small changes in the transduction signal. We can define the detection limit (*DL*) as the minimum resolvable refractive index change for a RI-based sensor, which is typically in units of refractive index units (RIU). *DL* is related to the resolution of the system and the sensitivity, and it can be estimated by $DL = 3\sigma / S$, where 3σ is the system noise. Sensor detection limit can fully describe the performance of sensor, which can be improved by increasing *S* or reducing the system noise 3σ [1].

We can define optical overlap integral f as the ratio of electric field energy in the analyte region to the total energy for a given mode [13, 14].

$$f = \left. \int_{V_{liquid}} \varepsilon |E|^2 \, dv \middle/ \int_{V_{total}} \varepsilon |E|^2 \, dv \right. \tag{1.1}$$

where ε is the dielectric constant of the material. The bulk spectral sensitivity *S* is related to the optical overlap integral f and the resonance wavelength λ_0 by:

$$S = \Delta\lambda_0 / \Delta n_{liquid} = \lambda_0 f / n_{liquid} \tag{1.2}$$

Therefore it is clear that a large f value will give higher bulk sensitivity because of larger field overlap with the analyte. System noise 3*σ* is given by [1]:

$$3\sigma = \frac{\Delta\lambda_{FWHM}}{1.5(SNR)^{0.25}} = \frac{\lambda_0 / Q}{1.5(SNR)^{0.25}} \tag{1.3}$$

Where *Q* is the quality factor of the cavity resonance, and *SNR* is the signal noise ratio. Therefore *DL* can be lowered by designing a resonant cavity with high quality factor and large mode overlap with the analyte.

1.2 Photonic crystal

Photonic crystal (PhC) is an optical nanostructure with periodic high and low dielectric constant [19]. It can be divided into one-dimensional (1D) PhC, two-dimensional (2D) PhC and three-dimensional (3D) PhC.

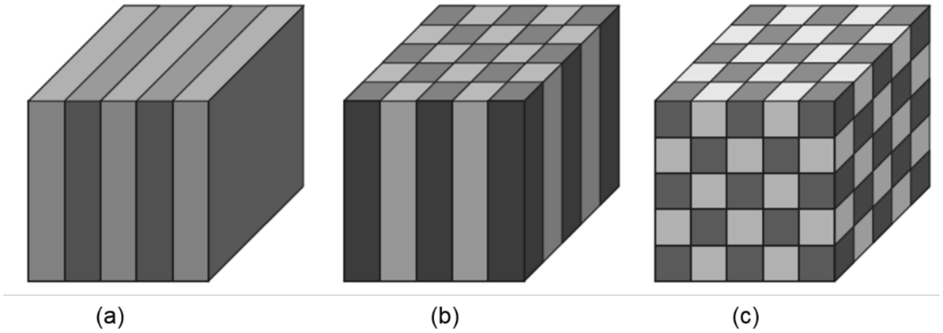

Figure 1-2: Schematics of (a) One-dimensional (1D) photonic crystal; (b) Two-dimensional (2D) photonic crystal; (c) Three-dimensional (3D) photonic crystal. [19] Each color represents a different index of refraction.

1D PhC has two alternating materials with different dielectric constant, as shown in Figure 1-2(a). 2D PhC consists of a dielectric crystal pattern which is periodic through a two-dimensional plane and homogeneous in the third dimension, as sketched in Figure

1-2(b). 3D PhC has periodic dielectric constant in three directions, as indicated in Figure 1-2(c). Its fabrication has no inheritable semiconductor industry techniques, and it can be formed by self-assembly process.

A photonic band is a range of light frequencies that are able to pass through the PhC, while a photonic bandgap refers to the frequency range that are forbidden passing through the PhC [20]. By designing the geometry of lattice structure, and selecting the materials, we can have a large control of the propagation of the light in the PhC structure. 2D photonic crystal slabs (PCSs) are an important class of PhC structures, as shown in Figure 1-3(a). They are quasi-2D structures where the light is confined due to both in-plane 2D photonic bandgap confinement and out-of-plane waveguide index confinement.

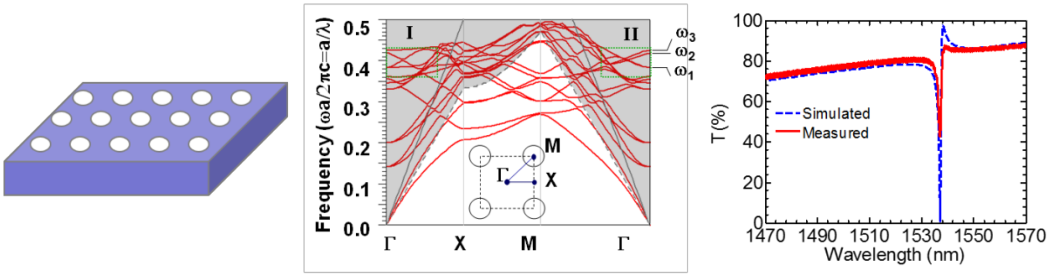

(a) (b) (c)

Figure 1-3: (a) A schematic of 2D-PCS. (b) Simulated dispersion curves for square lattice silicon 2D-PCS on low index glass substrate, where *r*/*a* = 0.19, *t*/*a* = 0.417. [21] (c) Simulated and measured transmission spectra of a silicon PCS on glass substrate, where *a* = 770 nm, *r* = 73 nm, *t* = 245 nm. [22]

Photonic-crystal fiber (PCF) is a new class of optical fiber based on the properties of 2D PhC [20]. PCF has large dimension in the third direction, typically a few centimeters or meters, while 2D PCS has a thickness comparable to the lattice constant. 2D PCS can be integrated with other photonic components for photonic integrated circuits (PICs), and it can be fabricated with standard CMOS process. A simulated dispersion plot is shown in Figure 1-3(b) for 2D square lattice air holes in silicon slab on glass substrate, with *r*/*a* = 0.19, *t*/*a* = 0.417 [21]. The dashed line is the light line. The 2D PCS support in-plane guided modes which lie below the light line; they are completely confined by the slab without coupling to external radiations.

Similar to the guided mode, the optical field of a guided resonance is strongly confined within the slab. However, the resonance can couple to external radiation [23]. These guided mode resonance operate above the light line region, as shown with shaded area in Figure 1-3(b). The reflection or transmission spectra are typically in an asymmetric line shape, as shown in Figure 1-3(c). The resonance modes (eg: at ω_1, ω_2, ω_3) arise from the coupling of in-plane discrete guided modes with the vertical continuum free-space radiation mode [24], and they are one type of Fano resonances [25]. The resonance can be very sharp with high quality factor, which can be used for bandpass filters [22-24, 26].

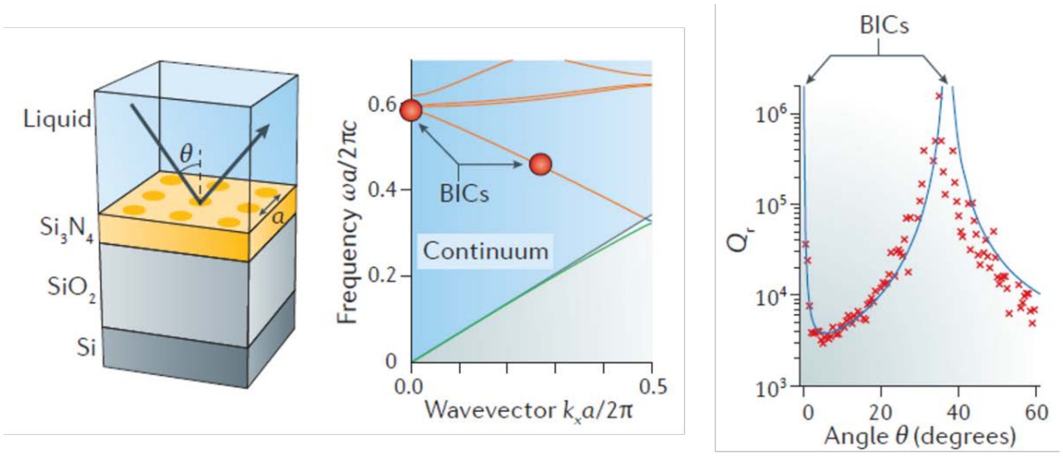

(a) (b) (c)

Figure 1-4: (a) A schematic of the Si_3N_4 PCS. (b) The photonic band structure, with two types of BICs labeled with red circles. (c) The radiative quality factor, Q_r, diverges to infinity at the two BICs for experimental data (red crosses) and theory (blue line) [27].

Fano resonances in the PCS structures could be excited by the external light that is vertically incident on the PCS efficiently [23, 24, 28, 29]. A bound state in the continuum (BIC) are waves that coexist with the continuous radiation spectrum, remaining perfectly confined without any radiation [27, 30]. BICs exist in 2D Si_3N_4 PCS at wave vector ***k*** ≈ 0 and some discrete ***k*** points with infinite lifetime and infinite *Q,* as shown with red circles in Figure 1-4(b) [31-34]. Figure 1-4(c) shows that the quality factors of the resonance diverge to infinity at these discrete ***k*** values, which is a good indication of the existence of BIC.

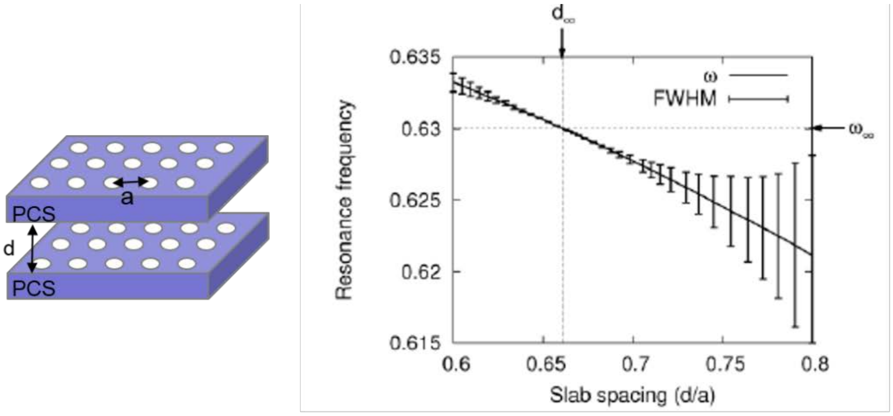

(a) (b)

Figure 1-5: (a) A schematic of the double layer PCS. (b) The resonance location and FWHM of the resonance for one double layer PCS, as a function of slab spacing *d/a*. [35]

Shown in Figure 1-5(a) is a schematic of a double layer PCS, with a separation distance of *d* between the two slabs. Fabry-Perot BICs can be formed in coupled bi-layer PCS by choosing an appropriate spacing between the two slabs [27, 34, 35]. As we can see from Figure 1-5(b), the full width half maximum (FWHM) $\Delta\omega$ of the resonance reduces to almost zero when the slab spacing is approaching d_∞, where the light is perfectly confined between the two slabs because the Fabry-Perot resonance between the two slabs is formed at the frequency for unity reflection. Since $Q = \omega_0/\Delta\omega$, the quality factor goes to infinity when $\Delta\omega$ is approaching zero.

Extremely high Q can be achieved when coupling to the perturbed BICs by tilting the light away from the surface-normal direction [23, 31, 32], or tuning the spacing between coupled bi-layer PCS [26, 34, 35]. These perturbed BICs can be called quasi-BICs modes and can be employed for applications of lasing, sensing and filtering [27].

1.3 State of the art

Researchers have investigated many different optical configurations for label-free refractive index sensing, including surface plasmon resonance (SPR), ring resonator, 1D grating, and PCS cavity.

1.3.1 SPR sensor

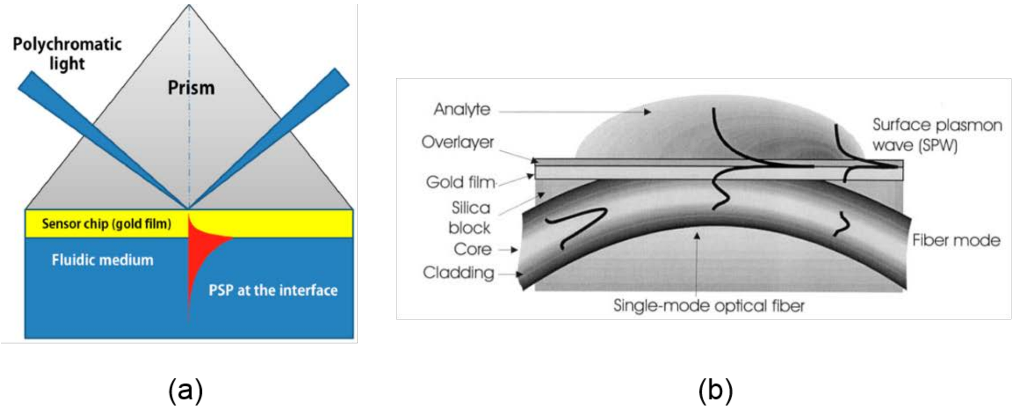

Figure 1-6: (a) Concept of a SPR biosensor based on prism coupling [36]. (b) Schematic of a SPR biosensor based on fiber coupling [37].

SPR sensor is probably the most successful one and has been commercialized due to its high sensitivity [36, 38-40]. A surface plasmon wave (SPW) is an electromagnetic wave that can propagate along the boundary between a dielectric and metal. A SPW is a transverse-magnetic (TM) wave, where the magnetic field is parallel to the plane of interface and perpendicular to the incident plane. It is characterized by the propagation constant β. Gold is the most common choice for the metal. The field of an SPW is confined at the metal-dielectric interface and decreases exponentially into both media. Because the majority of the light is distributed in the dielectric, the propagation constant of the SPW is very sensitive to the refractive index change in the dielectric. This is the fundamental principle for affinity SPR biosensors.

In a typical SPR sensor, biorecognition molecules are immobilized on one side of an gold-coated glass slide, and the target molecules in an aqueous buffer solution is injected to flow across the surface through the fluidic chamber, as shown in Figure 1-6(a). When target molecules bind to the biorecognition molecules, the refractive index changes in the dielectric. Excitation of an SPW by light can occur when its light vector along the metal surface matches that of the SPW, which can be satisfied by prism coupling, grating coupling, fiber coupling and waveguide coupling [38]. The prism coupling is shown in Figure 1-6(a) and fiber coupling is shown in Figure 1-6(b).

As shown in Figure 1-6(a), a light beam shines through a high refractive index prism and hits the gold surface, it is totally reflected if the incident angle is greater than the critical angle. At a specific resonant angle and wavelength, it will excite the SPW by matching the vector condition. The reflection spectrum will show a reflection dip if we scan the incident angle [36]. This resonant angle is sensitive to the refractive index of the dielectric, which can be used to track and monitor biomolecule interaction.

SPR biosensors have been widely studied for localized RI sensing [41, 42]. SPR biosensors can provide high sensitivity S >1000 nm/RIU but the large absorption in metal leads to low Q [37], which increases the ambiguity in determining the spectral resonance location in the presence of spectral noise [1].

1.3.2 Ring resonator

Ring resonators have been investigated for biochemical and chemical sensing because of its high Q factor [43-45]. The resonant optical mode forms due to total internal reflection of the light at the curved boundary. The resonant wavelength can be calculated from:

$$\lambda_m = 2\pi r n_{eff} \;/\; m \tag{1.4}$$

Where *r* is the radius of the ring, n_{eff} is the effective refractive index of the optical resonator mode, and *m* is an integer number representing the order of the longitudinal cavity mode.

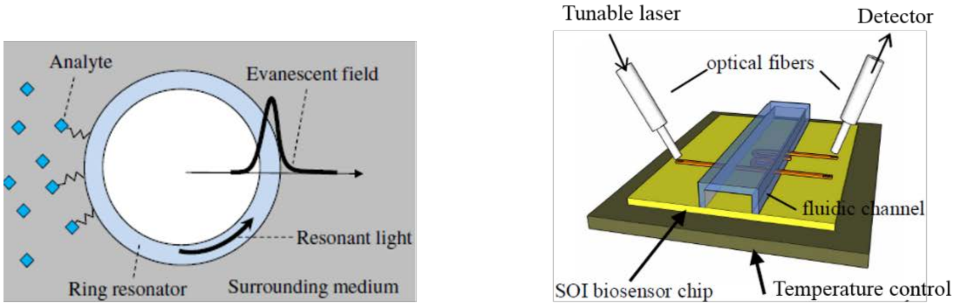

(a)

(b)

Figure 1-7: (a) Schematic of a ring resonator for biochemical and chemical sensing [43]. (b) Schematic of the test setup to characterize the ring resonator [44].

The circulating optical mode has an evanescent field which decays into the surrounding medium and interact with the analyte, as shown in Figure 1-7(a). Any small change of refractive index in the evanescent region will cause a change in the effective refractive index, n_{eff}, of the waveguide mode. By increasing the modal overlap with the sensing region, the sensitivity can be increased. A number of factors determine the cavity *Q* factor, including optical cavity loss, coupling loss, bend loss and scattering loss. The *Q* factor for a ring is typically in the range of 10,000 to 50,000. A schematic of the measurement setup is shown in Figure 1-7(b). A fluidic channel is mounted on the sensor chip. Input light from a tunable laser is coupled into the input waveguide through grating coupler, and the output light is collected with a photo detector through a grating coupler [44]. A typical sensitivity of 100-200 nm/RIU bulk sensitivity can be achieved with the ring resonator.

1.3.3 Grating

Label-free guided-mode resonance (GMR) grating biosensors have been investigated extensively in the last two decades [5, 6, 8, 46]. In 1992, Magnusson and Wang discussed GMR effect in grating structure and its possibility for biosensor application [29].

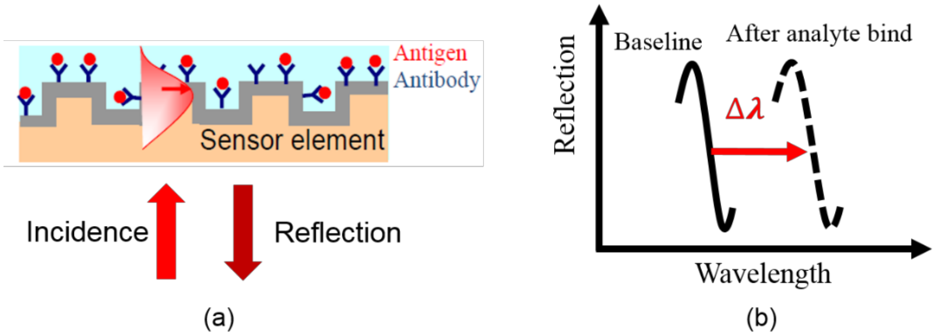

Figure 1-8: (a) Schematic of a grating sensor for biochemical sensing [8]. (b) Binding events produce spectrum shift of the resonance.

The GMR sensor uses a sub-wavelength grating waveguide structure which reflects only a narrow band of wavelength when a broadband incident light illuminate on the structure. It exhibits properties of both diffraction grating and waveguide and the leaky mode can couple to the external diffracted light. The resonant wavelength depends on the refractive indices of the composed material and the geometrical configuration, such as period, thickness and fraction of high-index region.

As shown in Figure 1-8(a), the binding interaction of an immobilized receptor (antibody) with an analyte (antigen) can interact with the guide mode resonance by changing the refractive index at the surface of the sensor. The refractive index change will induce a spectral shift of the GMR, as indicated in Figure 1-8(b). The grating structure is highly polarization dependent and it has different resonance with TE (electrical vector normal to the incident plane) and TM (magnetic vector normal to the incident plane) polarized source, which provides two concurrent sets of data to distinguish background noise from the specific biomolecule binding interaction [8].

1.3.4 Defect-free 2D PCS

2D PCS without defect has been studied for biochemical sensing recently, due to its simple test scheme and possibility to achieve simultaneous high *Q* or high *S* [13, 14, 47, 48]. Fano resonance in the 2D PCS are very sensitive to the refractive index at the PCS sensor, making them a good choice for biomolecule sensing.

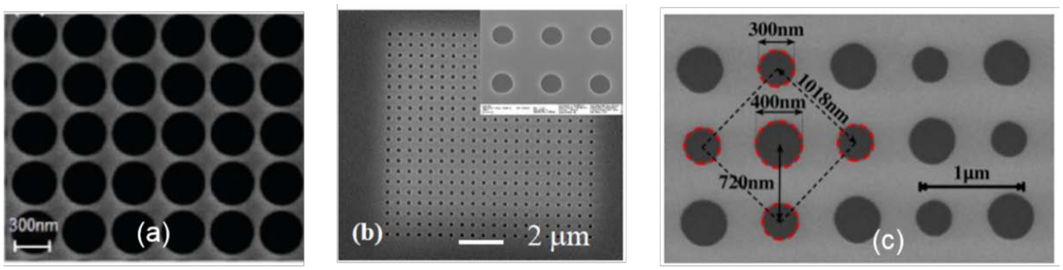

Figure 1-9: SEM images of (a) Suspended defect free PCS [47]; (b) Defect free PCS on glass substrate [48]; (c) Suspended defect free checkboard PCS [14].

Figure 1-9(a) shows a SEM image of a suspended Si_3N_4 PCS with large holes. This sensor achieved a sensitivity of 510 nm/RIU when two sides of the PCS can be accessed by analyte, while the quality factor is less than 100 [47]. Another configuration on glass substrate was investigated and it achieved a sensitivity of 130 nm/RIU and a quality factor of 180 [48], which is shown in Figure 1-9(b). A simultaneous high sensitivity and high *Q* has been achieved by modifying the lattice structure from square lattice to a checkboard lattice [14], as shown in Figure 1-9(c). The checkboard PCS was fabricated from Si_3N_4 and suspended in liquid solution to achieve high sensitivity of 800 nm/RIU. The *Q* factor was tested to be around 10,000 by small perturbation of the dark mode.

These defect-free 2D PCS are typically tested with a free-space incident beam normal to the 2D PCS surface. Either reflection or transmission spectrum can be tested to track the resonant location of the Fano resonance.

1.3.4 Defect PCS cavity and slotted PCS

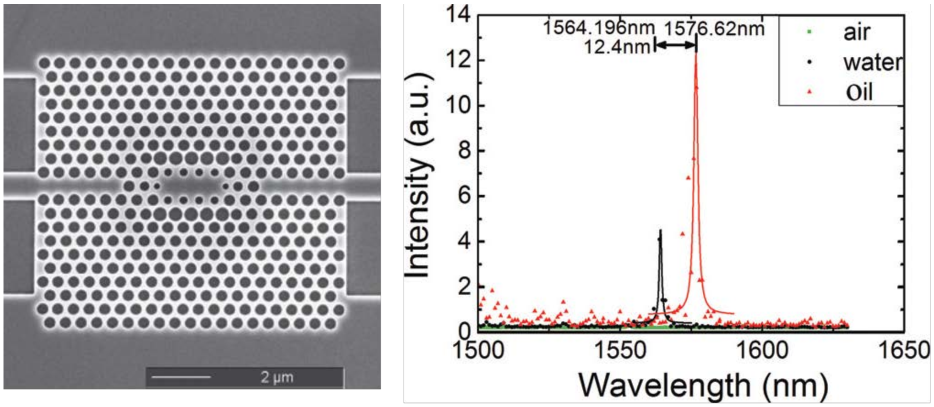

(a) (b)

Figure 1-10: (a) SEM image of a sensor device based on L3 PCS cavity. (b) Transmission spectra of the in-plane coupled light with air, water and oil ambient environment [49].

2D PCS exhibit band gaps for in-plane propagation and no modes are allowed within the bandgap. Localized mode within the gap is allowed when perturbing the lattice structure [19]. In a sense, we create a cavity that is effectively surrounded by reflecting walls. For example, we can remove three holes from the crystal at the center region and create a L3 cavity [49], as shown in Figure 1-10(a). A localized mode is created with a quality factor of 1,500 in water, as shown in Figure 1-10(b). The bulk sensitivity is found to be 103 nm/RIU by testing the transmission spectra in water and in oil. A few other papers also discussed the defect 2D PCS for sensing application [4, 50-53]. The quality factor of a few thousand can be achieved, but the sensitivity is typically around 100 to 150 nm/RIU due to small mode overlap with the analyte.

Sensitivities of the defect 2D PCS can be dramatically increased to 400-900 nm/RIU by designing a slot region in the PCS which confines the light and increases the light interaction with analyte [54-56]. Shown in Figure 1-11(a) is a slotted PCS cavity with a *Q* factor of 3,000 and a sensitivity of 500 nm/RIU [55]. A slotted parallel quadrabeam PCS cavity achieved a *Q* factor of 7,000 and a sensitivity of 450 nm/RIU [54], as shown in Figure 1-11(b).

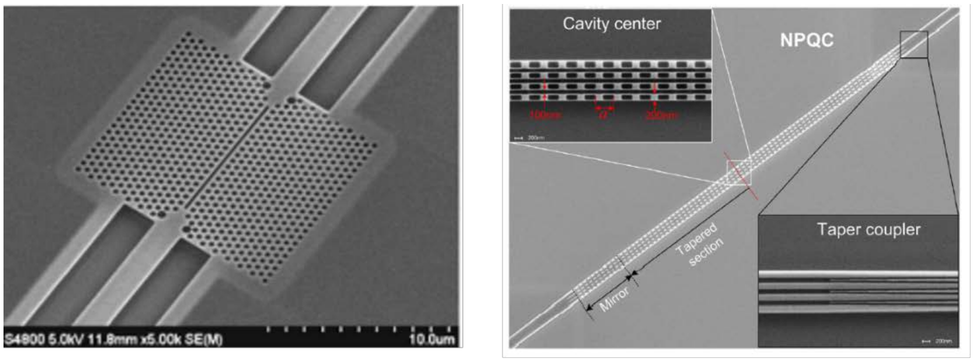

(a) (b)

Figure 1-11: SEM images of (a) Slotted PCS cavities [55]; (b) Nanoslotted parallel quadrabeam PCS cavity [54].

1.3.5 Summary

Table 1-1 summarizes different resonators in terms of quality factor, sensitivity and the incident light direction. SPR sensors have high sensitivity but suffer from low *Q* factor. Ring resonators have high *Q* and they are very promising platform to achieve on chip integration with in-plane light excitation and detection. Grating GMR sensor has been implemented for biosensing successfully, though its quality factor is not that high compared with defect PCS and 2D defect-free PCS. Localized and slotted PCS cavities can achieve high Q factors. However, they requires delicate alignment scheme and has low coupling efficiency from free space. The detection speed is greatly comprised due to the slow mass transport rate for the analyte to diffuse in and out of the confined nanoscale channels or localized cavity.

The work in this dissertation focuses on 2D defect free PCS. It can achieve high *Q* factor and high sensitivity. Meanwhile, the optical test can be done with out-of-plane incident light beam and it has large tolerance in terms of alignment of the beam onto the device. The detection speed is also fast, allowing for real-time measurement for biomedical, healthcare and industrial applications.

Table 1-1: Summary of state of the art for quality factor, sensitivity and incident light direction for different resonators.

Resonator	**Quality factor**	**Sensitivity (nm/RIU)**	**Light direction**
SPR	Low (<100)	High (10^3)	Oblique
Ring resonators	High (10^3-10^5)	Moderate (100-300)	In-plane
Grating	Moderate (100-10^3)	Moderate (100-300)	Out-of-plane
Defect PCS	High (10^3-10^4)	Moderate (100-200)	In-plane
Slotted PCS	High (10^3-10^4)	High (400-1500)	In-plane
Defect-free PCS	High (10^3-10^4)	High (100-800)	Out-of-plane

1.4 Organization of this dissertation

The chapters of this thesis are divided in two broad categories. Chapters 2-4 discuss the design, fabrication and characterization of 2D Si PCS for bulk liquid refractive index sensing. Chapter 5 presents theoretical study and experimental results on chemical vapor sensing with the 2D PCS sensor platform.

- Chapter 2 - Design of 2D PCS Sensor for Bulk Liquid Sensing

  This chapter firstly discusses two computation methods RCWA and FDTD for designing the 2D PCS. Single-layer 2D PCS is then discussed, including the bright guided resonance and the quasi-BIC modes. Finally, BIC modes in double-layer 2D PCS are investigated for bulk sensing.
- Chapter 3 - Fabrication of 2D PCS Sensor

  This chapter describes the fabrication process for single-layer and double-layer PCS. The fabrication of PDMS microfluidic chamber is also discussed.
- Chapter 4 - Characterization of PCS Sensor for Bulk Liquid Sensing

  This chapter presents measurement results for bright guided modes and quasi-BIC modes in single-layer PCS and double-layer PCS.
- Chapter 5 - PCS Sensor for Chemical Vapor sensing

  This chapter firstly discusses the theoretical design of 2D single-layer PCS for chemical vapor sensing. Then the experimental result is presented to prove the capability of PCS for vapor sensing. Two integration schemes are discussed for vapor sensing. The first configuration is a simple integration of PCS on SOI substrate with a glass gas chamber. The other configuration is an integration of PCS with silicon separation column. The silicon column with polymer coating can be used for gas separation.
- Chapter 6 - Summary and Future Work

  This chapter summarizes the work in this thesis, and gives some possible future directions for further study.

Chapter 2

Design of 2D PCS Sensor for Bulk Liquid Sensing

2.1 Simulation methods

2.1.1 Rigorous Coupled Wave Analysis

Rigorous coupled-wave analysis (RCWA) is a semi-analytical method in computational electromagnetics. It can solve scattering from periodic dielectric structures. It is also called Fourier modal method (FMM) or the scattering matrix method (SMM) [57]. It is widely used in the research community to solve grating diffraction for a few decades [58-61].

Victor Liu developed Stanford Stratified Structure Solver (S4), a frequency domain code to solve the linear Maxwell's equations in layered periodic structures, using RCWA algorithm [57].

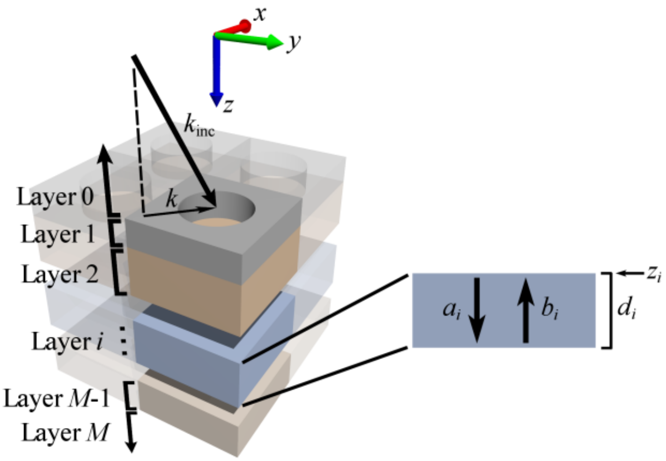

Figure 2-1: Left: 3D schematic of one unit cell for a stack of layers. Right: Cross-sectional view of layer *i*. [57]

As shown in Figure 2-1, the structure is periodic in the *xy* plane, and can be divided into a few layers in the z direction. Incident radiation from layer 0 is assumed to be a plane wave propagating in the positive *z* direction toward layer 1. ***K***inc denotes the incident wavevector with in-plane component ***k***. The field within a layer is expanded into eigenmodes which can be represented by Fourier basis. The transverse magnetic field in layer *i* can be written as:

$$\begin{bmatrix} h_x(z) \\ h_y(z) \end{bmatrix} = \sum_n \begin{bmatrix} \phi_{x,n} \\ \phi_{y,n} \end{bmatrix} (a_n e^{iq_n z} + b_n e^{iq_n(d_i - z)}) \tag{2.1}$$

where a_n is the coefficient of a forward propagating wave, and b_n is the coefficient of a backward propagating wave, *q* is a complex number. By matching boundary conditions at all interfaces, a_n and b_n can be determined from the linear system.

S4 can be used to compute transmission, reflection or absorption spectra of periodic, patterned and planar structures. The computation is very fast, and the spectrum obtained from S4 is smooth. It can obtain sharp spectral features for the Fano resonance in grating and 2D PCS. Therefore, it is very useful to do optimization with S4 to scan different geometry parameters for 2D PCS. All the reflection and transmission spectra in this thesis are computed with S4. However, because the tool works in the frequency domain, it does not have time-domain capabilities. It could not give accurate field plot compared with the FDTD method described in the following section.

2.1.2 Finite-difference time-domain method

Finite-difference time-domain (FDTD) is a numerical analysis method used for solving the MaxWell's equation [62-64]. It works by discretizing MaxWell's equation. The computation space is composed of *Yee cells*, which divides space and time into a regular grid and simulates the time evolution of Maxwell's equations. It is a time-domain method, which can solve for a wide frequency range with a single simulation run. Oskooi from MIT developed Meep, a popular free open-source implementation of the FDTD method for simulating electromagnetism [65].

The Maxwell's equations can be written as [65]:

$$\frac{\partial B}{\partial t} = -\nabla \times E - J_B \tag{2.2}$$

$$\frac{\partial D}{\partial t} = \nabla \times H - J \tag{2.3}$$

where E and H are electric and magnetic fields, D and B are electric displacement and magnetic induction fields, J is the electric-charge current density, J_B is a fictitious magnetic-charge current density. In a linear dispersionless medium, the constituent relations are $D = \varepsilon E$ and $B = \mu H$, where ε and μ are the relative permittivity and permeability.

In Meep, the standard *Yee grid* discretization is used to stagger the electric and magnetic fields in time and space, with each field component sampled at different spatial locations offset by half a pixel, allowing the time and space derivatives to be formulated as center-difference approximations. Meep further divides the grid into chunks that are joined together into an arbitrary topology via boundary conditions. Perfectly matched layers (PML) is defined in Meep to serve as a fictitious absorbing material for absorbing boundary condition.

FDTD method produces time-domain animations of field to visualize field evolution. It can be used to compute field distribution in a 2D PCS. All the field calculation in the thesis is performed with Meep. Because the defect free 2D PCS is periodic in *xy* plane, we simulate a unit cell of the 2D PCS structures with periodic boundary conditions (PBCs) applied to *xz* and *yz* planes and PMLs at the top and bottom of the unit cell to absorb outgoing fields. The excitation consists of a broadband planar Gaussian source located above the PCS to solve modes of the PCS. Field distribution for each mode is computed by exciting the PCS with a narrowband planar Gaussian source also located above the PCS. In Meep, resonance frequency and radiative quality factor of each localized mode is calculated with Harminv, a program that decomposes the fields into a sum of sinusoids and determines their frequencies and decay constants.

FDTD method typically requires long computation time and large memory, without approximation to simplify computation. Especially when the structure has high Q factor, smaller resolution is required, therefore the required time to simulate the reflection or transmission spectra accurately can increase dramatically. RCWA has its advantage in terms of speed and spectrum accuracy, and it can be used to resolve very high Q resonances. For periodic structure, RCWA would be sufficient for reflection and transmission spectrum simulation. For non-periodic structure, such as finite size grating and PCS or defect PCS cavity, FDTD would be a good option to provide accurate simulation. There are some commercial softwares for FDTD simulation in the market, such as Lumerical FDTD solution and Rsoft FullWAVE.

2.2 Single-layer PCS design

2.2.1 Bright guided resonance of PCS on SOI substrate

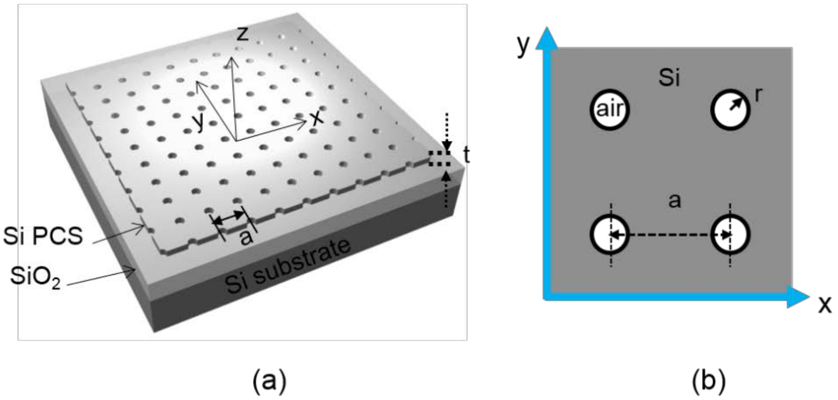

(a) (b)

Figure 2-2: (a) 3D schematic of PCS on SOI substrate. (b) 2D sketch of the Si PCS, where a is the lattice constant, *r* is the hole radius, and *t* is the Si PCS thickness.

We first consider a single-layer PCS shown in Figure 2-2. The silicon PCS is designed on silicon on insulator (SOI) substrate. We utilized S4 software to optimize the PCS to achieve high Q factor and high sensitivity. We take lattice constant *a* as 1000 nm and radius *r* as 100 nm for the optimization. The PCS is immersed in water with RI = 1.33. The reflection spectra for the PCS with various thicknesses from 120 nm to 200 nm are simulated and plotted in Figure 2-3(a). Increasing the thickness of the slab will shift the spectral resonance to longer wavelength. The sensitivities for each resonance were calculated based on the equation $S = \Delta\lambda/\Delta n$, by tracking the spectral shift when varying the refractive index of the medium above the PCS from 1.33 to 1.335. Mode *A* is observed to have higher sensitivity than the other modes, as shown in Figure 2-3(b). It has a sensitivity of around 300 nm/RIU.

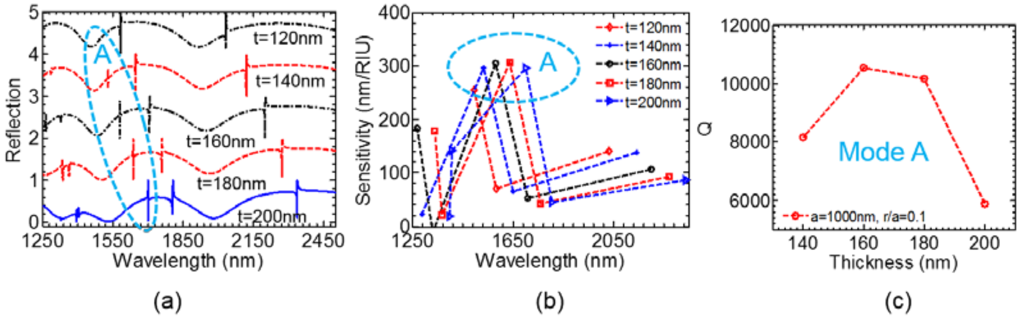

Figure 2-3: (a) Simulated reflection spectra of single-layer PCS on SOI substrate for different Si slab thickness, with *a* = 1000 nm and *r* = 100 nm at surface-normal incidence ($\theta = 0$). (b) Sensitivities for the resonant modes in (a). (c) Quality factor (*Q*) of mode *A* as a function of thickness of the Si slab.

The quality factor for Fano resonance mode *A* is fitted from Fano fitting based on the equation [66]:

$$R = {(F\gamma + \omega - \omega_0)^2} \Big/ {(\omega - \omega_0)^2 + (\gamma)^2} \tag{2.4}$$

where γ is resonance linewidth, ω_0 is the resonance frequency, and F is Fano parameter, which describes the degree of asymmetry. Q_{rad} is calculated from $\omega_0/2\gamma$. The Q factor is plotted in Figure 2-3(c) for different thickness of the slab. The maximum Q factor of ~10,000 is found at t = 160 nm.

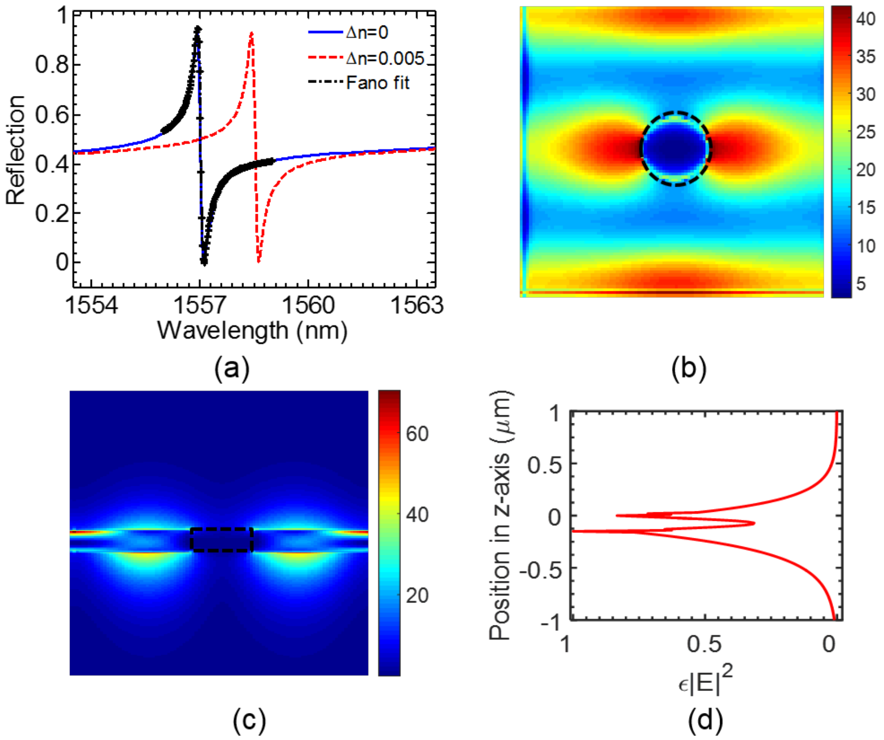

Figure 2-4: (a) Simulated reflection spectra of single-layer PCS in water (Δn = 0), and with small refractive index Δn = 0.005, PCS parameters: a = 1000 nm and r = 100 nm, t = 160 nm. (b) The $\varepsilon|E|^2$ profile in xy plane at the center of the PCS with boundary of the hole labeled in dashed circle. (c) The $\varepsilon|E|^2$ profile in yz plane at the center of the hole, with boundary of the Si PCS labeled in dashed rectangles. (c) Distribution of integrated $\varepsilon|E|^2$ in one unit cell along vertical (z-axis) direction.

Figure 2-4(a) shows the reflection spectra for the optimized PCS structure with 160 nm slab thickness. The reflection spectrum in water ($\Delta n = 0$) is fitted to the Fano equation 2.4. We examine the field energy distribution $\varepsilon|E|^2$ for mode A. Figure 2-4(b) shows the $\varepsilon|E|^2$ distribution in the x-y plane at the center of the PCS ($z = -80$ nm), with most of the energy confined in the high index silicon region. The $\varepsilon|E|^2$ distribution in the y-z plane at the center of the hole is plotted in Figure 2-4(c). To evaluate how much field energy is concentrated in the liquid region, we plot the integrated $\varepsilon|E|^2$ in one unit cell along z axis, as shown in Figure 2-4(d). The optical overlap integral f can be calculated to be 22%. With $S = \lambda_0 * f/n_{liquid}$ we can calculate the sensitivity to be 260 nm/RIU, which matches with the sensitivity of 300 nm/RIU calculated from resonance spectral tracking $S = \Delta\lambda/\Delta n$ using S4.

2.2.2 Bright guided resonance of suspended PCS

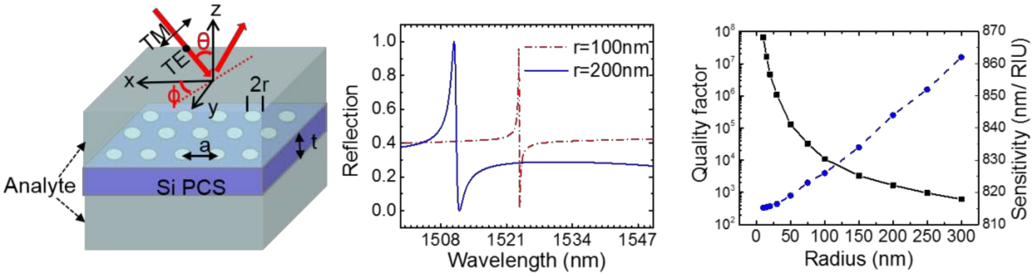

(a) (b) (c)

Figure 2-5: (a) 3D schematic of a suspended PCS in the analyte, where a is the lattice constant, r is the hole radius, t is the Si PCS thickness, θ is the incident angle, φ is the azimuth angle. (b) Simulated reflection spectra of a suspended single-layer PCS in water with $r = 100$ nm and $r = 200$ nm, other parameters: $a = 1000$ nm, $t = 160$ nm. (c) Quality factor and sensitivity of the resonance as a function of radius of the holes.

Here we consider a suspended silicon PCS in the analyte solution. The schematic is shown in Figure 2-5(a). Two angles are defined to represent the propagation direction of the incident beam, the incident angle θ (angle between incident beam and the surface-normal z axis) and the azimuth angle φ (angle between the positive x-axis and the incident beam projection in the x-y plane). The Si PCS is immersed in symmetric aqueous analyte (RI = 1.33), which also fill the air holes. Refractive index of Si is taken as 3.48. A portion of the incident light gets reflected back and the other portion of light gets transmitted through the PCS, neglecting the absorption in the analyte and the PCS.

The single-layer Si PCS consists of square lattice with period a = 1000 nm, and the thickness of the Si PCS t = 160 nm. The reflection spectra for the single-layer PCS with hole radius of 100 nm and 200 nm under surface-normal incidence ($\theta = 0^0$) are plotted out in Figure 2-5(b). Azimuth angle φ has no effect on the refection spectrum of the PCS at surface-normal incidence due to 90-degree rotational symmetry [67]. The spectral feature for the resonances becomes sharper when r reduces from 200 nm to 100 nm. The Q of the resonances, extracted from the Fano-fitting, is 10,940 and 1,654 for r = 100 nm and r = 200 nm, respectively. The sensitivity was calculated with the equation $S = \Delta\lambda/\Delta n$ by tracking the resonance shift at two different refractive indices n = 1.33 and n = 1.34 for the aqueous analyte solution. As shown in Figure 2-5(c), the resonance Q factor increases with the decrease of the radius. On the other hand, the sensitivity S only decreases slightly from 860 nm/RIU to 815 nm/ RIU when the radius decreases from 300 nm to 10 nm.

The $\varepsilon|E|^2$ profiles in xy plane and yz plane are shown in Figure 2-6(a) and (b). The integrated $\varepsilon|E|^2$ in one unit cell along the z axis is plotted in Figure 2-6(c). The blue shaded area is the Si PCS region. As analyte exists above and below the PCS, the calculated optical integral f in analyte is 0.733. The sensitivity is estimated to be 839 nm/RIU from $S = \lambda_0 * f / n_{liquid}$, which agrees well with the sensitivity of 830 nm/RIU calculated from resonance spectral tracking using S4. The sensitivities of the suspended PCS are much higher than the single layer PCS on SOI substrate because the analyte is distributed at both sides of the PCS.

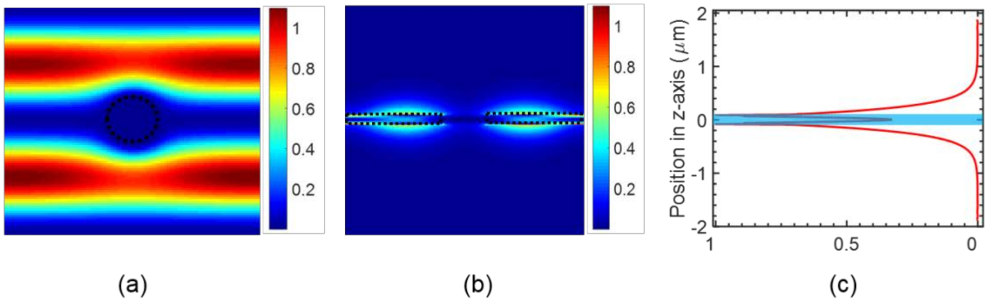

Figure 2-6: Simulated field distribution of the suspended single layer PCS with a = 1000 nm, r = 100 nm, and t = 160 nm, at the surface-normal incidence (θ = 0). (a) $\varepsilon|E|^2$ profile in xy plane at the center of the PCS with boundary of the hole labeled in dashed circle. (b) $\varepsilon|E|^2$ profile in yz plane at the center of the hole, with boundary of the Si PCS labeled in dashed rectangles. (c) Distribution of integrated $\varepsilon|E|^2$ in one unit cell along vertical (z-axis) direction, with blue shaded area indicating the Si PCS.

2.2.3 Quasi-BIC modes of suspended PCS

The discussion in the previous section considers an incident angle of zero. If the incident angle θ of the beam is not strictly zero, the symmetry is broken. At Γ point ($\boldsymbol{k}$ = 0, $\theta = 0^0$), square lattice possesses a symmetry group of C_{4v}. If it moves from Γ point to X point ($\theta \neq 0^0$, $\varphi = 0^0$), the symmetry group changes to C_{1h} [32]. As shown in the inset of Figure 2-7(a), the mode existing at $\theta = 0^0$ splits into two modes B and D. Two new modes A and C emerge in the spectra when θ is non-zero. They are symmetry-protected BIC at $\theta = 0^0$ because there is a symmetry mismatch between them and the radiation modes.

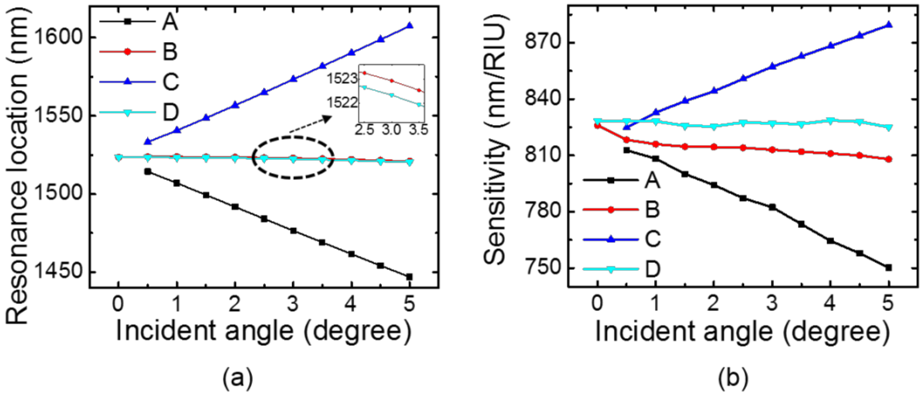

Figure 2-7: Simulation of suspended single-layer PCS with *a* = 1000 nm, *r* = 100 nm, and *t* = 160 nm at near surface normal incidence condition and $\phi = 0$. (a) Resonance spectral location dependence on incident angle. (b) Bulk sensitivity dependence on incident angle.

Modes *A*, *B* and *C* can be excited by source with TM polarization, while mode *D* can be excited by source with TE polarization. Sensitivity of the four modes are plotted in Figure 2-7(b). Mode *A* has lower sensitivity at larger angle, while mode *C* has higher sensitivity at larger angle. Sensitivity for mode *B* and *D* remains relatively unchanged in the incident angle ranges from 0 ~ 5 degrees.

Figure 2-8(a) shows the calculated quality factor with Fano fitting of the four modes at $\varphi = 0^0$ from the simulated reflection spectra. Modes *B* and *D* have a *Q* around 10^4 at $\theta \approx 0^0$, while the singly degenerate modes *A* and *C* have infinite *Q* when $\theta \approx 0^0$. Figure 2-8(b) shows a zoom-in view of the *Q* for the four modes at small incident angles. Mode *A* and *C* have $Q > 10^7$ in the incident angle range of 0 - 0.01 degrees. When the azimuth angle φ is not zero, mode *A* and *C* occur at slightly different wavelength in the reflection spectrum, but the quality factors for them are not affected much by the azimuth angle.

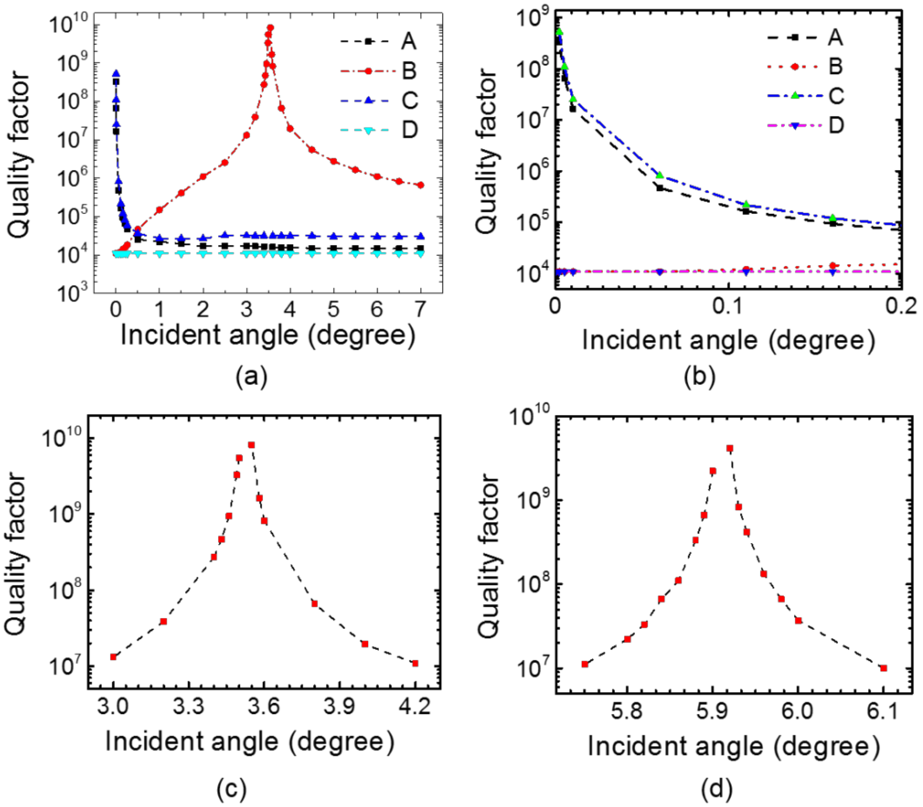

(a) (b) (c) (d)

Figure 2-8: Study of quality factor in suspended single-layer PCS at near surface normal incidence condition and $\phi = 0$. Design of the PCS: a = 1000 nm, t = 160 nm, r = 100 nm in (a)-(c), and r = 200 nm in (d). Q factor of the four modes in PCS at incident angle in the range of 0-7 degrees (a) and at near-zero incident angles (b). Mode B at incident angles near infinite Q condition for the PCS with two different radii: r = 100 nm in (c) and r = 200 nm in (d), respectively.

As we can see from Figure 2-8(c), mode B has extremely high Q at around 3.52 degrees, where it becomes a quasi-bound state. Unlike the symmetry-protected BIC for mode A and C at $\boldsymbol{k} \approx 0$, the high-Q resonance for mode B is due to the destructive interference between the leakage channels above and below the PCS. Mode B can achieve $Q > 10^7$ in the incident angle range of 3 - 4.2 degrees when $\varphi = 0^0$. When the radius r increases from 100 nm to 200 nm, the bound state for mode B occurs at an incident angle ~ 5.91 degrees, as shown in Figure 2-8(d). The results suggest that the BIC is robust. Small variations in device parameters (such as radius of the hole) only change the bound state to a different $\boldsymbol{k}$ value ***(***or incident angle in this case).

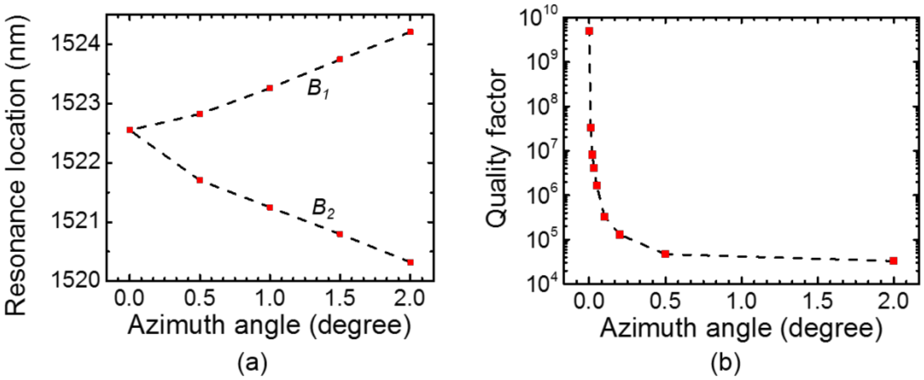

Figure 2-9: Simulation of mode B in suspended single-layer PCS with a = 1000 nm, r = 100 nm, and t = 160 nm at $\theta = 3.5^0$. (a) Resonance spectral location dependence on azimuth angle. (b) Quality factor dependence of mode B_1 on azimuth angle.

Unlike modes A and C, mode B splits to two modes B_1 and B_2 when the azimuth angle φ is not zero, as shown in Figure 2-9(a). The quality factor reduces for mode B_1 when azimuth angle increases, as indicated in Figure 2-9(b). Mode B_2 has lower Q than B_1 and it is not discussed here. For mode B_1 to achieve $Q > 10^7$, the azimuth angle φ needs to be in the range of 0 - 0.02 degrees.

2.2.4 Quasi-BIC modes of PCS on SOI substrate

Last section discuss the suspended PCS, which requires much effort in the fabrication process. Here we discuss the symmetry protected modes of the PCS on a commercially available SOI substrate. The SOI substrate we purchased from Soitec has a top silicon device layer of 250 nm. Therefore, we choose 250 nm top silicon thickness for the design in this section. The schematic is shown in Figure 2-10(a).

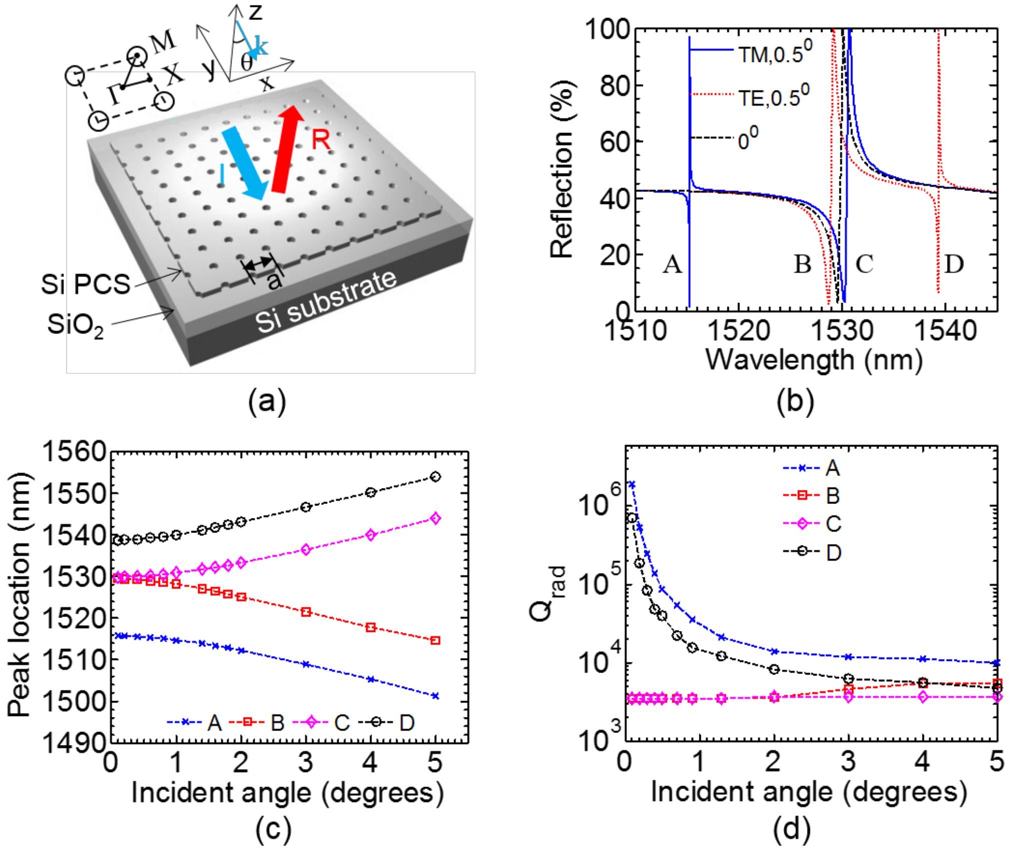

Figure 2-10: (a) 3D schematic of PCS on SOI substrate with light shinned at a incident angle *θ*. PCS parameters: *a* = 1000 nm, *t* = 250 nm, *r* = 100 nm. (b) Simulated reflection spectra for PCS at 0.5 degree and 0 degree incident angles. (c) Simulated band diagram of singly degenerate modes (*A, D*) and doubly degenerate modes (*B, C*) for the PCS. (d) Fano fitted quality factor for reflection spectra at different incident angles for the four modes.

At normal incidence ($\boldsymbol{k} = 0$, $\theta = 0^0$), there exists one doubly degenerate mode at 1530 nm, as shown in black dashed line in Figure 2-10(b). At 0.5^0 incident angle, a new mode *A* emerges at 1515 nm with TM polarized light source excitation, as shown in Figure 2-10(b). The new emerged non-degenerate mode *A* is uncoupled mode at Γ point ($\boldsymbol{k} = 0$), which has infinite life time and is completely decoupled from the external world, it is a symmetry protected BIC mode. When $\boldsymbol{k}$ is slightly greater than zero, this unique guided resonance has finite lifetime and could couple light in and out of the slab efficiently. At 0.5^0 incident angle, the singly degenerate mode *D* could be excited with TE polarized light source, which is also a symmetry-protected BIC mode. Figure 2-10(c) shows the dispersion curves of the four energy bands along the Γ-X direction under small incident angles (θ). The doubly degenerate mode at Γ point splits into two modes *B* and *C* when incident angle is not zero. The two singly degenerate modes *A* and *D* do not continue to $\boldsymbol{k} = 0$ in Figure 2-10(b) because they are uncoupled modes at $\boldsymbol{k} = 0$.

Figure 2-10(d) depicts the calculated radiative quality factor (Q_{rad}) of these four bands. Bands *B* and *C* originate from the doubly degenerate mode (at Γ point) and they have finite Q_{rad} at $\boldsymbol{k} \approx 0$, the singly degenerate bands *A* and *D* have Q_{rad} that approaches infinity when $\boldsymbol{k} \approx 0$. At Γ point, the doubly degenerate mode has the same symmetry as free-space modes, while the singly degenerate modes *A* and *D* are decoupled from free-space radiation modes due to symmetry mismatching.

Figure 2-11(a)-(d) shows the E_x component in *y-z* plane for the four modes excited at 0.5 degree incident angle. These modes have odd symmetry in their electric field with respect to the mirror plane perpendicular to the *z* axis. The field is greatly extended to the medium above the PCS, which is liquid in our case. At Γ point, square lattice has a symmetry group of C_{4v} with five irreducible representations. When moving away from Γ point to X point, the symmetry group changes to C_{1h} with only two irreducible representations.

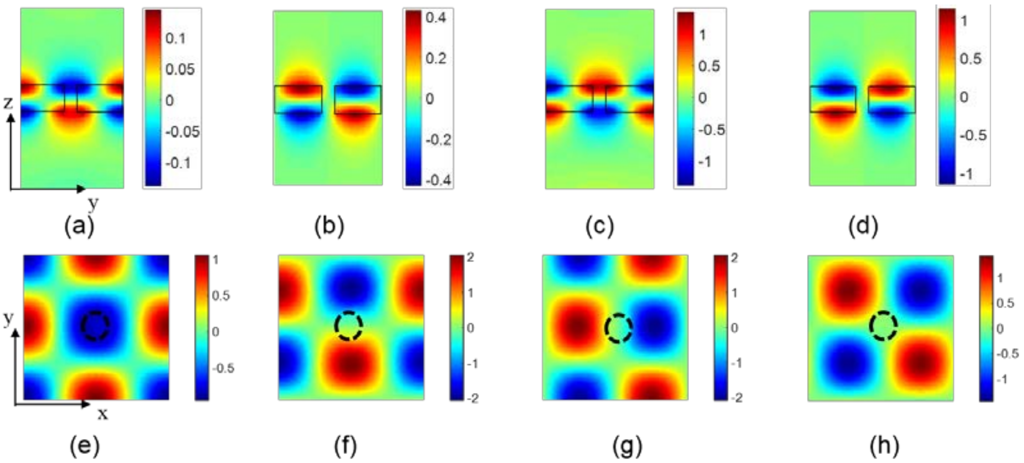

(a) (b) (c) (d)

(e) (f) (g) (h)

Figure 2-11: (a-d) *Ex* field distribution in *yz* plane at the center of the hole, (e-h) *Ez* field distribution in *xy* plane at the center of PCS slab for the four modes (a, e) *A*, (b, f) *B*, (c, g) *C*, (d, h) *D*, with air hole boundary shown in dashed line and the Si region boundary shown in solid line.

The symmetry of each mode could be determined by the mode profile of its E_z component in *x-y* plane. As shown in Figure 2-11(f) and (h), Mode *B* and *D* are antisymmetric around the *x* axis, it can be excited by TE polarized source. Figure 2-11(e) and (g) shows that mode *A* and *C* are symmetric around the *x* axis and hence excited by TM polarized source.

We examine the field energy distribution $\varepsilon|E|^2$ for *B* mode with 0.5 degree incident angle. Figure 2-12(a) shows the $\varepsilon|E|^2$ distribution in the *x-y* plane at the center of the PCS (z = -120 nm), with most of the energy confined in the high index silicon region. The $\varepsilon|E|^2$ distribution in the *y-z* plane at the center of the hole is plotted in Figure 2-12(b). To evaluate how much field energy is concentrated in the liquid region, we plot $\varepsilon|E|^2$

along *z* axis for the slice of $x = 0$, as shown with blue solid line in Figure 2-12(c). In Meep, we simulated one unit cell with space resolution of 10 nm, which is sufficient for our structure. We integrated $\varepsilon|E|^2$ along *z* axis for all the slices at every 10nm from x= -485 nm to $x = 485$ nm. The integrated $\varepsilon|E|^2$ is plotted with red solid line in Figure 2-12(c). The dashed lines indicate the boundary of PCS, with the PCS-liquid boundary located at $z = 0$ nm. The optical overlap integral *f* in the liquid region above the PCS is calculated to be 10.6% by integrating $\varepsilon|E|^2$ for $z > 0$, according to $S = \lambda_0 * f/n_{liquid}$. The *f* in the air hole of the PCS is around 0.3%, which does not contribute much to the bulk sensitivity. The other three modes *A*, *C* and *D* are also calculated in this way.

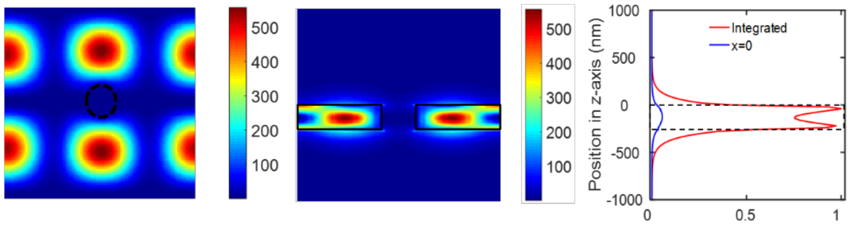

(a) (b) (c)

Figure 2-12: Simulation of B mode at 0.5 degree incident angle. (a) $\varepsilon|E|^2$ profile in *xy* plane at the center of PCS (z = -120nm) with air hole boundary shown in dashed line. (b) $\varepsilon|E|^2$ profile in *yz* plane at the center of air hole ($x = 0$), solid lines show the boundary of Si region. (b) Distribution of $\varepsilon|E|^2$ along vertical (*z*-axis) direction for $x = 0$ and integrated $\varepsilon|E|^2$ from -485 nm < x < 485 nm, with dashed lines showing the Si slab boundary.

A summary of the mode properties and sensor performance for the four modes at 0.5 degree incident angle is shown in Table 2-1. The integrated $\varepsilon|E|^2$ and sensitivity are almost the same for the four modes. For calculation of sensitivity in S^4, we simulated the reflection spectrum for $n_{analyte} = 1.319$ and $n_{analyte} = 1.329$. Symmetry protected BIC modes *A* and *D* have one order of magnitude higher *Q* with similar *S* compared with modes *B* and *C*, thereby achieving lower *DL.*

Table 2-1: Comparison of resonance location, radiative quality factor, sensitivity, and detection limit of the four modes simulated with S4 and MEEP.

Computation technique	Modes	*A*	*B*	*C*	*D*
S4	λ_0 (nm)	1515.3	1529	1530.4	1539.3
	Q_{rad}	86,500	3,500	3,500	39,385
	S (nm/ RIU)	100	105.5	105.4	100.7
	DL (RIU)	$4.1\text{x}10^{-6}$	$8.9\text{x}10^{-5}$	$8.9\text{x}10^{-5}$	$8.3\text{x}10^{-6}$
Meep	λ_0 (nm)	1518.1	1529.2	1530.2	1538.3
	Q_{rad}	73,772	4,230	4,093	59,582
	f	10.8%	10.9%	10.9%	10.8%
	S (nm/ RIU)	124	126	126	126
	DL (RIU)	$3.6\text{x}10^{-6}$	$6.2\text{x}10^{-5}$	$6.4\text{x}10^{-5}$	$4.4\text{x}10^{-6}$

2.3 Double-layer PCS design

2.3.1 Suspended double-layer PCS

The double-layer PCS configuration consists two Si PCS separated with an air gap distance t_g, as shown in Figure 2-13(a). The thickness of the top Si PCS is t_1 and the bottom Si PCS is t_2. The coupled PCS is immersed in analyte with the air hole and air gap filled with analyte. The coupled bi-layer PCS is immersed in aqueous solution with RI of 1.33. The 2D Si PCS has a square lattice with period a = 1000 nm and a hole radius r = 100 nm. The thickness of top Si PCS t_1 and bottom Si PCS t_2 are both 80 nm. The gap distance t_g affects the mode coupling between the top and bottom PCS [35]. We simulated the bi-layer PCS structure under surface-normal incidence condition with S4 software. The reflection spectra for the bi-layer PCS with gap distance t_g of 110 nm, 115 nm and 120 nm are plotted out in Figure 2-13(b).

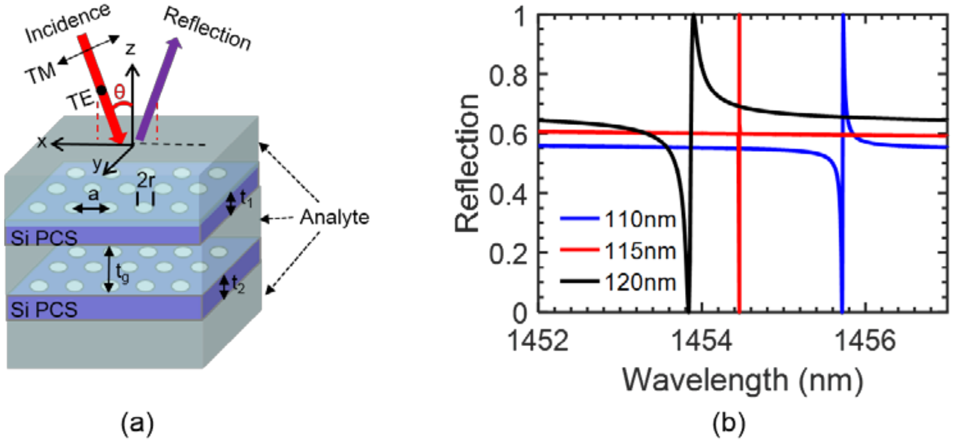

Figure 2-13: (a) Coupled bi-layer PCS where t_1 is the top Si PCS thickness, t_2 is the bottom Si PCS thickness, and t_g is the air gap distance between the top and the bottom Si PCS. (b) Simulated reflection spectra of the coupled bi-layer PCS, with a = 1000 nm, t_1 = t_2 = 80 nm, r = 100 nm and three different gap distance t_g at surface-normal incidence.

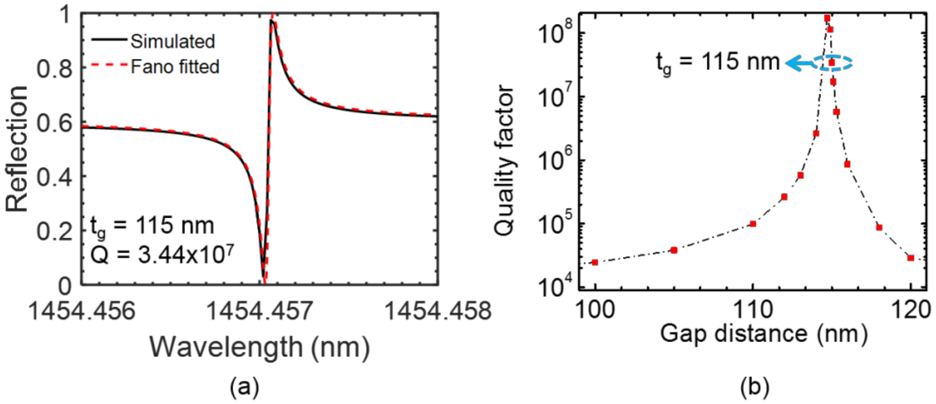

Figure 2-14: Simulation of bi-layer PCS with a = 1000 nm, t_1 = t_2 = 80 nm, r = 100 nm at surface-normal incidence (θ = 0). (a) Reflection spectrum of bi-layer PCS with t_g = 115 nm. Fano-fitting shows a Q factor of 3.44x10^7. (b) Quality factor for the resonance in bi-layer PCS with gap distance t_g varying from 100 nm to 120 nm.

Fano-fitting of the reflection spectrum for the coupled bi-layer PCS with $t_g = 115$ nm shows a quality factor of $3.44\text{x}10^7$, as shown in Figure 2-14(a). We further studied quality factor of the Fano resonance dependence on the bi-layer gap distance in Figure 2-14(b). The Fabry-Perot BIC forms at gap distance t_g around 114.7 nm. The top and bottom PCS act as a pair of perfect mirrors that trap waves between them. The bound state has an infinite *Q* and it cannot be observed in the spectrum. When the gap distance is slightly off, the bound state is perturbed, and it can couple to the external radiation mode with extremely high *Q*.

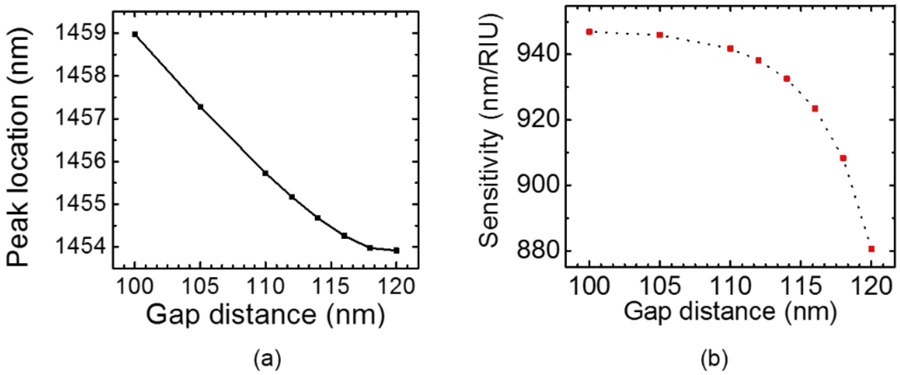

Figure 2-15: Resonance peak location (a) and sensitivity (b) for bi-layer PCS with gap distance t_g varying from 100 nm to 120 nm. Parameters of bi-layer PCS: $a = 1000$ nm, $t_1 = t_2 = 80$ nm, $r = 100$ nm at surface-normal incidence ($\theta = 0$).

The resonance peak location for the double-layer PCS shift to longer wavelength when the gap distance reduces, as shown in Figure 2-15(a). The bulk sensitivity decreases from 950 nm/RIU to 880 nm/RIU when the gap distance increases from 100 nm to 120 nm, as shown in Figure 2-15(b).

We computed the field distribution for the coupled bi-layer PCS with $t_g = 115$ nm using FDTD method. Figure 2-16(a) shows the electric field energy profile at the center of the top PCS (z = 100 nm) in the x-y plane. The field energy distribution at the center of the hole in the y-z plane is shown in Figure 2-16(b). The field is largely concentrated in the gap region between the top and bottom PCS, with large extension to the media above and below the slab. The integrated field energy in one unit cell is plotted in Figure 2-16(c). The optical overlap integral f in the gap analyte region is around 0.33, while f is around 0.26 in the analyte region above the top PCS or beneath the bottom PCS. The total optical overlap integral f in the analyte outside the Si PCS is around 0.85. The sensitivity could be estimated to be 930 nm/RIU based on $S = \lambda_0 * f/n_{liquid}$. The sensitivity calculated from spectral resonance tracking is around 925 nm/RIU, which agrees with the calculated sensitivity from optical field overlap integral f.

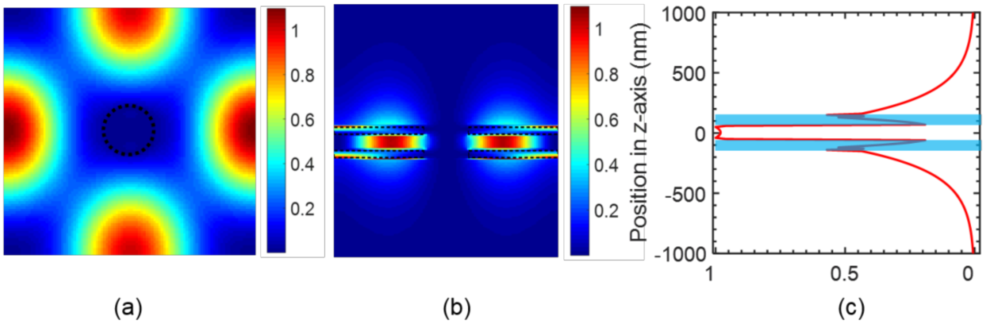

Figure 2-16: Simulation of field distribution of bi-layer PCS with a = 1000 nm, $t_1 = t_2$ = 80 nm, r = 100 nm, t_g = 115 nm at surface-normal incidence (θ = 0). (a) $\varepsilon|E|^2$ profile in xy plane at the center of top PCS with hole boundary shown in dashed circle. (b) $\varepsilon|E|^2$ profile in yz plane at the center of hole, dashed rectangles show the boundary of top and bottom Si PCS. (c) Distribution of integrated $\varepsilon|E|^2$ in one unit cell along vertical (z-axis) direction, with blue shaded area showing the top and bottom Si PCS.

If we tune the incident angle for coupled bi-layer PCS, the dependence of Q on incident angle for the four modes shows similar trend as that for the single-layer PCS. For one coupled bi-layer PCS design with $t_1 = t_2 = t_g$ = 80 nm, a = 1000 nm, and r = 100 nm, mode *A* and *C* have extremely high *Q* at $\theta \sim 0^0$, while mode *B* can achieve near infinite *Q* at an incident angle of ~ 3 degrees. The result suggests that the approaches to achieve high *Q* in single layer PCS by tuning incident angle also apply to coupled bi-layer PCS.

2.3.2 Double-layer PCS on SOI substrate

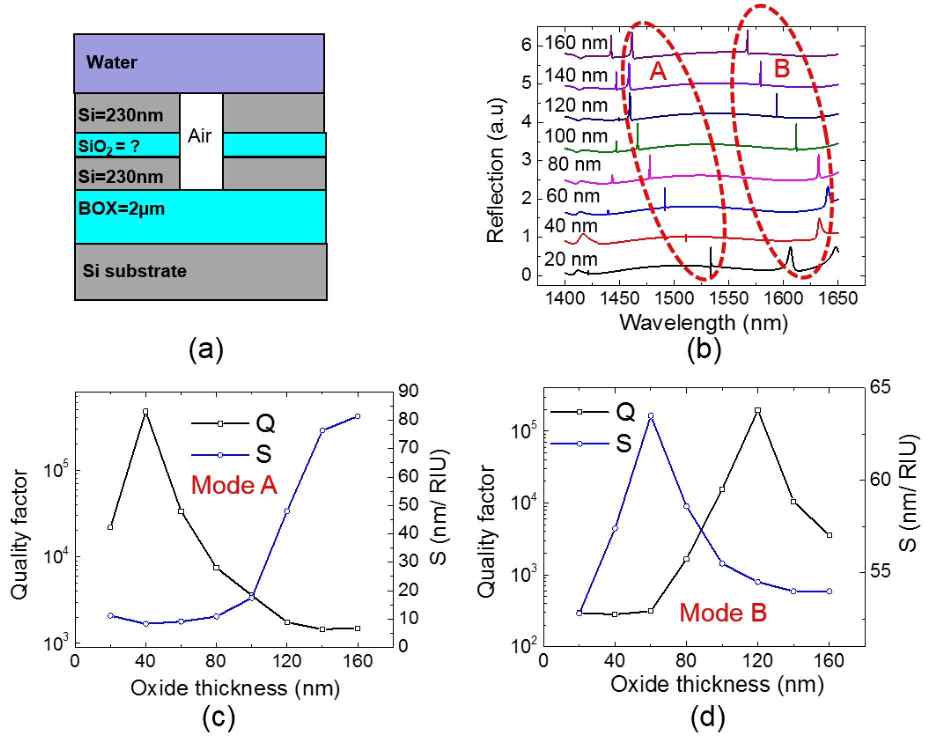

Figure 2-17: (a) The simulated structure on SOI substrate with a = 1000 nm, $t_1 = t_2$ = 230 nm, r = 150 nm, BOX = 2µm. (b) Simulated reflection spectra with different buffer oxide thickness at surface-normal incidence. (c,d) Quality factor and sensitivity (*S*) as a function of buffer oxide thickness for (c) mode *A*; and (d) mode *B*.

The suspended double-layer PCS structure discussed in last section gives good sensing performance, but it is difficult to fabricate. In this section we consider a much simpler case where the double-layer PCS is designed on SOI substrate, and the buffer layer between the two silicon slabs is oxide instead of air, as shown in Figure 2-17(a). The top and bottom PCS thickness are chosen to be 230 nm. The buffer oxide thickness is scanned from 20 nm to 160 nm to run the simulation for reflection spectra, as shown in Figure 2-17(b). Two modes exist in the wavelength range between 1450 nm to 1650 nm. Mode A has low sensitivity when buffer oxide thickness is less than 80 nm, but it shows low quality factor when buffer oxide thickness is greater than 80 nm, as shown in Figure 2-17(c). The maximum quality factor occurs when oxide buffer thickness is 40 nm. Mode *B* has a maximum quality factor with around 120 nm thick buffer oxide, while sensitivity does not change much when changing the buffer oxide thickness, as shown in Figure 2-17(d). Mode *B* is more suitable for sensing than mode *A*.

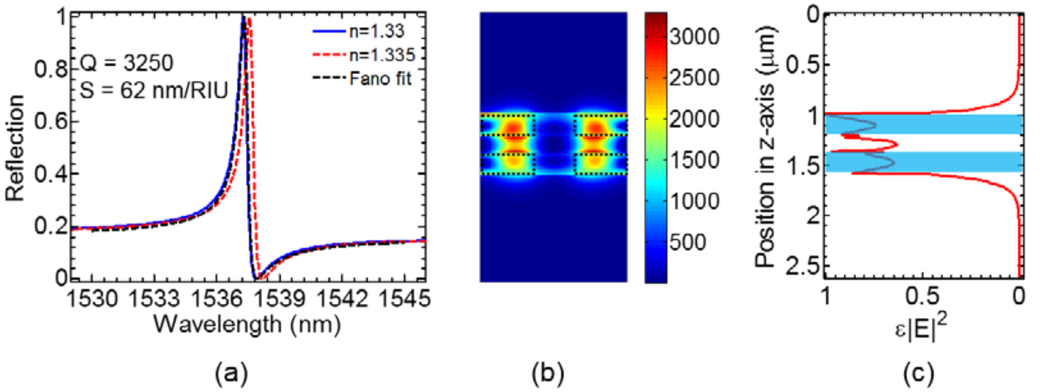

Figure 2-18: (a) Simulated reflection spectra for the double-layer PCS in water (*n* = 1.33) and with a small index change (*n* = 1.335). Q factor is 3,250 from Fano fitting. (b) $\varepsilon|E|^2$ profile in *yz* plane at the center of the hole, dashed rectangles show the boundary of top and bottom Si PCS. (c) The integrated $\varepsilon|E|^2$ along vertical (*z*-axis) direction in one unit cell, with blue shaded area showing the top and bottom Si PCS.

With 120 nm buffer oxide, mode *B* is at around 1590 nm, which is out of our tunable laser wavelength range (1470-1570 nm). Therefore, we choose 160 nm buffer oxide instead of the optimal 120 nm buffer oxide due to limitation of the wavelength range for our tunable laser. However, this restriction will not be an issue if we change the top and bottom slab thickness. The reflection spectra of mode *B* with 160 nm buffer oxide at two different liquid cladding refractive index $n = 1.33$ and $n = 1.335$ are shown in Figure 2-18(a). The quality factor is fitted to be 3,250 from Fano fitting. Sensitivity can be calculated to be 62 nm/RIU from the two spectral resonance. The field distribution in the *yz* plane at the center of the hole is shown in Figure 2-18(b), most of the light is confined in the silicon slab region. The integrated $\varepsilon|E|^2$ along vertical z direction is plotted in Figure 2-18(c). The field energy filling fraction *f* in the analyte sensing region (above the top silicon slab) is around 5% for this structure, which is the reason for low sensitivity.

2.4 Summary

Section 2.2.2, section 2.2.3 and section 2.3.1 discussed in this chapter can achieve high $Q > 10^7$ and high $S > 800$ nm/RIU simultaneously. The three cases discussed in section 2.2.1, section 2.2.4 and section 2.3.2 are all on SOI substrate, so the sensitivities are not as high as the suspended PCS. In this summary we only compare the three cases which are all suspended in the analyte solution.

Table 2-2: Summary of different approaches to achieve $Q > 10^7$, $S > 800$ nm/RIU and $DL < 10^{-8}$ RIU in PCS sensor design.

Configuration	**Section**	**Incident angle θ**	**Requirement**
Single-layer	2.2.2	0^0	Radius $r < 15$ nm
Single-layer	2.2.3	$\approx 0^0$	$0^0 < \theta < 0.01^0$
Single-layer	2.2.3	$> 0^0$	$3^0 < \theta < 4.2^0$; $\varphi < 0.02^0$
Bi-layer	2.3.1	0^0	Gap $t_g = 114.2 \sim 115.2$ nm

Spectral linewidth $\delta\lambda$ is related to resonance wavelength λ_0 and Q by $\delta\lambda = \lambda_0/Q$. Assume a spectral resolution R' as 1/20th of the spectral linewidth [2, 68], we can achieve $DL = R'/S \sim 10^{-8}$ RIU, with $Q = 10^7$ and $S = 800$ nm/RIU at $\lambda_0 \sim 1550$ nm. The requirement in each configuration studied in this work to achieve $Q = 10^7$ and $S = 800$ nm/RIU are summarized in Table 2-2.

For single layer PCS at surface-normal incidence (section 2.2.2), the radius of the hole needs to be less than 15 nm to have $DL < 10^{-8}$ RIU. For coupled bi-layer PCS to achieve $DL < 10^{-8}$ RIU at surface-normal incidence (section 2.3.1), the gap distance t_g is required to be in less than 0.5 nm away from 114.7 nm. Small hole size or high accuracy in gap distance and PCS thickness control are challenging in terms of fabrication of the device.

For single layer PCS with oblique incident light (section 2.2.3), the hole size can be relatively large. $DL < 10^{-8}$ RIU can be achieved for hole radius of 100 ~ 200 nm by controlling the incident angle and the azimuth angle. Non-symmetry protected BIC modes at large incident angle has much larger incident angle tolerance than symmetry protected BIC modes. It can maintain high $Q > 10^7$ in an incident angle range of 3 - 4.2 degrees with $\varphi = 0^0$. The larger incident angle range to maintain high Q is beneficial in relaxing the optical alignment requirement in practical sensor systems, as typically the incident Gaussian beam consists of a spread of ***k*** points (or incident angle) related to the lateral size of the beam [31]. However, the non-symmetry protected BIC modes has less tolerance in terms of azimuth angle compared to symmetry protected BIC modes. The quality factors of symmetry protected BIC mode A and C are not affected much when azimuth angle φ is not zero, while φ needs to be less than 0.02 degree for non-symmetry protected BIC mode B to achieve $Q > 10^7$. In experiment, the azimuth angle can be controlled by rotating the sample stage or adjusting the principle axis of the linear polarizer to control the polarization direction of the incident beam.

Chapter 3

Fabrication of 2D PCS Sensor

3.1 Single-layer PCS

3.1.1 Single-layer PCS with 250 nm slab

The most simple device design in chapter 2 would be the PCS on SOI discussed in section 2.2.4. The thickness of the silicon PCS is 250 nm, which is the same as the SOI wafers we purchased from Soitec. The fabrication process flow is shown in Figure 3-1. The PC device was fabricated on SOI substrate with electron beam lithography (EBL) and plasma dry-etching process.

Figure 3-1: Process flow for fabrication of PCS on SOI substrate with t = 250 nm.

Positive electron beam resist ZEP 520A is used for the patterning. The resist thickness is around 400 nm when spun at 2600 rpm for 60 s. EBL tool Jeol 6000 in the MRC at UT Austin was used for the exposure, with 50 kV volts and 108 μC/cm^2 area doses. 100 pA is used for the exposure. After exposure, the sample was developed in ZED-N50 (n-Amyl acetate) for 90 seconds, and followed by IPA rinse.

Table 3-1: RIE recipe for 250 nm silicon etching

Etch	**Pressure (mTorr)**	**Gas flow (sccm)**	**Power (W)**	**DC bias (V)**	**Time (s)**	**Etch rate (nm/min)**
1th	40	CHF_3=40; O_2=3	300	400	30	32
2nd	30	Cl_2 = 4; HBr = 5.4	170	250	360	55

The RIE etching of the top 250 nm silicon layer is done with Cl_2 and HBr gas combination, as shown in the second row of Table 3-1. This gas combination has very high etching selectivity of silicon to oxide. Therefore, before the silicon etching, it is necessary to do a first etch with fluorine based gas to remove the native oxide on silicon surface, as shown in the first row of Table 3-1.

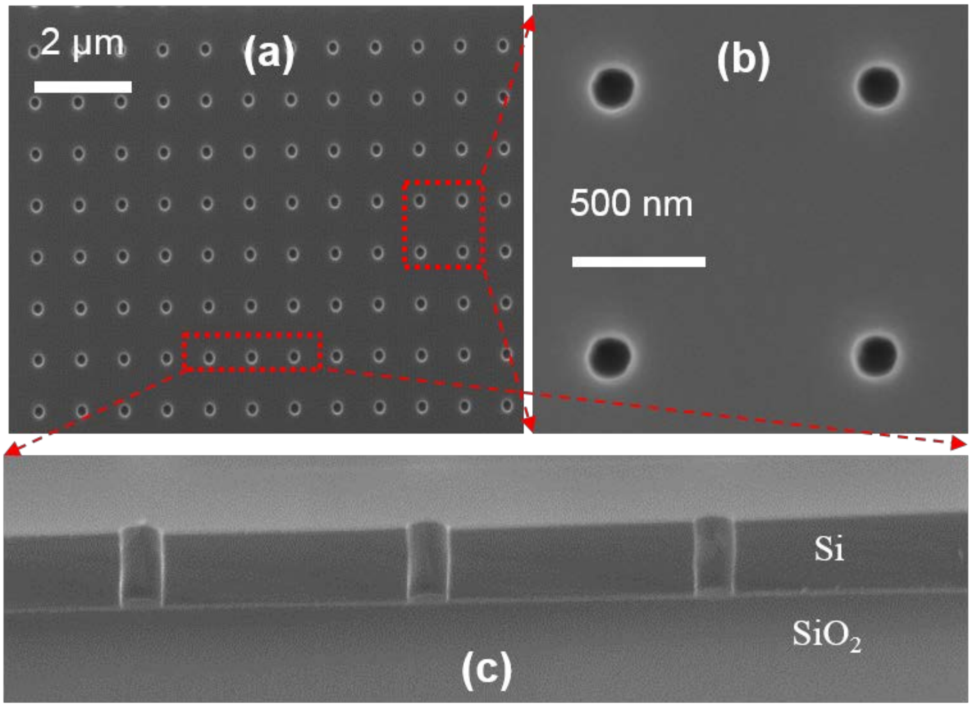

Figure 3-2: SEM images of one fabricated device on SOI substrate with *a* = 970 nm, *r* = 83 nm, *t* = 250 nm. (a) Top view of the PCS; (b) Zoom in of 2x2 air holes; (c) Cross-sectional view of three air holes.

The scanning electron microscope (SEM) images of one fabricated device are shown in Figure 3-2. The lattice constant, *a,* is 970 nm and the radius is 83 nm. The thickness of the silicon layer is 250 nm, measured with ellipsometer and confirmed with cross-sectional SEM image. As we can see from Figure 3-2(c), the sidewall of the etched hole is straight and the etching stops at the boundary between silicon and buried oxide layer due to slow etching rate of oxide with this gas combination.

The ellipsometer is J.A. Woollam M-2000 with wavelength coverage of the lamp from 193 nm to 1690 nm. Ellipsometry measures a change in polarization as light reflects or transmits from a material structure, a schematic of the ellipsometer is shown in Figure 3-3(a). The measured polarization change is represented as an amplitude ratio, Ψ, and the phase difference, Δ. The polarization change depends on the optical properties and thickness of individual materials. Therefore, ellipsometry is typically used to determine film thickness and optical constants such as the refractive index and the extinction coefficient [69].

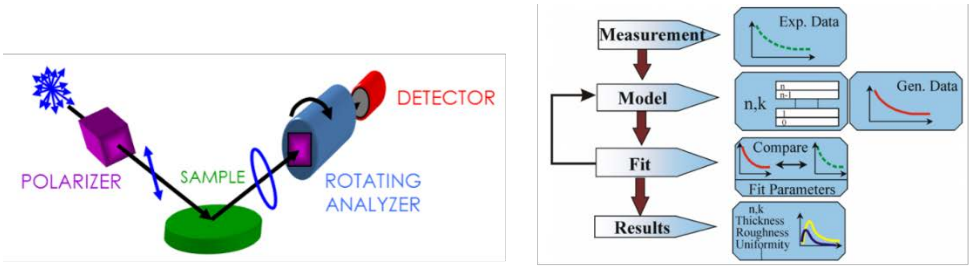

(a) (b)

Figure 3-3: (a) A schematic of the ellipsometer. (b) Flow chart of the data analysis for ellipsometry [69].

After the measurement is done, we build a model of the SOI structure with three layers: top silicon layer/buried oxide layer/silicon substrate. For transparent materials, the refractive index is often described using the Cauchy or Sellmeier relationship. The Cauchy relationship is typically given as:

$$n(\lambda) = A + \frac{B}{\lambda^2} + \frac{C}{\lambda^4} \tag{3.1}$$

where A, B, C are constant for the material and can be fitted with least-squares minimization. After fitting, we get a best guess for the thickness and also the refractive index of the material. The flow chart for data analysis is shown in Figure 3-3(b).

3.1.2 Single-layer PCS with 160 nm slab

For the design in section 2.2.1, the top silicon device layer is 160 nm, because our SOI wafer has a top silicon thickness of 250 nm, so we first need to do a thermal oxidation to reduce the thickness of top silicon layer from 250 nm to 160 nm. The process flow is shown in Figure 3-4.

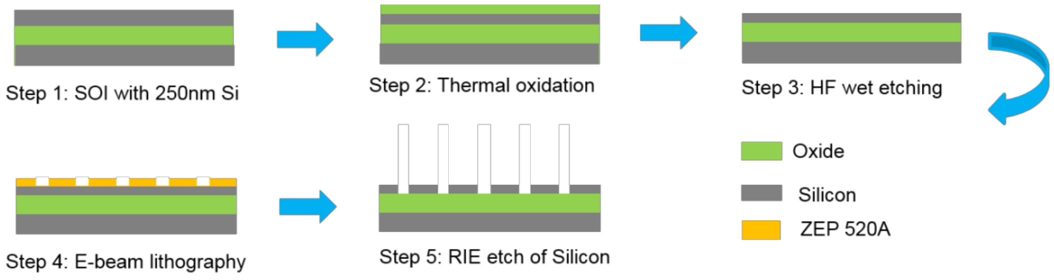

Figure 3-4: Process flow for fabrication of PCS on SOI substrate with t = 160 nm.

Wet oxidation is used to grow thermal oxide. Thermal oxidation is done in a furnace at 1050 ^{0}C using water vapor as the oxidant, the chemical reaction for the wet oxidation is:

$$Si + 2H_2O\ (vapor) \xrightarrow{1050\ ^0C} SiO_2 + 2H_2$$

The thickness of the thermal oxide over time follows Deal-Grove Model:[70]

$$X_{ox}{}^2 + AX_{ox} = B(t + \tau) \qquad (3.2)$$

where X_{ox} is the thickness of the thermal oxide, *t* is the time, τ is the time needed to produce the initial oxide layer at *t* = 0, *A* and *B* are parameters related to diffusivity, reaction rate constant, number of oxidant molecules and gas-phase mass transfer coefficient. To grow an oxide thickness of X_{ox}, a layer of silicon equal to a thickness of 0.44 X_{ox} is consumed. The thickness of the thermal oxide and remaining silicon are measured with ellipsometer. A few calibration runs are done to find the right time to thin down the silicon from 250 nm to 160 nm, which is around 25 minutes. Depending on the repeatability of different runs, dry oxidation with much slower growth rate can be further used to fine tune the thickness of the top silicon layer. In dry oxidation, the chemical reaction is like:

$$Si + O_2\ (gas) \xrightarrow{1000\ ^0C} SiO_2$$

The dry oxidation has a better control of the thickness, but with a much slower oxidation rate. 30 minutes only produce around 45 nm oxide with 20 nm silicon consumption. The quality of the oxide grown by dry oxidation is better than the wet oxide film with higher density, which results in a higher breakdown voltage. Therefore, thin oxides such as screen oxide, pad oxide, and especially gate oxide normally use the dry oxidation process. Wet oxidation is typically used to grow thick oxide such as masking oxide and field oxide.

After the thermal oxidation, the thermal oxide is etched with HF solution. The EBL patterning process is the same as last section. The RIE etching time in Table 3-1 need to reduce to 240 seconds. SEM images of one device are shown in Figure 3-5.

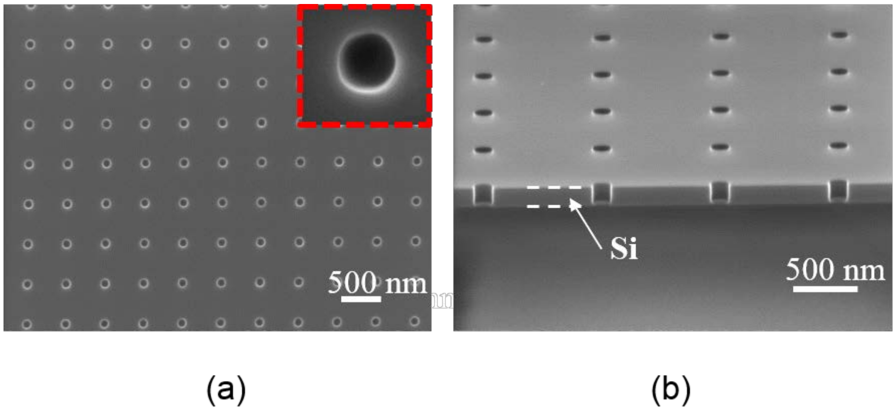

Figure 3-5: SEM image of one fabricated device on SOI substrate with *a* = 970 nm, *r* = 83 nm, *t* = 160 nm. (a) Top view of the PCS. The inset shows a zoom in of one air hole; (b) Cross-sectional view of three air holes.

3.2 Double-layer PCS

For the double-layer PCS design on SOI substrate in 2.3.2, the first step is to prepare the wafer with the desired thickness for each layer. One method to form the double silicon slabs is through oxide-oxide bonding of two thermally oxidized SOI wafers[71]. Here we adopted another way to form the double-silicon-slab structure. The process flow is shown in Figure 3-6.

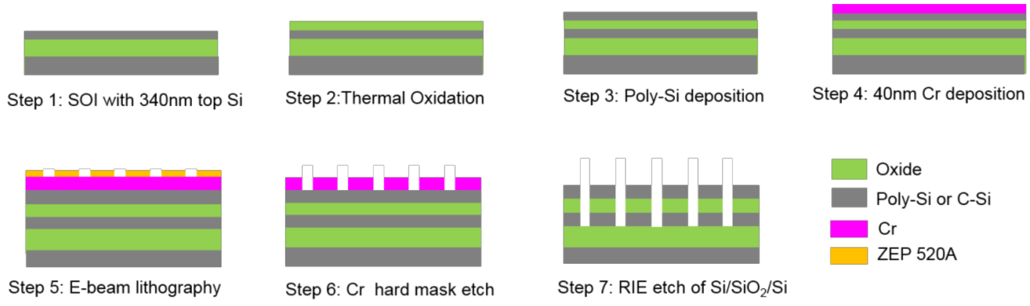

Figure 3-6: Process flow for fabrication of double-layer PCS on SOI substrate.

We start with a SOI wafer of 340 nm top silicon layer. After thermal oxidation to reduce the silicon layer to 230 nm, the thermal oxide is around 240 nm. As discussed in section 2.3.2, the buffer oxide thickness is designed to be around 160 nm. Buffered oxide etch (BOE) solution is used to precisely control buffer oxide thickness. A common BOE solution comprises a 6:1 volume ratio of 40% NH_4F in water to 49% HF in water. This solution will etch thermally grown oxide at approximately 2 nanometers per second at 25 degrees Celsius. If we dilute this BOE solution with DI water with 1:1 volume ratio, the etching rate of thermal oxide is around 1 nm/second. Ellipsometer was used to measure the thickness of oxide.

After forming the buffer oxide layer, amorphous silicon is deposited on the wafer by low pressure chemical vapor deposition (LPCVD), with 150 sccm SiH_4 gas flow at 550 degrees Celsius and at a low pressure of 300 mTorr. The deposition rate is around 3 nm/min, with slight variation depending on the location of wafer in the furnace. To have a uniform deposition, a few 4 inch dummy silicon wafers need to be placed in the quartz boat to have a more uniform gas distribution. The amorphous silicon will have large optical absorption. In order to reduce the optical absorption, it needs to be annealed to form poly-silicon. The wafers were annealed using a two-step annealing process [72]. The first anneal is a low temperature anneal that is done at 600°C N_2 for 30 hours, and the purpose of this anneal is for gradual grain nucleation, which results in large grains. The second anneal is a 6 hour 1000°C in N_2 to crystallize the individual polysilicon grains.

Now the wafer with the right thickness is ready. Because we will etch the entire triple-layer 230 nm Si/160 nm SiO_2/230 nm Si stack with RIE, a 400 nm ZEP 520A resist is not sufficient to stand the long time dry etching. 40 nm thick chromium is deposited on the triple-layer wafer with electron beam evaporation, to serve as a hard mask for the RIE etching. EBL is used to do the patterning on the wafer with chromium, and the chromium is then dry etched in a TRION Oracle production cluster chamber, with Cl_2 = 40 sccm, O_2= 10 sccm, RIE power = 80W at a low pressure of 30 mTorr. The etching rate for chromium is around 6 nm/min.

After transferring the pattern into chromium, the triple-layer 230 nm Si/160 nm SiO_2/230 nm Si stack was etched with RIE. The silicon is etched with Cl_2/HBr and the oxide is etched with CHF_3/O_2 gas. The RIE recipes can be found in Table 3-1, by tuning the etching time to over etch each layer. The buffer oxide etching step is the most critical step, because any remaining oxide will prevent the bottom silicon layer etching. Therefore, a quick BOE etch can be performed to ensure the over etch of buffer oxide layer. The SEM images of one sample #A with a quick BOE dip are shown in Figure 3-7(a) and (b). The BOE etch has laterally etched the buffer oxide a little. The sidewall of the bottom silicon PCS is slightly slanted due to the long dry etching with CHF_3/O_2 gas. The SEM images of another sample #B without BOE dip for buffer oxide etching are shown in Figure 3-7(c) and (d). The sidewall is straight without lateral etching. Some trench test patterns on sample #B were cut to visualize the sidewall more clearly in the cross-sectional view of SEM image.

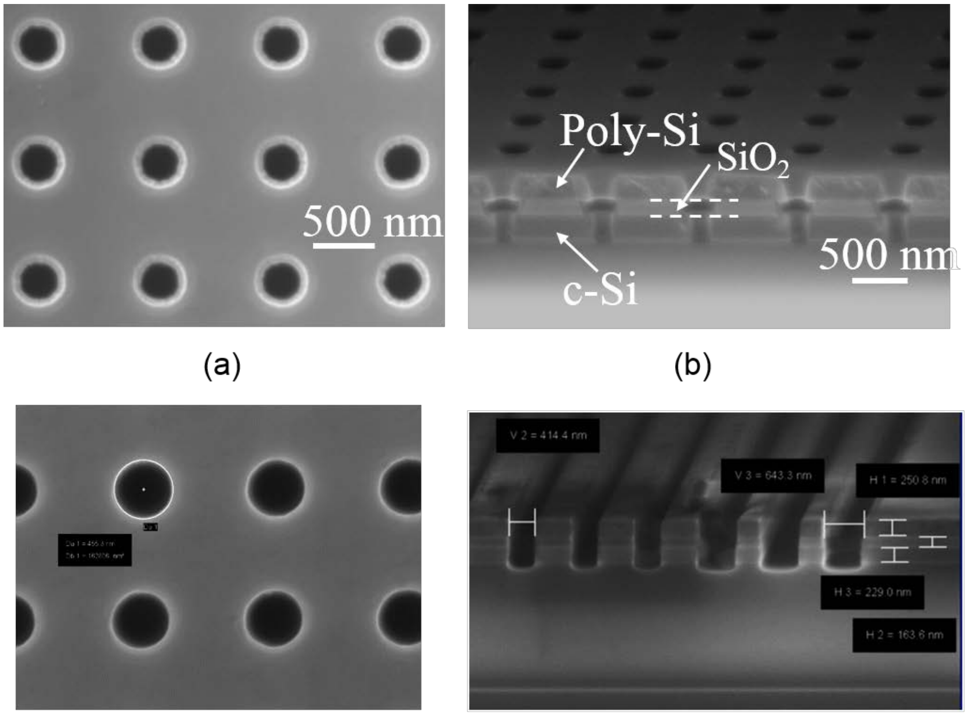

(a) (b)

(c) (d)

Figure 3-7: (a) Top view and (b) cross-sectional view SEM images of one fabricated bi-layer PCS sample #A with *a* = 1000 nm, *r* = 160 nm, Poly-Si = 230 nm, buffer oxide = 160 nm, c-Si = 222 nm. (c) Top view of bi-layer PCS sample #B with *a* = 1000 nm, *r* = 228 nm. (d) Cross-sectional view of one grating pattern on sample #B, it shows Poly-Si = 250.8 nm, buffer oxide = 163.6 nm, c-Si = 229 nm.

3.3 PDMS microfluidic chamber

The previous two sections discuss the fabrication of the single-layer and double-layer PCS. After the PCS is fabricated, we need to form a microfluidic chamber on top of the PCS for analyte solution delivery. Polydimethylsiloxane (PDMS) is one of the most widely used silicone-based organic polymers. Here we choose PDMS as the material for the fluidic chamber, because it has good chemical stability and it is optically transparent.

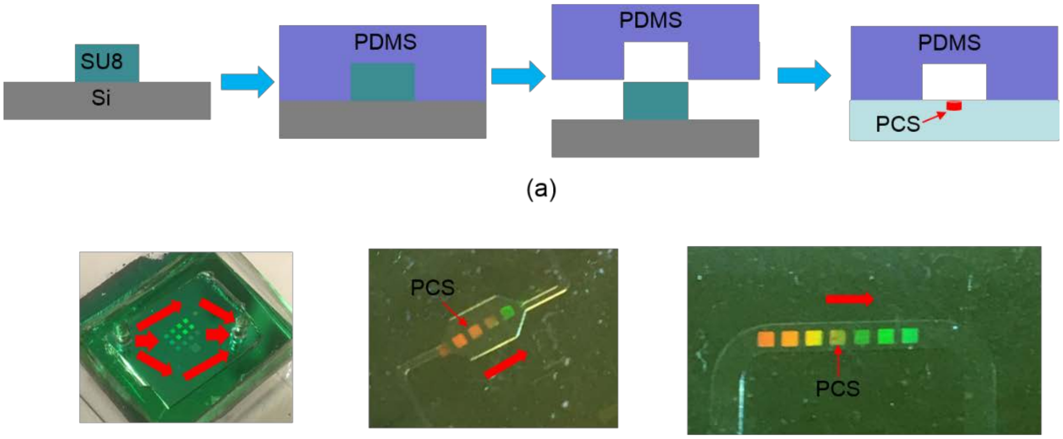

(b) (c) (d)

Figure 3-8: (a) Process flow to make a PDMS microfluidic chamber and bond on top of the PCS device (b) Device #1 with a big microfluidic chamber. (c) Device #2 with a smaller microfluidic chamber. (d) Device #3 with a small microfluidic chamber and minimized dead volume. Red arrows indicate the flow direction.

As shown in Figure 3-8(a), a 50 um thick SU8 strip is formed on the silicon wafer with photolithography. SU-8 50 resist is spun on silicon wafer at 2000 rpm for 60 seconds, followed by 6 minutes prebake at 65 degrees and 20 minutes softbake at 95 degrees. The thickness of SU8 is around 50 um, measured by profilometer. The exposure energy for SU-8 50 is 300 mJ/cm^2, followed by a post exposure bake of 5 minutes at 95 degrees, and then developed for 6 minutes. Hard bake of the pattern can prevent some cracks in the pattern.

A mixture of Sylgard 184 silicone elastomer base and Sylgard 184 silicone elastomer curing agent manufactured by Dow Corning (Midland, MI) were used to make the PDMS network [73, 74]. The base/agent mass ratio was chosen to be 10:1. After thoroughly mixing the corresponding elastomer base and the curing agent mixtures in a glass beaker, degassing the PDMS under vacuum is required to remove air bubbles in the mixture. After forming the SU8 strip on silicon wafer, the wafer is placed in a petri dish. The PDMS mixture is poured into the petri dish to have the SU8 strip immersed. The PDMS is cured in an oven at 65 C for 7 hours. After curing, the crosslinking reaction will produce a soft and flexible PDMS elastomer.

After cleaning the PCS sample with piranha solution, a mixture of sulfuric acid (H_2SO_4) and hydrogen peroxide (H_2O_2), both the PCS sample and PDMS elastomer were treated with O_2 plasma to enhance the adhesion [75]. The process flow to make a PDMS chamber and bond on the PCS device is shown in Figure 3-8(a). A few images of the PDMS microfluidic chamber with PCS device inside the chamber taken by a smartphone are shown in Figure 3-8(b-d). The configuration in Figure 3-8(b) has a big PDMS chamber volume, which also has some flow dead volume. The two configurations in Figure 3-8 (c) and (d) consume less analyte solution without flow dead volume. Multiple PCS devices are included in the PDMS microfluidic chamber for different designs.

Chapter 4

Characterization of PCS Sensor for Bulk Liquid Sensing

4.1 Bright guided resonance in single-layer PCS

After fabricating the single-layer PCS on SOI substrate and bonding with a PDMS microfluidic chamber, two holes are punched at the two ends of the PDMS channel and two tubing are inserted into the two holes. The other end of the outlet tubing is immersed in liquid analyte; the inlet tubing is connected to a syringe which is mounted on a syringe pump. The schematic of a single-layer PCS sample under test is shown in Figure 4-1(a).

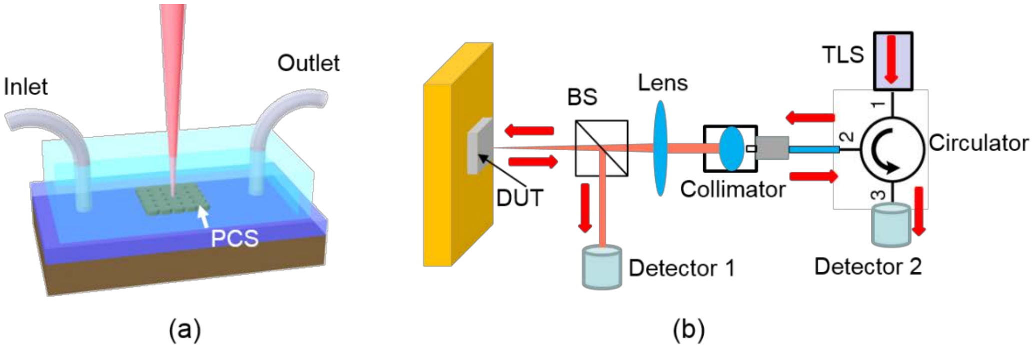

Figure 4-1: (a) Schematic of the PCS based optofluidic RI sensor. (b) Schematic illustration of the measurement system. TLS: tunable laser source, BS: beam splitter, DUT: device under test.

In this section, we discuss the characterization of bright guided resonance of single-layer PCS, the design was discussed in section 2.2.1. The PCS slab thickness is 156 nm, lattice constant, *a*, is 970 nm, radius is 103 nm. The test setup is shown in Figure 4-1(b). The syringe pump is in withdrawal mode with 0.1 mL/min flow rate of the analyte.

A tunable laser system in the 1465 nm to 1575 nm wavelength range with 1 pm tuning resolution and 9 dBm output power was used to test the reflection spectrum. The laser beam from tunable laser source (Agilent 81980A) passed through a fiber circulator (CIR1550PM-APC from Thorlabs), and got collimated by a fiber collimator (PAF-X-11-PC-C–FiberPort from Thorlabs) and focused onto the PCS at normal incidence by an 10x optical lens. The sample was mounted on a translation stage with six freedom adjustment, care was taken to maintain surface normal incidence by fine tuning the angle of the stage to have the reflection beam with maximum coupling into the fiber collimator and then being collected by detector 2. The reflected beam was detected by a germanium photo detector 1 (Agilent 81623B) through a beam splitter (BS015 - 50:50 Non-Polarizing Beamsplitter Cube from Thorlabs).

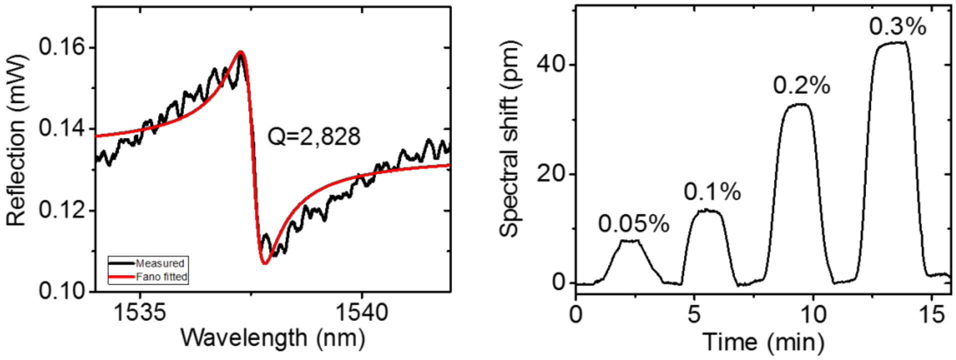

(a) (b)

Figure 4-2: (a) Measured reflection spectrum of PCS in water environment (black) and Fano fitting (red) shows a quality factor of 2,828. (b) Sensorgram of the spectral response to various concentrations of ethanol/DI water solution.

A measured reflection spectrum of the PCS in water environment is shown in Figure 4-2(a). The quality factor is found to be 2,828 from fitting to the equation 2.4. The simulated reflection spectrum for the device configuration (t = 156 nm, a = 970 nm, r = 103 nm) has a quality factor of 5,400. The reduction of quality factor in the test might come from the scattering loss and water absorption. The measured Q factor is related to the radiation quality factor from simulation and also the material loss (eg: scattering loss and material absorption) [76].

$$\frac{1}{Q_M} = \frac{1}{Q_{rad}} + \frac{1}{Q_{loss}} \tag{4.1}$$

The absorption induced quality factor Q_{abs} is given by [77]:

$$Q_{abs} = n_r / (2 f n_i) \tag{4.2}$$

where n_i and n_r are the imaginary part and real part for the absorptive material, f is the optical overlap integral in the absorptive material. We take n_i as 10^{-4} and n_r as 1.319 [78]. Optical overlap integral f is around 25% for this structure. Q_{abs} is calculated to be around $2.6\text{x}10^4$, which is the upper bound for the quality factor of this PCS sensor in water. Therefore, the measured quality factor is not limited by the quality factor in this case. The scattering loss from imperfect fabrication might cause the reduced quality factor.

We further characterized the sensing performance of the resonance at different RI for the analyte with various concentration of ethanol/deionized (DI) water mixture (0.05%-0.5% volume ratio). The spectral shift ($\Delta\lambda$) is read out from the linear region of the peak-to-dip transition in the Fano resonance. Specifically, linear fitting is performed in the peak-to-dip transition region of the Fano resonance mode. The intensity change (ΔI) is monitored in real-time at the point where $I = (I_{\text{peak}} + I_{\text{dip}})/2$ of the normalized reflection spectrum and then converted into $\Delta\lambda$, which is used as the sensing signal. The sensorgram tested for 0.05% to 0.3% ethanol volume ratio is shown in Figure 4-2(b). We performed water rinsing step before injecting new ethanol/DI water mixture to ensure that the PDMS chamber was free of residual ethanol from the previous test run. We can see that the Fano resonance spectral position redshifts when ethanol/DI water sample (i.e., RI increase) reaches the sensor surface and returns to signal baseline after DI water rinsing.

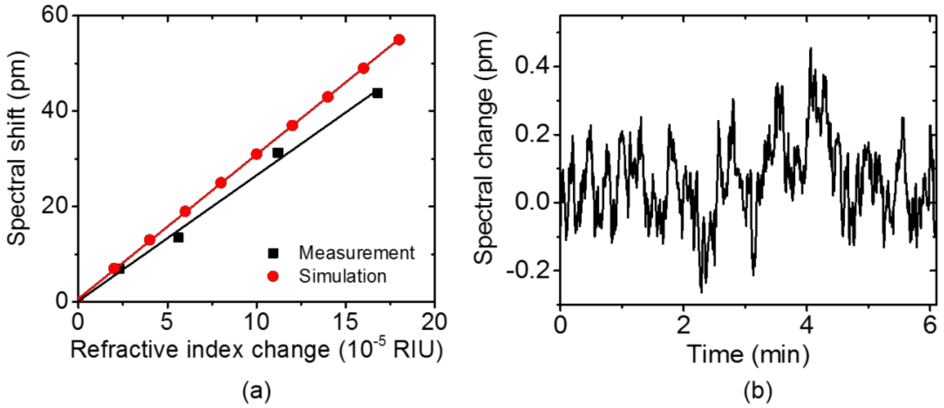

Figure 4-3: (a) Simulated and measured spectral shift as a function of refractive index change, the slope of the linear fitted line shows the bulk RI sensitivity. (b) Resonance spectral fluctuation of the PCS sensor over 6 minutes.

The respective spectral shift ($\Delta\lambda$) in Figure 4-2(b) with respect to RI change (Δn) is plotted in Figure 4-3(a). The RI change for various concentrations of ethanol/deionized (DI) water mixture is shown in Table 4-1.

Table 4-1: RI change for different concentration of ethanol/deionized (DI) water mixture

Volume ratio	0.1%	0.2%	0.3%	0.4%	0.6%	1%
RI change	$6x10^{-5}$	$1.1x10^{-4}$	$1.7x10^{-4}$	$2.2x10^{-4}$	$3.4x10^{-4}$	$5.6x10^{-4}$

The RI change versus volume ratio is quite linear up to 30%, it can be linear fitted with $\Delta n = 5.5x10^{-2}$ x (volume ratio) + $8x10^{-5}$, with a R^2 value of 0.9999. For volume ratio up to 10%, a more accurate fitting equation would be $\Delta n = 5.61\text{x}10^{-2}$ x (volume ratio) + $1\text{x}10^{-6}$.

To determine the *DL* of photonic crystal sensor, a representative baseline signal is acquired for 6 min, as shown in Figure 4-3(b). The standard deviation (σ) of the baseline signal is measured to be 0.117 pm. Extrapolating to the 3σ threshold, our photonic crystal sensor *DL* is determined to be $1.3\text{x}10^{-6}$ RIU based on $DL \sim 3\sigma/S$.

4.2 Quasi-BIC modes in single-layer PCS

To test the quasi-BIC modes discussed in section 2.2.4, we fabricated the 250 nm PCS on SOI substrate. The test setup is shown in Figure 4-4. Compared to the test setup in Figure 4-1(b), two linear polarizers were added in this setup. The crossed-polarized measurement technique suppresses the incident background light, revealing the guided resonance in the reflection spectrum with high extinction ratio (*ER*) [79, 80].

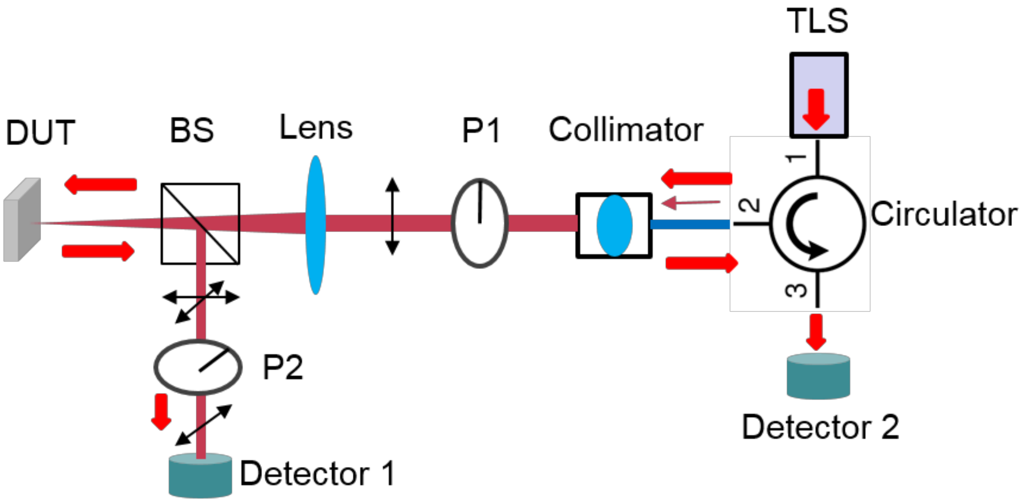

Figure 4-4: Schematic illustration of the measurement system. TLS: tunable laser source, BS: beam splitter, P1(P2): linear polarizer, DUT: device under test.

The tested reflection spectra of one PCS device with 250 nm slab thickness are shown in Figure 4-5(a). When the principle axes of the two polarizers are parallel, the line shape of the resonance is asymmetric, and we can see a small dip at 1527 nm. When rotating the second polarizer P2 to have larger angle with respect to the first polarizer P1, the intensity of the reflection will reduce. When polarizer P2 is at 90 degrees with polarizer P1, the intensity is very low because the majority of the background light is removed. However, if we zoom in at the reflection spectrum, we see two very profound resonances in Lorentzian line shape, as plotted in Figure 4-5(b). The extinction ratio is more than 10 dB. The mode at 1519 nm corresponds to the asymmetric major resonance in Figure 4-5(a), while the mode at 1527 nm is related to the small dip.

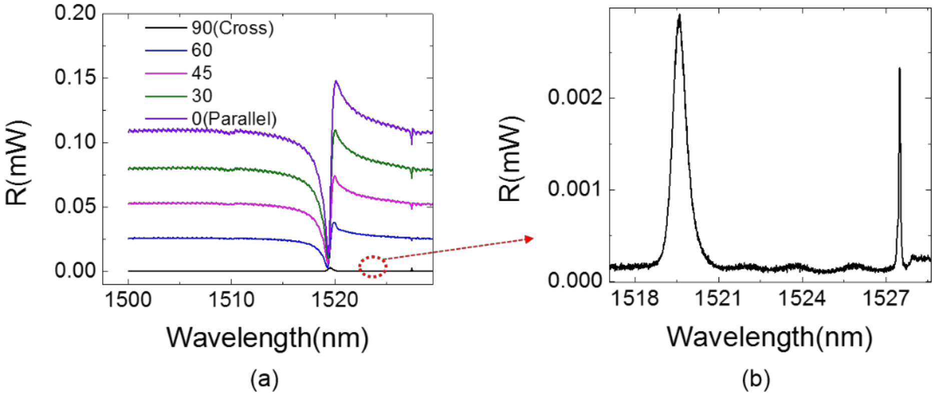

Figure 4-5: (a) The measured reflection spectra of one PCS with 250 nm slab thickness by changing the angles of the principle axis of two polarizers. (b) Zoom in for the cross polarizer tests when the principle axes of two polarizers are at 90 degrees.

Figure 4-6 shows experimental characterization of another PCS device with and without cross-polarization setup. First we measured the reflection spectrum of the fabricated PCS on SOI wafer at normal incidence without any polarizers (Figure 4-6(a)). The resonance has asymmetric line shape, which matches with Mode 4 in simulation results shown in Figure 4-6(c). After adding cross polarizers in the measurement setup, the experimental result of reflection spectrum is shown in Figure 4-6(b). All of the five modes can be clearly resolved in the reflection spectrum.

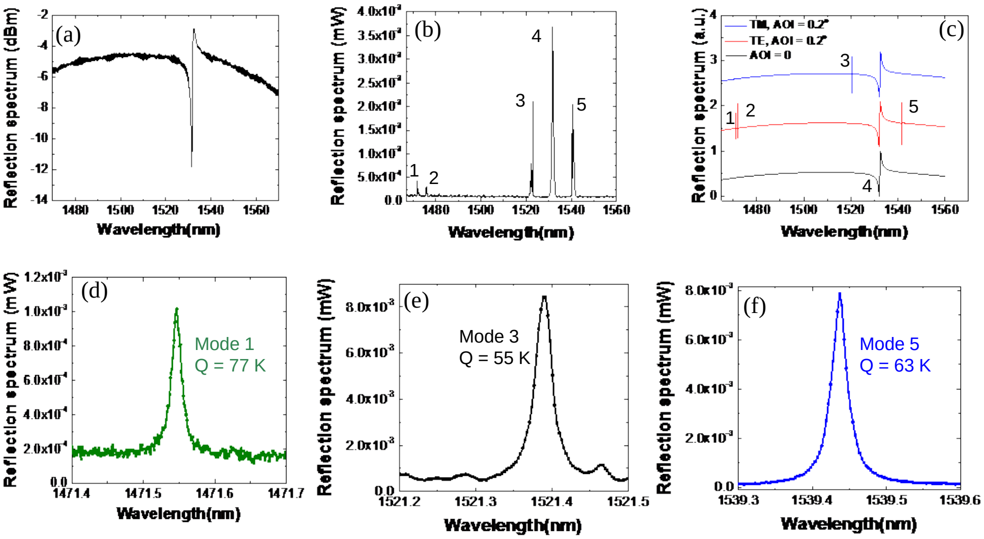

Figure 4-6: Experimental characterization of PCS with cross-polarization setup. (a) Reflection spectrum of single layer PCS without polarizers. (b) Reflection spectrum measured with cross- polarization setup. Five modes could be identified. (c) Simulation result of reflection spectrum for single layer PCS at normal incidence AOI = 0 and TE/TM mode at 0.2° incident angle. (d)-(f) Measured reflection spectra of Mode 1, 3, and 5 at optimized experimental condition.

As the incident laser beam is focused onto the PCS with a long working distance 10X objective lens, the incident beam has a small divergence angle although the sample is mounted at the beam waist of the incident Gaussian beam. The spectrum in Figure 4-6(b) should be superposition of angle of incidence (AOI) $\theta = 0$ and small incident angles $\theta < 1°$. Modes 1, 2, 3 and 5 are symmetry-protected BIC modes and can only be seen in the spectrum when $\theta \neq 0$ ($k \neq 0$). Simulation of the reflection spectrum at $\theta = 0$

and $\theta = 0.2°$ are shown in Figure 4-6(c). At normal incidence ($\theta = 0$), there is only one resonant mode and other BIC modes are invisible in the spectrum. For an incident wave that is either *s* or *p* polarized, the *s* polarization (TE) has the electric field perpendicular to the plane of incidence, while the *p* polarization (TM) has the magnetic field perpendicular to the plane of incidence. At small incident angle ($\theta = 0.2°$), TE polarized incident wave can excite mode 1, 2 , 4 and 5, while TM polarized incident wave can excite mode 3 and 4. Mode 4 also starts to split at $\theta = 0.2°$ but the spectral position change is small so we still take it as one mode. After optimization of incident beam relative to the PCS device, a high *Q* factor of 7.7x10^4, 5.5 x10^4, and 6.3 x10^4, is achieved for Mode 1, 3, and 5, respectively, as shown in Figure 4-6 (d, e, and f). These modes also have a very sharp spectral profile, showing high *ER*. The respective *ER* for Mode 1, 3, and 5 are 7 dB, 10 dB, and 20 dB, respectively.

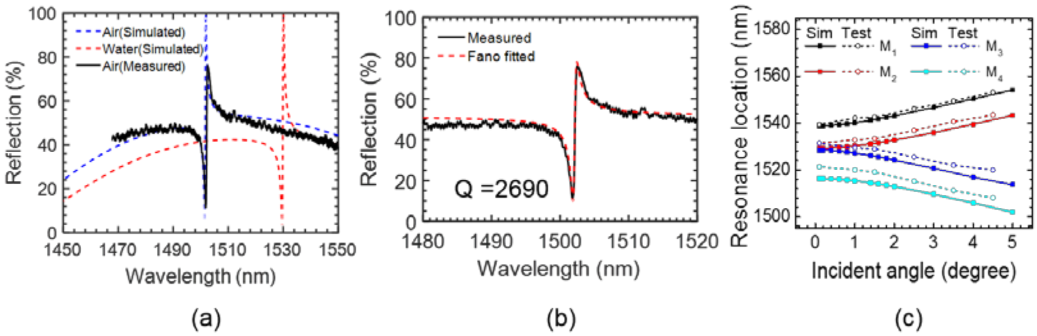

Figure 4-7: (a) Simulated reflection spectra of PCS at normal incidence in air and in water and measured reflection spectrum for PCS in air without polarizer. (b) Measured reflection spectrum in air and fano fitting shows *Q* = 2690. (c) Simulated and tested resonance locations for the four modes of the PCS on SOI substrate at different incident angles. Simulated data points are represented by squares and connected by solid lines, and tested data points are represented by circles and connected by dashed lines.

The simulation and test result of one 246 nm thick PCS device (*a* = 970 nm, *r* = 85 nm) in air and in water are shown in Figure 4-7(a). The black curve in Figure 4-7(a) shows the tested reflection spectrum of the PCS in air under normal incidence without crossed-polarized technique. Simulated reflection spectra of the PCS immersed in air is shown as blue dashed line, which matches well with the tested spectrum. When the PCS is immersed in water, the simulated reflection spectrum, shown as red dashed line, indicates around 30nm red shift compared to the spectrum in air. The fano resonance is asymmetric lineshape in the reflection spectrum [24]. The quality factor of the measured reflection spectrum can be fitted to be 2690, as shown in Figure 4-7(b). The measured and simulated resonance locations of the four modes (M_4, M_2&M_3, M_1 corresponds to Mode 3, 4, 5 in Figure 4-6(c)) at different incident angle from 0.1 to 5 degrees are plotted in Figure 4-7(c). The measured results agree well with the simulation results.

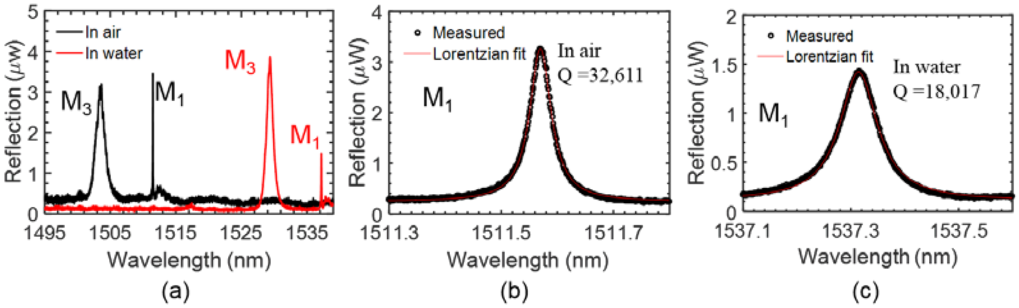

Figure 4-8: (a) Measured PCS reflection spectra with cross polarizers in air and in water. (b, c) Lorentzian fit of the measured reflection resonance for M_1 (b) in air and (c) in water.

The tested reflection spectra of the PCS in air and in water with crossed polarizer technique are shown in Figure 4-8(a). Measured quality factor Q_M for the spectrum in air and water is fitted by Lorentzian fitting [81]. Q_M is 3.2x10^4 for the resonance of the PCS tested in air and the Lorentzian fitting is shown in Figure 4-8(b). When testing the PCS immersed in water, the resonance spectral linewidth become broadened, exhibiting a Q_M

= 1.8×10^4, as shown in Figure 4-8(c). The extinction ratio is more than 10 dB for these resonances. Optical overlap integral f is 10.8% for this structure. Based on equation 4.2, Q_{abs} is calculated to be around 6.1×10^4, which is the upper bound for the quality factor of this PCS sensor in water.

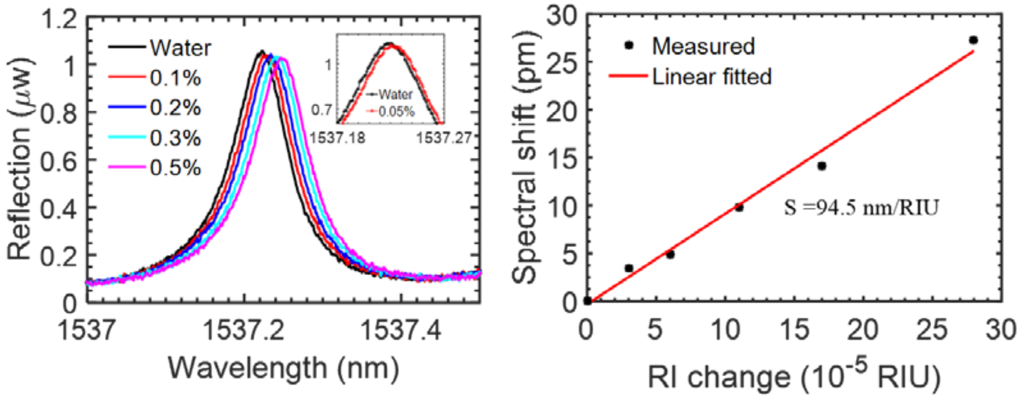

(a) (b)

Figure 4-9: (a) Measured reflection spectra of the PCS in water and in different concentration of ethanol/DI water mixture, with a zoom in of the spectrum in water and 0.05% ethanol concentration shown in the inset. (b) Bulk sensitivity of the PCS is linear fitted to be 94.5 nm/RIU.

We further characterized the sensing performance of Mode 1 at different RI for the analyte with various concentration of ethanol/deionized (DI) water mixture (0.05%-0.5% volume ratio). The spectrum tested for 0.05% to 0.5% ethanol volume ratio is shown in Figure 4-9(a). The spectral shift is plotted out in Figure 4-9(b) with lowest detectable RI change of 3×10^{-5} RIU. The bulk sensitivity for Mode 1 is fitted to be 94.5 nm/ RIU, which matches well with the simulated sensitivity of 100 nm/ RIU for this mode.

To test the sensorgrams in real time, a custom LabVIEW program was developed to track the peak of the resonance. The resonance location of the peak when injecting different volume ratio of ethanol and rinsing with DI water is shown in Figure 4-10(a). In Figure 4-10(b), the spectral shift of the resonance is plotted with respect to RI change of the analyte above the PCS surface. 0.1% ethanol/DI water mixture has a 6 x 10^{-5} RIU RI change compared to DI water and induced around 5 pm spectral shift, which can be clearly distinguished. The bulk sensitivity is 94 nm/RIU obtained from the linear fitting of the measured results.

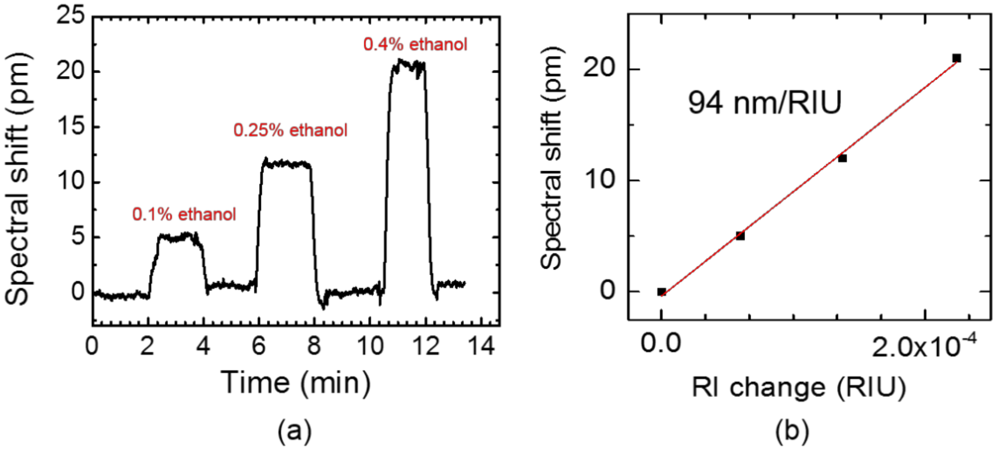

Figure 4-10: (a) Measured sensorgram of the spectral shift to various concentrations of ethanol/DI water solution. (b) Bulk sensitivity of the PCS is linear fitted to be 94 nm/RIU.

4.3 Double-layer PCS

For the double layer PCS design in section 2.3.2, we fabricated one device named “sample #A” as shown in Figure 3-7(a) and (b). In this section, we utilized the device to do some refractive index sensing experiments.

The device has parameters: *a* = 1000 nm, *r* = 160 nm, Poly-Si = 230 nm, buffer oxide = 160 nm, c-Si = 222 nm. The reflection spectrum was tested for the device in air and it matches with the simulation result, as shown in Figure 4-11(a). The *Q* factor for the simulated reflection spectrum is 6500 from Fano fitting, as shown in Figure 4-11(b). The tested quality factor is 2490, fitted from the measured spectrum, as we can see from Figure 4-11(c).

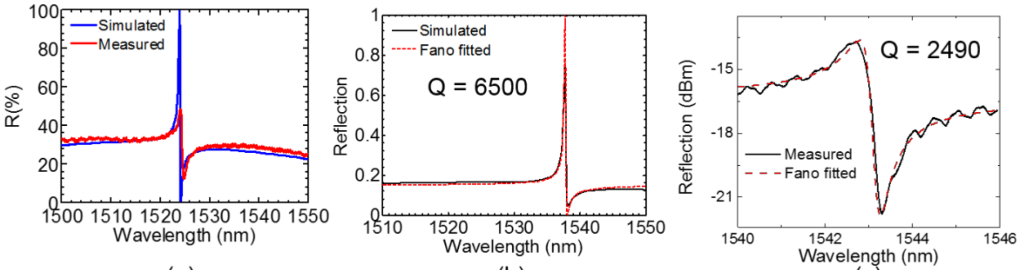

(a) (b) (c)

Figure 4-11: Measurement and simulation of bi-layer PCS with *a* = 1000 nm, *r* = 160 nm, Poly-Si = 230 nm, buffer oxide = 160 nm, c-Si = 222 nm: (a) Reflection spectra of a PCS in air. (b) Simulated reflection spectrum of the PCS when immersed in water, with a quality factor of 6500. (c) Measured spectrum in water shows a quality factor of 2490.

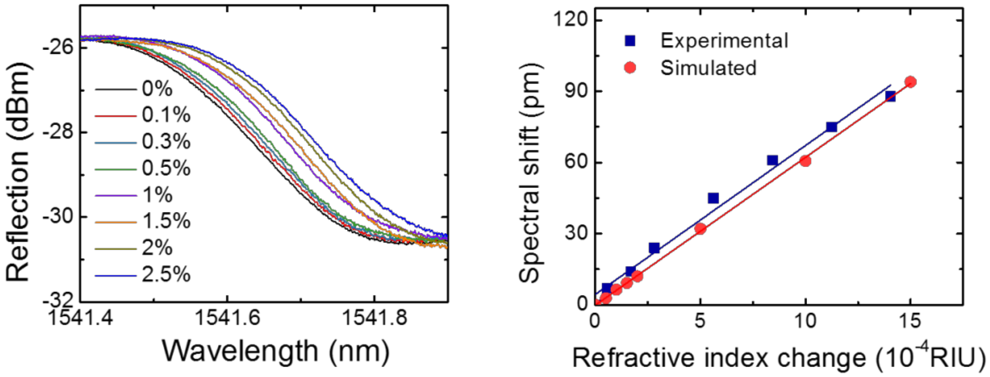

(a) (b)

Figure 4-12: (a) Measured reflection spectra of the bi-layer PCS in various concentrations of ethanol/DI water solution. (b) Simulated and measured spectral shift as a function of refractive index change, the slope of the linear fitted line shows the bulk RI sensitivity.

The spectra for different concentrations of ethanol solution were measured and shown in Figure 4-12(a). The ethanol volume ratio was changed from 0.1% to 2.5%. The resonance shows a consistent red shift with the increase of concentration. The unique asymmetric line shape and sharp peak-to-dip transition of the Fano resonance allows us to extract the spectral shift in the sharp transition region. The respective spectral shift ($\Delta\lambda$) with RI change (Δn) is plotted in Figure 4-12(b). A measured sensitivity of 62.8 nm/RIU was obtained by linear fitting from the experimental data. A simulated spectral sensitivity of 62.3 nm/RIU was acquired by linear fitting of the simulated data. Experimental and simulated results are in good agreement. The smallest Δn we measured from double-layer PCS is 5.6x10^{-5} RIU, which gives a Fano spectral shift of 4 pm.

4.4 Summary

In this chapter, refractive index sensing with bulk liquid was performed with two different configurations: single layer PCS on SOI and double layer PCS on SOI. For single layer PCS, both bright guided resonance and quasi-BIC modes (comes from symmetry-protected BIC modes) are discussed for sensing application. A summary is shown in Table 4-2. For single layer configuration, higher *S* is observed with bright guided resonance for 156 nm thick PCS design. Symmetry-protected BIC modes in 246 nm thick single layer PCS achieves higher *Q* but lower *S*. The sensitivity for the symmetry-protected modes can be increased by reducing the slab thickness, as more field will be extended to the analyte for reduced slab thickness. They obtain the same measured detection limit of 2.3x10^{-5} RIU since *DL* is determined from both *Q* and *S*. The double-layer PCS achieve 5.6x10^{-5} RIU *DL* with a non-optimal design.

Table 4-2: Summary of the experimental result of *Q*, *S* and *DL*

Configuration	**Principles**	**Q**	**S (nm/RIU)**	**DL (RIU)**
Single-layer; 156 nm PCS	Bright guided resonance	2,828	264	2.3x10^{-5}
Single-layer; 246 nm PCS	Symmetry-protected BIC modes	18,000	94.5	2.3x10^{-5}
Double-layer; 230/160/222 nm	Bright guided resonance	24,90	62.8	5.6x10^{-5}

Chapter 5

PCS Sensor for Chemical Vapor sensing

5.1 Introduction of vapor sensors

Optical vapor sensors have been widely used in industrial emission control, environmental monitoring, healthcare and homeland security [82]. The majority of optical vapor sensors measure either gas absorption or refractive index (RI) change induced by the gases. Absorption-based vapor sensing is highly specific because of the characteristic absorption lines resulting from the molecular rotation and vibration in the near IR (700 nm - 2.5 μm) and mid-IR range (2.5 μm - 14 μm) [82]. However, the sensor typically requires large dimension of the gas cell to have enough absorption based on Beer–Lambert law.

Researchers have investigated different types of optical structures for refractive index (RI)-based vapor sensors, including ring resonators [10, 11, 83, 84], SPR [85-87], Fabry-Perot interferometers [88-91], photonic crystal fiber (PCF) [92-96], and photonic crystals (PhC) cavity or waveguide [12, 97-102]. Most of the ring resonators, SPR sensors and Fabry-Perot interferometers have a layer of vapor-sensitive polymer coating on the sensor surface to capture the vapor molecules. The absorbed vapor molecules introduce change in refractive index and thickness of the polymer, causing a shift for the resonance wavelength of the whispering gallery modes (WGM) in ring resonators or change of the resonant angle in SPR sensors.

PCF has been investigated in vapor sensing due to its built-in gas fluidics, efficient light-vapor interaction, flexibility, and potential for remote sensing, in which the hollow cores of the fiber are filled with vapors [92-96]. PCF vapor sensors are typically based on absorption change in the transmission spectra. PCF sensors are flexible and allow for remote and distributed sensing. However, PCF vapor sensors typically need a length of a few tens of centimeters of PCF in order to have sufficient absorption, which suffers from long response time because it needs to fill the hollow region of the PCF with the gas analyte [92-94, 96]. The launching conditions is also critical, when injecting and extracting light to and from the PCF [93, 96]. The coupling of input light from fiber into the PCF requires good alignment, and a gap between the input fiber and the PCF is required for filling gas into the PCF.

Photonic crystal cavities and waveguide based vapor sensors can be very compact with enhanced light matter interactions. Slow light in a PCS slot waveguide can be utilized to enhance absorption of the vapor [12]. However, the spectral range with strong slow light effect is narrow, therefore it requires very careful design and fabrication to match the narrow low group velocity spectral region with the absorption peak of the analyte, and it can only be used for a few vapors [12, 103]. A few PCS defect cavity based vapor sensors tracked the resonance shift due to refractive index change of the vapor at the sensor surface[99, 100]. For both localized defect PCS cavities and slotted PCS waveguide, careful alignment is required to couple the beam from the fiber to the in-plane access waveguide.

Fano resonance in defect-free photonic crystal slabs (PCS) provides an effective channel for the light to radiate to the external environment [23, 24], and the evanescent field is quite sensitive to the RI change near the PCS surface. It has been demonstrated for bulk liquid sensing with a detection limit of 10^{-5}-10^{-6} refractive index units (RIU) [13, 16, 17]. However, there is not much work in vapor detection. Only several studies have discussed one dimensional (1-D) and two dimensional (2-D) defect-free PCS by doping dye in the polymer, where polymer swelling due to exposure to specific gases caused shift in the emission wavelength of the PCS cavities [101, 102].

5.2 Theoretical study of vapor sensing with PCS

The schematic of the PCS on SOI substrate is shown in Figure 5-1(a), with a 250 nm top Si device layer and 3 μm SiO_2 layer. The Si PCS is designed with lattice constant *a* = 980 nm and radius *r* = 85 nm. The incident beam shines on the PCS along surface-normal direction (*z*-axis) and gets reflected back.

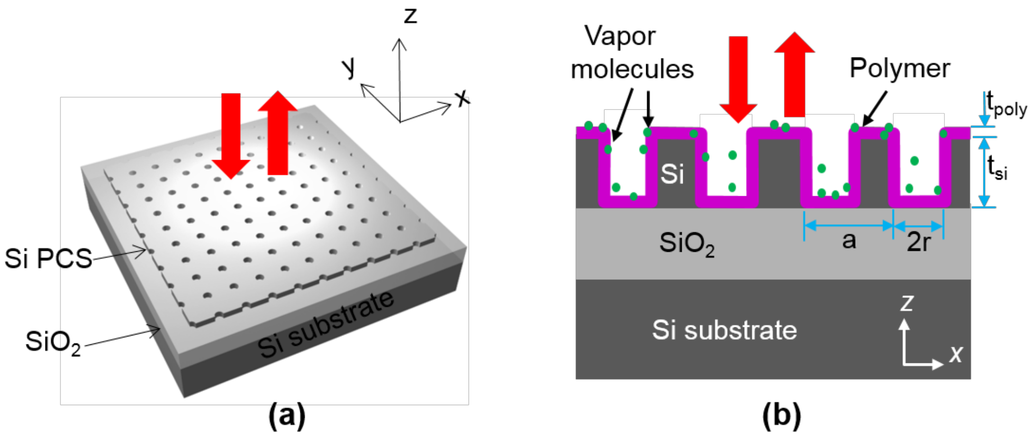

Figure 5-1: (a) A schematic view of a PCS vapor sensor with free-space coupled laser beam; and (b) A cross-sectional view in *x-z* plane of the PCS for vapor molecules sensing with coated polymer, where *a* is the lattice constant, *r* is the hole radius, t_{Si} and t_{poly} are the thicknesses of Si and polymer, respectively.

The sensor utilizes a thin layer of polymer coating on the PCS surface to serve as a transduction layer, capturing and concentrating the vapor molecules, as schematically shown in Figure 5-1(b). When vapor molecules are adsorbed, the interaction between vapor molecules and polymer causes a change in refractive index and thickness of the polymer, resulting in a shift of the resonance wavelength.

The refractive indices of Si, SiO_2 and OV-101 polymer are taken as 3.48, 1.45 and 1.4, respectively. The reflection spectra at surface-normal incidence for the PCS without polymer coating and with 100 nm polymer coating are shown in Figure 5-2(a). The resonant spectral location redshifts 27 nm as a result of 100 nm polymer coating. The spectral shift for the PCS with various thickness of polymer is plotted in Figure 5-2(b). The resonant peak shifts at a rate of 0.33 nm/nm for polymer thicknesses less than 60 nm, and approaches a saturation value of 38 nm when the polymer thickness is great than 250 nm.

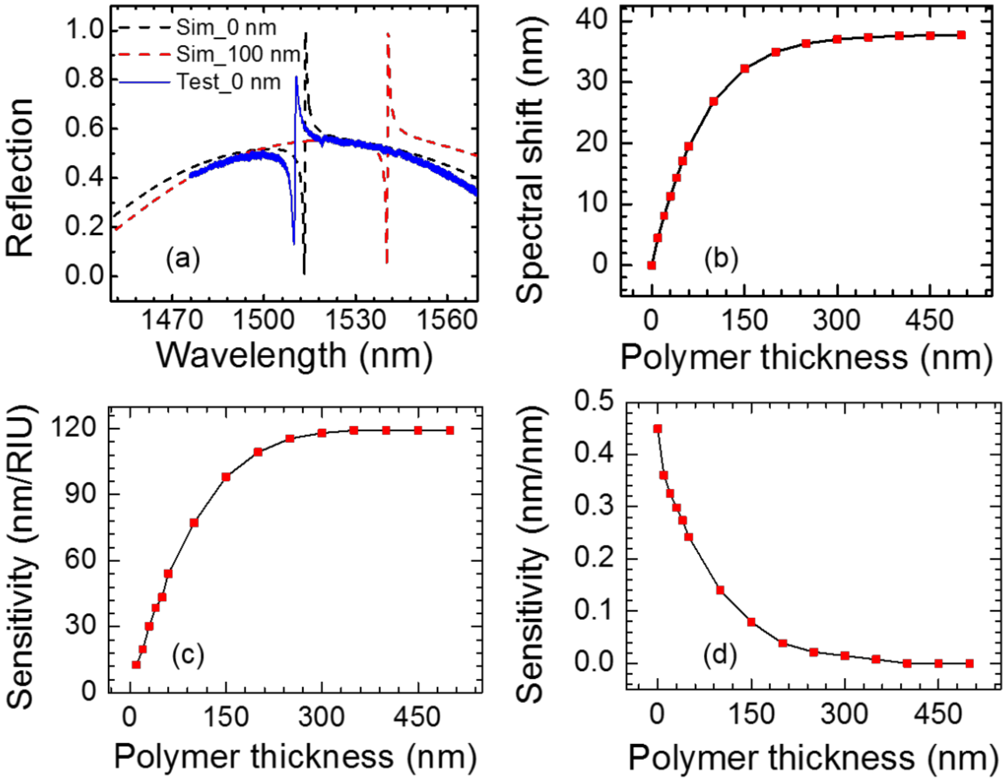

Figure 5-2: Spectral shift and sensitivity of the PCS as a function of polymer thickness. (a) The simulated reflection spectra for PCS with 0 nm polymer and with 100 nm polymer, and the tested spectrum of PCS with 0 nm polymer. (b) Spectral shift; and (c,d): (c) RI sensitivity $\partial\lambda/\partial n$; (d) Thickness sensitivity $\partial\lambda/\partial t$ at different polymer thickness.

The polymer undergoes RI and/or thickness change when interacting with the vapor molecules, the spectral shift of Fano resonance can be expressed as[10]:

$$\Delta\lambda = (\partial\lambda / \partial n) \bullet \Delta n + (\partial\lambda / \partial t) \bullet \Delta t \tag{5.1}$$

where n and t are the RI and thickness of the polymer. ∂λ/∂n and ∂λ/∂t refer to the RI sensitivity (S_{RI}) and thickness sensitivity (S_t), respectively, which are the intrinsic properties associated with the optical mode of the PCS. The RI sensitivity is calculated by tracking the resonance shift for the PCS structure with a small variation in refractive index of the polymer around 1.4. The RI sensitivity S_{RI} at different polymer thickness is plotted in Figure 5-2(c). S_{RI} increases linearly in the 0-100 nm polymer range. S_{RI} reaches 115 nm/RIU with 250 nm polymer and saturates when thickness increases beyond 250 nm.

The thickness sensitivity S_t is plotted in Figure 5-2(d). S_t has high value at small polymer thickness and drops drastically when thickness increases. When the polymer layer is thicker than 300 nm, the thickness sensitivity is close to zero, meaning that the PCS sensor is not sensitive to the change of polymer thickness any more. In the case of thin polymer coating, the RI sensitivity is lower, but with much higher thickness sensitivity, compared to the thicker polymer case.

We simulated the field distribution for the PCS with 50 nm polymer and 300 nm polymer to represent the thin and the thick polymer, respectively. Field distribution is computed with Meep (FDTD). To evaluate the amount of field energy in the polymer region, we integrated $\varepsilon|E|^2$ in one unit cell along the z axis, which are plotted for the two cases shown in Figure 5-3(a) and Figure 5-3(b), for 50 nm polymer and 300 nm polymer, respectively. The inset figures in Figure 5-3(a) show the $\varepsilon|E|^2$ distribution at the center of the Si PCS in the x-y plane (left) and at the center of the hole in the y-z plane (right), where most of the field energy is concentrated in the high refractive index Si region. The integrated $\varepsilon|E|^2$ has the maximum value at the two interfaces of the Si slab, and decay exponentially when moving away from the Si slab interfaces to the polymer layer or buried oxide layer.

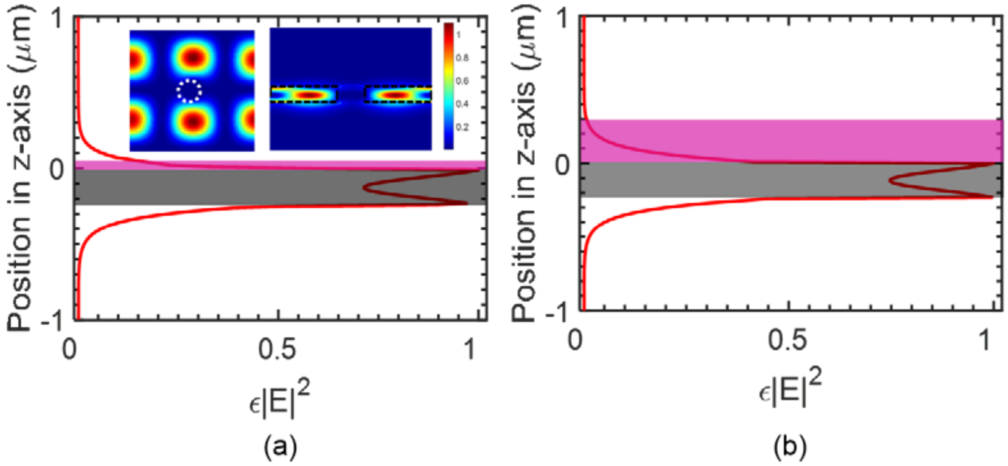

Figure 5-3: Distribution of integrated $\varepsilon|E|^2$ in one unit cell along vertical (z-axis) direction for polymer thicknesses of (a) 50 nm and (b) 300 nm. Pink shaded area is the polymer region and grey shaded area is the Si slab: Shown in the inset of (a) are $\varepsilon|E|^2$ profiles at the center of the PCS in the x-y plane (left) and at the center of the hole in the x-z plane (right), with boundary of hole and Si region shown with dashed lines.

The optical overlap integral *f* in the polymer layer are 4.18% and 11.32% for 50 nm and 300 nm polymer, respectively. We can derive the S_{RI} as 45.3 nm/RIU for 50 nm polymer and 123.4 nm/RIU for 300 nm polymer. The RI sensitivities calculated from field distribution match well with those calculated from spectral resonance tracking, as shown in Figure 5-2(c). As we can see from Figure 5-3(b), there is almost no field outside the 300 nm polymer region, which is the reason for invariant RI sensitivity and near-zero thickness sensitivity when thickness is beyond 300 nm shown in Figure 5-2(d).

The intensity of the evanescent wave above the top surface of the PCS can be written as $I(z) = I_0 \cdot exp(-z/d_p)$, where I_0 is the intensity at the interface between the PCS and the polymer, and d_p is the penetration depth. Intensity I is proportional to $|E|^2$. Penetration depth is around 20 nm and 70 nm for PCS with 50 nm polymer and 300 nm polymer coating, respectively, as shown in Figure 5-4(a) and (b). The larger penetration depth for 300 nm polymer indicates that thicker polymer can pull out more mode intensity out of the Si PCS.

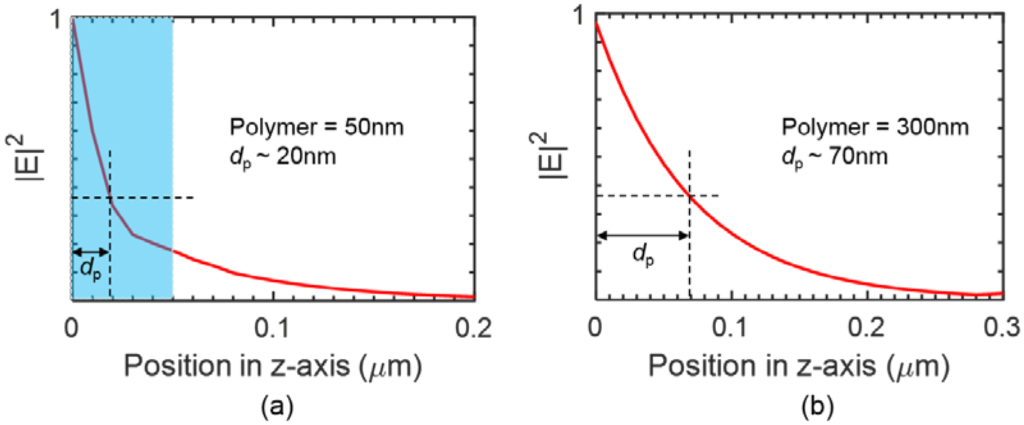

Figure 5-4: Distribution of light intensity above the Si PCS, integrated in one unit cell along vertical (*z*-axis) direction: (a) 50 nm thick polymer case, penetration depth is ~ 20 nm, blue shaded area is the polymer region; (b) 300 nm thick polymer case, penetration depth is ~ 70 nm.

5.3 Integration of PCS with gas chamber

The PCS device on SOI was fabricated with standard EBL process and RIE process, as detailed in section 3.1.1 in chapter 3. Therefore, the fabrication will not be discussed here. We used OV-101 (Ohio Valley Specialty) as vapor sensing polymer. The polymer coating was based on well-developed static coating procedures for gas separation columns[11, 104]. Three PCS devices with the same design were coated with different thicknesses of polymer by controlling the coating solution concentration. The polymer thickness on the three devices is 5 nm (Device #1), 20 nm (Device #2), and 54 nm (Device #3), respectively. We fabricated the PCS with a footprint of 500x500 μm^2 for easier alignment of the incident beam on the device, which can further be reduced down to around 40x40 μm^2 without affecting the quality factor and sensitivity of the PCS.

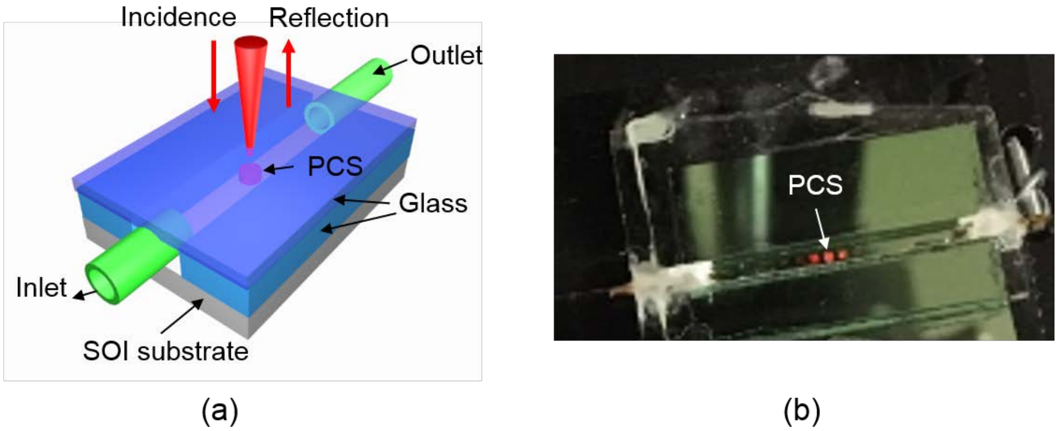

Figure 5-5: (a) A schematic of the vapor sensor device based on the PCS. (b) An image of the device taken by a camera of the smartphone.

A gas chamber made of glass was built on top of the device for polymer static coating and vapor delivery, as schematically shown in Figure 5-5(a), and an image is shown in Figure 5-5 (b) where we can see the PCS inside the gas channel. During static coating, the glass channel is filled with solvent with dissolved polymer, and the outlet is connected to a vacuum pump that evaporate the solvent in a few hours, leaving a conformal polymer coating on the PCS device surface and the interior wall of the glass chamber.

The measured reflection spectrum of Device #3 without polymer coating is shown in Figure 5-2(a). The test setup is shown in Figure 4-1(b) where no polarizers are required. Cross-polarization technique was used to suppress the Fabry-Perot interference induced by the cover glass, and the setup is shown in Figure 4-4. Cross polarization technique can reveal the high Q factor quasi-BIC modes (symmetry-protected modes), as discussed in section 4.2.

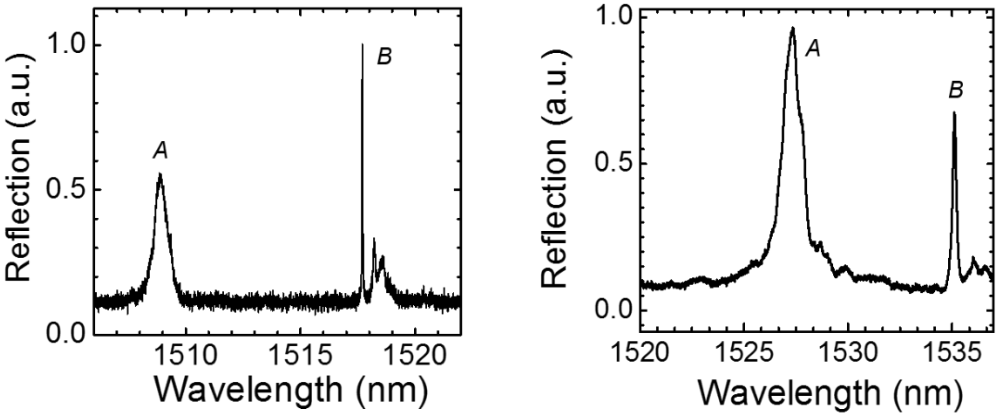

Figure 5-6: Measured reflection spectrum of Device #3 with cross-polarization technique (a) without polymer coating (b) with polymer coating.

The reflection spectrum of Device #3 without polymer coating and with polymer coating are shown in Figure 5-6(a) and Figure 5-6(b), respectively. Mode *A* corresponds to the resonance in Figure 5-2(a). Mode *B* is symmetry-protected mode and it can be observed in the spectrum due to small inherent incident angle of the beam. Mode *A* and *B* redshifted 18 nm after polymer coating, the polymer thickness was derived to be 54 nm based on simulation in Figure 5-2(b). Mode *A* and *B* have similar RI and thickness sensitivities. Each reflection intensity spectrum was fit with a Lorentzian function to obtain the center wavelength of the resonance.

For the chemical-vapor sensing, hexane and ethanol vapors are utilized to represent nonpolar and polar gaseous analyte. Various concentrations of analyte/air mixtures from 0.1 to 30 kppm (thousand parts per million) were injected into the gas chamber by a syringe pump at a flow rate of 0.5 mL/min. Air was used to purge the vapor analyte out of the glass chamber after each analyte sensing run.

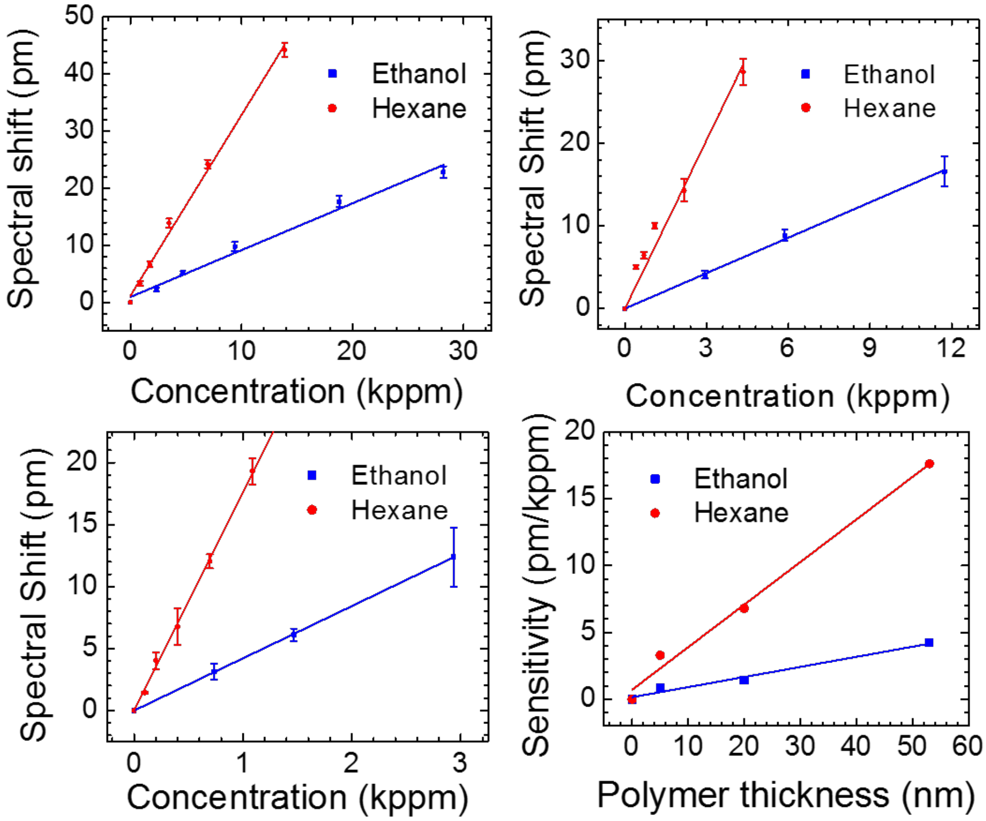

Figure 5-7: Measured spectral shift of the resonant mode at various hexane and ethanol concentration for the PCS coated with polymer of three different thicknesses: (a) Device #1 with 5 nm polymer; (b) Device #2 with 20 nm polymer; and (c) Device #3 with 54 nm polymer. (d) Measured sensitivity of the PCS to hexane and ethanol vapor at different thickness of polymer coating.

We tested mode B because it has higher quality factor, while the sensitivities are similar for mode A and mode B. Each reflection intensity spectrum was fit with a Lorentzian function to obtain the center wavelength of the resonance. The thickness of the polymer coating on Device #1 and #2 were derived to be 5 nm and 20 nm respectively, based on the measured spectral resonance shift after coating.

The spectral shift obtained at equilibrium state for different concentrations of ethanol or hexane vapor for the three devices are plotted in Figure 5-7(a-c). Device #1 has a 5 nm polymer coating, exhibiting a sensitivity of 3.29 pm/kppm for hexane vapor and 0.87 pm/kppm for ethanol vapor, as shown with the linear fitted curves in Figure 5-7(a). Device #2 has a 20 nm polymer coating and the sensitivities of hexane and ethanol vapors increase to 6.81 pm/kppm and 1.43 pm/kppm, respectively, as shown in Figure 5-7(b). The sensitivities of the device #3 with 54 nm polymer coating are fitted to be 17.62 pm/kppm for hexane vapor and 4.22 pm/kppm for ethanol vapor, as shown in Figure 5-7(c). Limited by 1 pm resolution of the tunable laser source, the detection limit for hexane vapor is estimated to be 57 ppm for Device #3.

The sensitivity of hexane vapor is approximately four times higher than that of ethanol vapor for all three devices. This is expected since OV-101 is a nonpolar polymer and has higher solubility for nonpolar vapor molecules such as hexane. Shown in Figure 5-7(d) are the extracted sensitivities for different polymer coating thicknesses. The sensitivities to hexane and ethanol show good linearity with polymer thicknesses in the range of 0 - 50 nm.

The measured sensorgrams with 1.74 kppm hexane and 9.4 kppm ethanol for the device #1 are shown in Figure 5-8(a) and Figure 5-8(b), respectively. The resonant spectrum quickly returns to the baseline after purging with air, indicating that the vapor molecules diffused out of the polymer completely and the polymer is fully regenerated.

The response time of the mode to vapor analytes and air are within 2 seconds. The sensorgrams with 4.34 kppm hexane vapor and 11.74 kppm ethanol vapor for the device #2 with 20 nm polymer coating are shown in Figure 5-8(c) and Figure 5-8(d), respectively. The response time to hexane vapor is around 50 seconds.

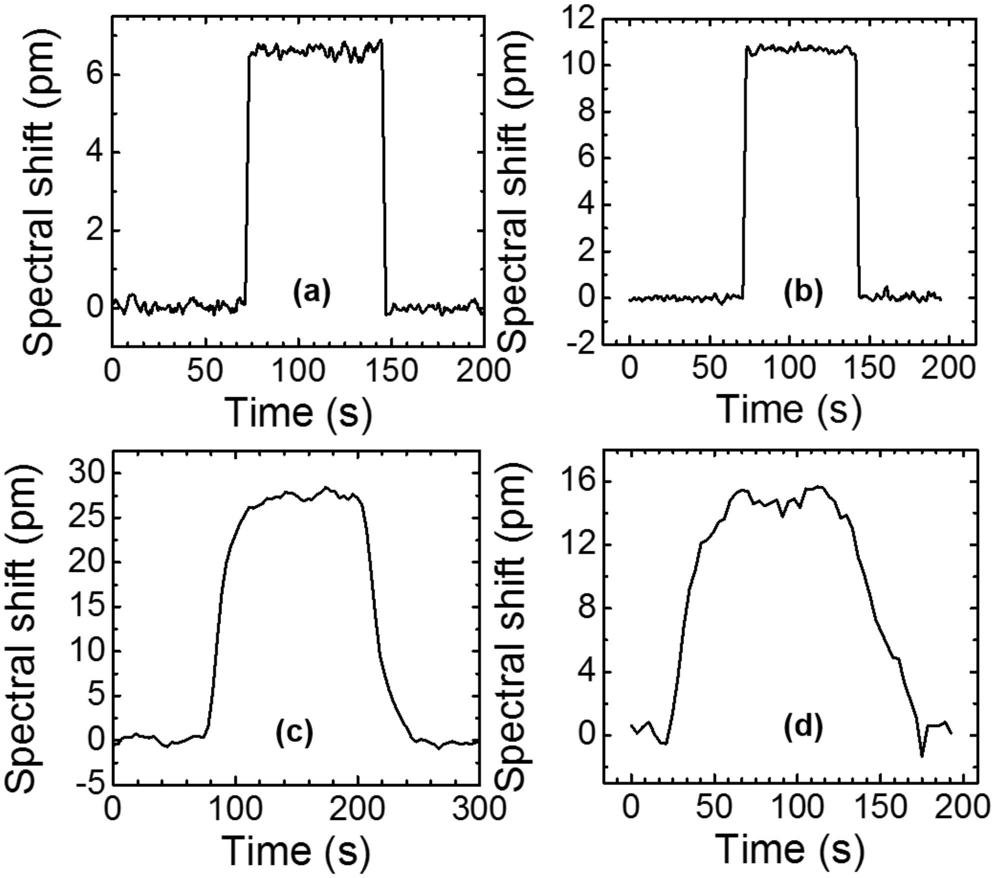

Figure 5-8: Measured sensorgrams of hexane and ethanol vapors for the PCS coated with two polymer thicknesses: (a) 1.74 kppm hexane vapor with 5 nm polymer; (b) 9.4 kppm ethanol vapor with 5 nm polymer; (c) 4.34 kppm hexane vapor with 20 nm polymer; and (d) 11.74 kppm ethanol vapor with 20 nm polymer.

The response time of the three devices to 1.09 kppm and 4.34 kppm hexane vapors are plotted in Figure 5-9(a), while the response time to 2.93 kppm and 11.74 kppm ethanol vapors are shown in Figure 5-9(b). The response time for thicker polymer is longer, because it takes more time for the vapor molecules to diffuse into a thicker polymer to reach the equilibrium. And higher concentration of vapor also requires longer time for the sensor to reach the equilibrium state.

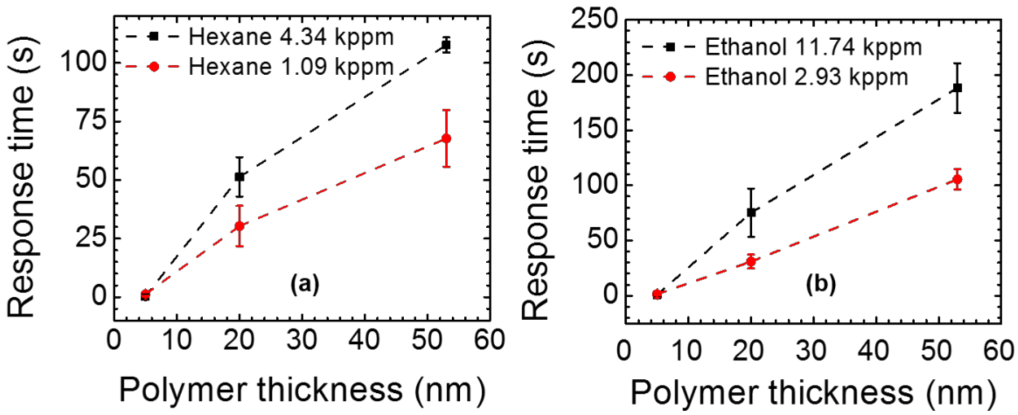

Figure 5-9: Measured response times of the PCS sensor with different thickness of polymer for vapor detection: (a) Hexane vapor with concentrations of 1.09 kppm and 4.34 kppm; and (b) Ethanol vapor with concentrations of 2.93 kppm and 11.74 kppm.

5.4 Integration of PCS with silicon column

In the previous section, the PCS is integrated with a glass chamber using optical glue. The optical glue might contaminate the vapor chamber, and the bonding is also reversible if the sample undergoes high temperature, making it not that reliable for harsh environment. What’s more, the glass gas chamber has large volume. Here we also investigated another configuration to reduce the gas chamber volume for more efficient fluidics. The PCS sensor is transferred onto a glass slide and the fluidic chamber is formed in a piece of silicon wafer. The glass slide and silicon surface can be bonded permanently using anodic bonding process. The silicon column can also be utilized for vapor separation after polymer coating due to different partition coefficient of the vapor to the polymer, providing on-chip gas chromatography (GC).

5.4.1 Silicon column fabrication

Gas chromatography separation columns have been fabricated in silicon substrate by a few groups [105-109]. Deep-reactive-ion-etching (DRIE) or Bosch process are typically used for the fabrication of the micro-columns for microelectromechanical systems (MEMS) applications [110-112].

Table 5-1: Bosch process recipe

Parameter	**Unit**	**Deposition**	**Etch A**	**Etch B**
Process Time	second	2	1.5	2
C_4F_8	sccm	150	--	--
SF_6	sccm	--	150	250
Ar	sccm	30	30	30
Bias voltage	volt	10	250-300	10
Bias Waveform	---	1	1	1
ICP Power	watt	2000	2000	2500
Pressure	mTorr	25	40	60

Bosch process is also called time-multiplexed etching, alternating between a plasma etching step and a polymer deposition step. The polymer passivation layer protects the etched structure from further chemical etching. However, during the etching phase, the directional ions that bombard the substrate remove the passivation layer at the bottom of the trench (but not along the sidewalls). Therefore, the Bosch process can etch deep trenches with straight sidewall profile. The sidewall is not smooth, having some scallops due to isotropic etching in the etching phase. Sulfur hexafluoride (SF_6) gas is typically used for etching, while perfluorocyclobutane (C_4F_8) is used for polymerization.

The deep etching were performed with a Versaline Plasma Processing System. The optimized recipe for the Bosch process is shown in Table 5-1. The etching step is divided into two steps: Etch A and Etch B. The purpose for Etch A is to remove the polymer at the bottom of the trench, therefore a high bias voltage 250-300 Volts is applied to increase physical etching by bombardment. Etch B is for silicon etching with SF_6 gas. The etching is isotropic as plasma etching is dominant.

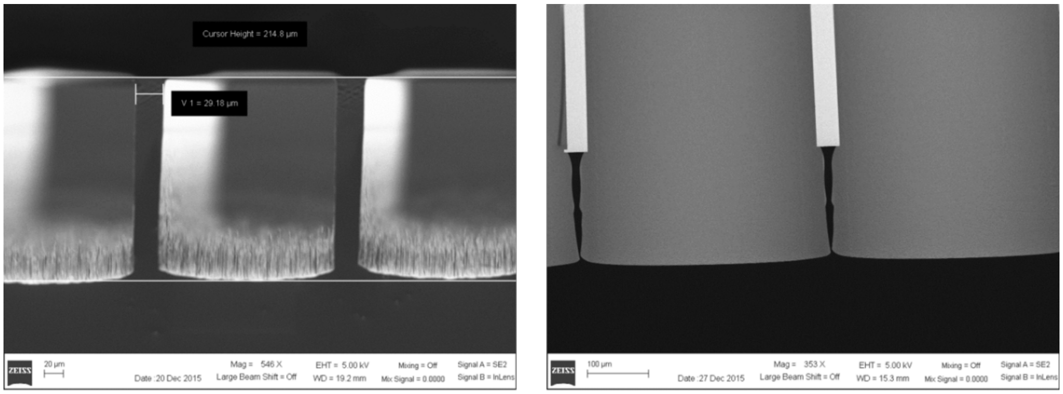

(a) (b)

Figure 5-10: (a) One etched sample with grass at bottom. (b) One etched sample with sidewall being attacked.

A 150 nm thick chromium layer was used as hard mask for the deep silicon etching. The samples were mounted on a 4-inch silicon carrier wafer with around 2-3 µm oxide. Samples were stick to the carrier wafer with Dow Corning 340 silicone heat sink compound to have a good heat transfer from the sample to the carrier wafer. A 10-min oxygen clean was performed between each experiment to remove polymer deposition on the reactor wall. Some calibrations runs with dummy samples were done to optimize the recipe. Here we show two undesired cases in Figure 5-10. The first case, shown in Figure 5-10(a), can be observed when the polymer deposition is too thick at the bottom of the trench to be removed by Etch A step. Micrograss is a term used to describe the formation of micro-columns of silicon due to residual polymer left on the bottom surface after the etch process [113]. The second case, shown in Figure 5-10(b), is because that the thin polymer deposition on the sidewall is too thin to prevent the lateral etching of plasma. Therefore, the polymer deposition time, the etching time, the bias voltage are all critical and adjustable to obtain a straight sidewall without grass formation at the bottom.

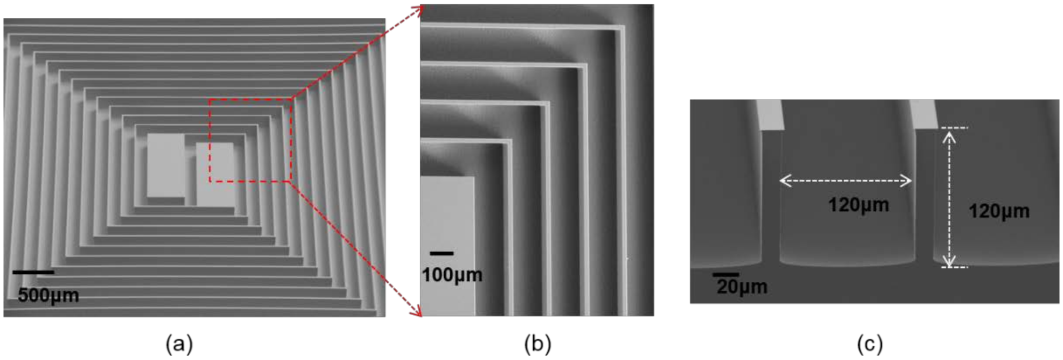

Figure 5-11: (a) SEM angled view of the fabricated silicon column. Column width = 120 um, column depth = 120 um. (b) Zoom in at the center region of the separation columns. (c) Cross sectional view of the columns.

After some calibration runs, the recipe is optimized, as shown in Table 5-1. One fabricated micro-column is shown in Figure 5-11. The column has 25 cm length, and 120x120 μm^2 cross-sectional area.

5.4.2 PCS sensor transfer on glass

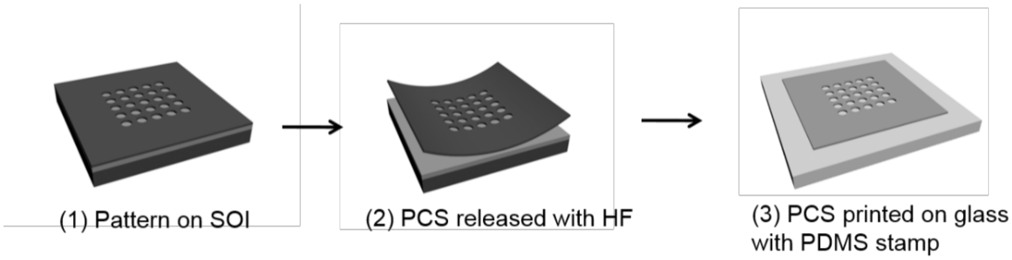

Figure 5-12: Fabrication process flow to transfer Si PCS onto a glass substrate.

The silicon PCS fabricated with SOI substrate can be transferred onto a glass slide. The fabrication process is shown in Figure 5-12. The transfer is done with a PDMS stamp, detailed in one work from Roger's group [114]. The most critical part is the printing of membrane on glass, where the PDMS stamp needs to be peeled off very slowly.

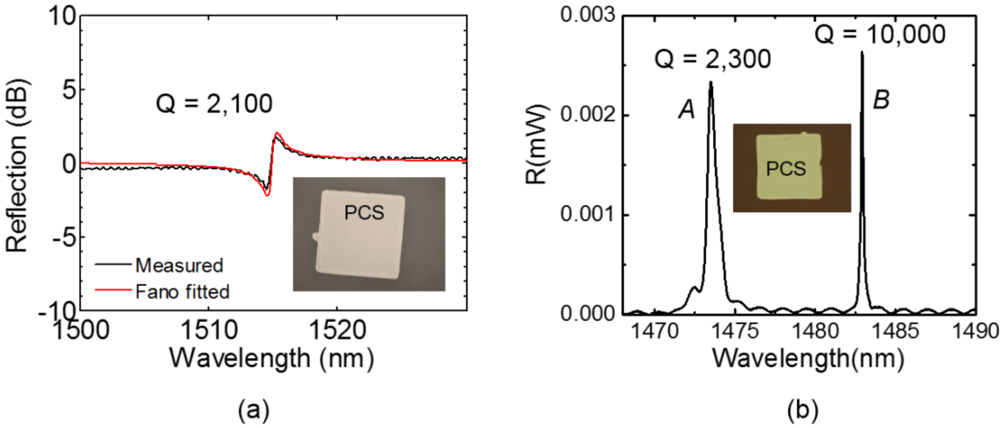

(a)

(b)

Figure 5-13: Measured reflection spectra of the PCS on glass substrate: (a) with index matching gel and parallel polarizers; (b) with cross-polarizer technique. Insets show micrographs of the PCS on glass.

The PCS on glass were measured with two setups. As shown in Figure 5-13(a), the PCS on glass was tested with parallel polarizers. To remove the Fabry-perot oscillation due to the glass substrate, index matching gel was applied at the backside of the glass slide. A quality factor of 2,100 was observed. Figure 5-13(b) shows test result for another PCS on glass with cross-polarizer technique to remove the Fabry-perot background. A quasi-BIC symmetry-protected mode can also be observed with a quality factor of 10,000. The micrograph images of the PCS on glass slide are shown in the insets of Figure 5-13(a) and (b).

5.4.3 Anodic bonding

The silicon column and glass slide can be integrated with anodic bonding. The schematic of home-built setup is shown in Figure 5-14(a). The glass is borofloat glass 33 from SCHOTT, which is a high-quality borosilicate glass with similar coefficient of thermal expansion (CTE) to silicon. It also contains a high concentration of alkali ions. The glass and silicon wafer were cleaned with Pranha solution before the bonding. The bonding were performed at 350 degrees on a hotplate, with a high voltage of 900 voltages for 30 minutes. A detailed description of the setup is in Appendix B.

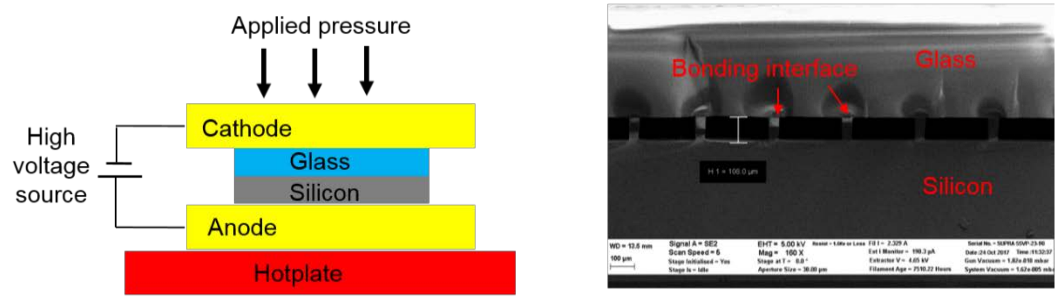

(a) (b)

Figure 5-14: (a) Schematic of the anodic bonding setup. (b) SEM cross-sectional view of one glass bonded to the Si substrate with channels.

The cross-sectional view of the bonded sample is shown in Figure 5-14(b). The silicon column depth is around 106 µm. The bonding interface can be seen, with slight charging effect under SEM.

One PCS sensor integrated with silicon column is shown in Figure 5-15(b). The 300x300 µm^2 PCS is placed on the outlet region of the silicon column, as shown in Figure 5-15(a). The width of the outlet region is 400 µm. An angled view SEM image is shown in Figure 5-15(c).

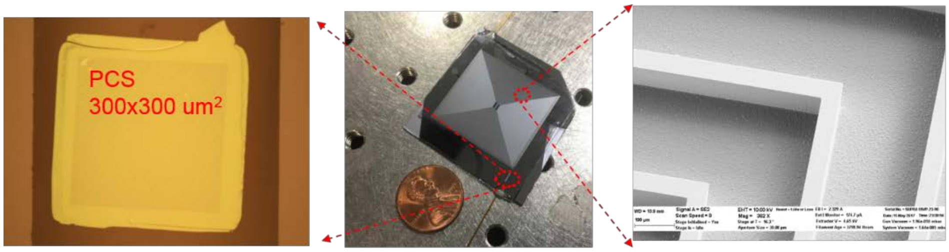

(a) (b) (c)

Figure 5-15: (a) A microscope image of the PCS transferred on the glass substrate. (b) A cellphone image of the Si channels bonded with glass, with a US penny as a size comparison. (c) Angled view SEM image of the Si channels.

5.4.4 Characterization

The integrated sample were firstly characterized with hexane and ethanol vapors, after coating a 20 nm OV-101 polymer. The spectral shift at different concentration of hexane vapor is shown in Figure 5-16(a), with a sensorgram at 8684 ppm shown in the inset. The sensitivity is linear fitted to be 8.3 pm/kppm.

The spectral shift for ethanol vapor is plotted in Figure 5-16(b). The inset shows a sensorgram at 14,670 ppm ethanol concentration. The sensitivity is found to be 3.7 pm/kppm. The sensor shows different sensitivities to hexane and ethanol vapor, with lower sensitivity for polar vapor ethanol due to the non-polar polymer coating.

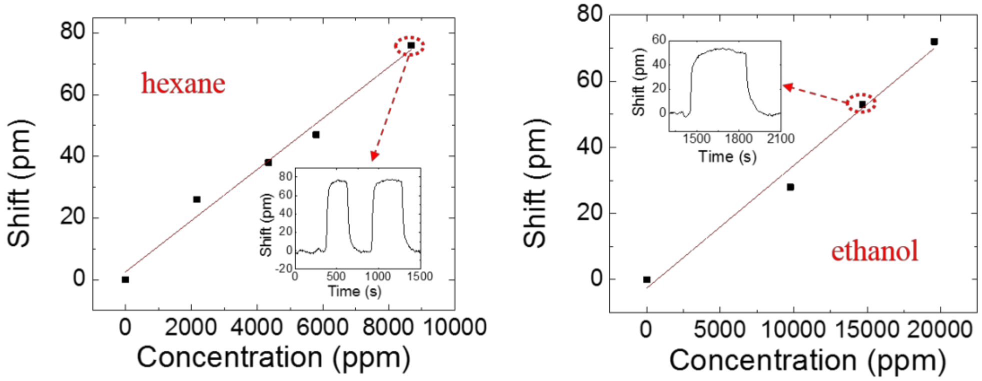

(a)

(b)

Figure 5-16: Measured spectral shift with different concentration of (a) hexane vapor, with a sensorgram for 8,684 ppm shown in the inset; (b) ethanol vapor, with a sensorgram for 14,670 ppm shown in the inset.

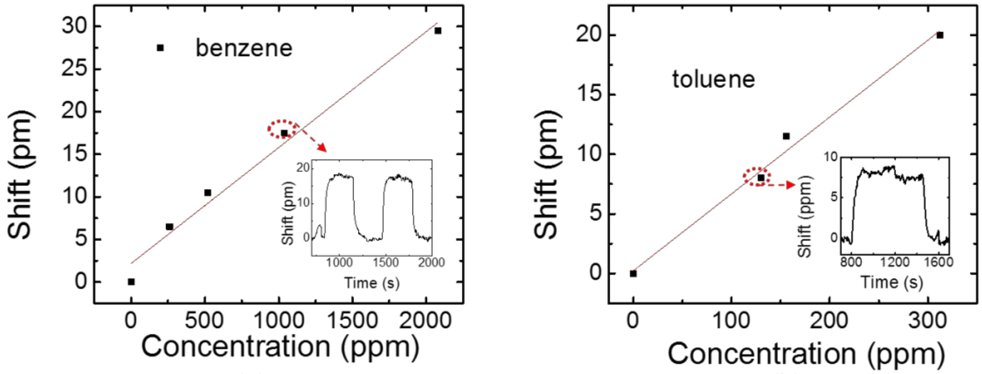

(a)

(b)

Figure 5-17: Measured spectral shift with different concentration of (a) benzene vapor, with a sensorgram for 1,040 ppm shown in the inset; (b) toluene vapor, with a sensorgram for 130 ppm shown in the inset.

We further characterized another two vapors: benzene and toluene. The spectral shift for various concentration of benzene is shown in Figure 5-17(a). The sensitivity is fitted to be 13.6 pm/kppm. The sensitivity for toluene is as high as 64 pm/kppm, as plotted in Figure 5-17(b). This indicates a very strong interaction between the polymer and toluene vapor. Both benzene and toluene are non-polar vapors.

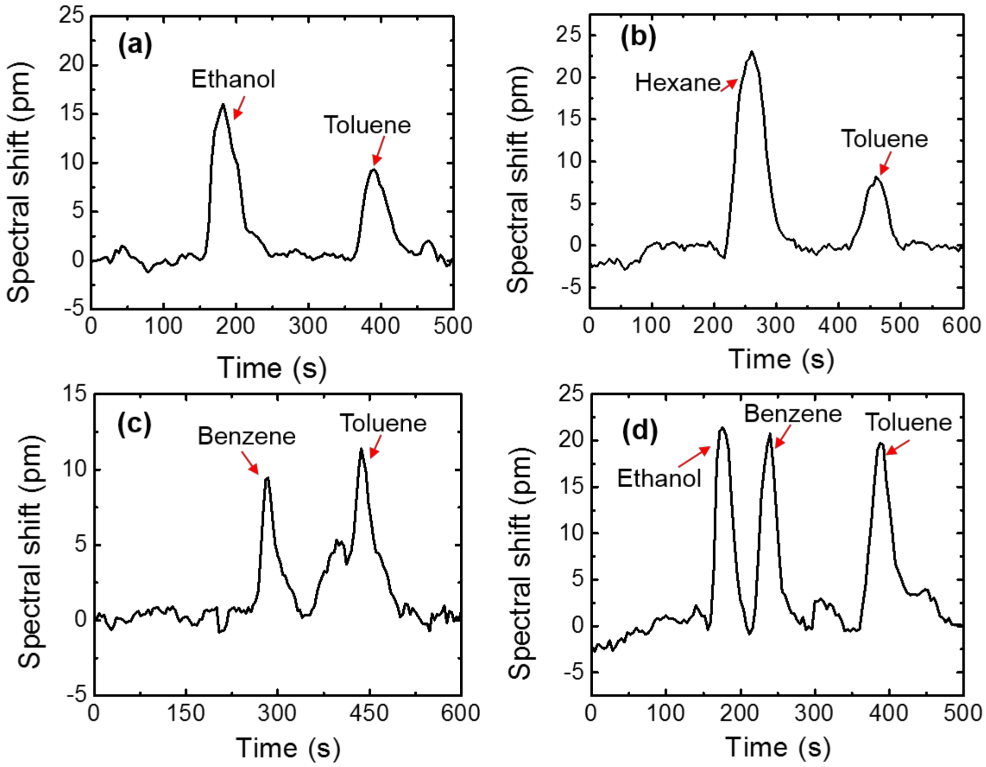

Figure 5-18: Separation of different analytes after passing through the 3 m OV-101 coated column, the vapors are detected with PCS sensor . (a) 5,868 ppm ethanol and 1,872 ppm toluene; (b) 2,894 ppm hexane and 624 ppm toluene; (c) 2,080 ppm benzene and 1,872 ppm toluene; (d) 10,669 ppm ethanol, 3,781 ppm benzene and 3,403 ppm toluene. All the analytes are injected at 0 second.

To study the vapor separation by using the integrated column/PCS, vapor mixture is injected into the column. The chromatograms for different vapor mixtures are shown in Figure 5-18. The mixture of vapors are injected at 0 second. The carrier flow (air) is set at 0.5 mL/min. As shown in Figure 5-18(d), ethanol, toluene, and benzene can be separated well after a 3-m integrated column. Further optimization of the injection volume, column fabrication process and coating process can increase the vapor separation efficiency.

5.5 Summary

Free-space coupled optical vapor sensor on silicon chip was demonstrated based on compact 2D defect-free Fano resonance PCS cavities. The impact of the polymer coating thickness were investigated theoretically and experimentally. A linear dependence of the sensitivities for the polymer thickness less than 54 nm, and reaching saturation values for polymer thickness greater than 300 nm, are associated with the engineered Fano resonance field distributions at surface of the PCS. A detection limit of 57 ppm to hexane vapors was observed for the sensor with 54 nm polymer coating, which is mainly limited by the intrinsic spectral resolution of the measurement setup. There exists a trade-off between the sensitivity and the response time. Thicker polymer tends to have higher sensitivity but responds much slower to the vapors. The sensor with non-polar polymer coating showed four times higher sensitivity of the hexane vapor than that of the ethanol vapor.

The PCS sensor has been integrated with silicon column by anodic bonding, providing more reliable bonding and more compact gas chamber. PCS has been transferred onto glass substrate with high quality factor, making it suitable for sensing. The silicon column can also be used for vapor separation, due to different retention time to different vapors.

Unlike the absorption-based sensors, the 2D PCS based vapour sensor does not require the overlap of resonance with the absorption peak of vapors, therefore it can be used to detect multiple vapors and offers more flexibility in design, and larger tolerance in fabrication. Compared to other resonance-based PCS vapor sensors, lower detection limit was achieved here by incorporating a sensitive polymer coating layer on the PCS surface. The sensor can operate with free-space light beam, with more tolerance for the alignment of the beam onto devices. The platform could be useful in a variety of industrial process control, environmental monitoring and biological research.

Chapter 6

Conclusion and Future Work

6.1 Research summary

6.1.1 Design of PCS for sensing

In the chapter 2 of this dissertation, two different configurations: single layer PCS and double layer PCS, based on bright guided resonance and quasi-BIC modes, have been designed for high *Q* and high sensitivity bulk sensing. For bright guided resonance in single layer PCS on SOI, a design with medium *Q* of 10,000 and medium *S* of 300 nm/RIU was achieved by optimization with RCWA method. To further increase the sensitivity, the single layer PCS can be suspended to have a larger optical overlap integral *f*, because the optical field at both sides of the PCS can interact with the analyte. To further increase the quality factor for the bright guided resonance in single-layer PCS, the radius of the hole can be reduced. However, small holes might pose some challenges in the fabrication.

To achieve high *Q* factor with relatively large hole, we can use some quasi-BIC modes in single-layer PCS. Symmetry-protected BIC modes exist at $\boldsymbol{k} = 0$ due to symmetry mismatch to the external radiation modes and small $\boldsymbol{k}$~0 will excite the quasi-BIC modes. Some non-symmetry-protected BIC modes exist at certain large $\boldsymbol{k}$ value due to the destructive interference between the leakage channels above and below the PCS. These quasi-BIC modes can have extremely high *Q* factor with long lifetime for the photons.

Fabry-perot BIC modes exist when two single layer PCS are brought close to form a double-layer PCS at a critical separation distance d_∞ where two PCS act as two perfect mirrors that trap the light. Quasi-BIC modes will be excited when the separation is off a little from the critical separation d_∞. Suspended double-layer PCS would be challenging to fabricate with good reliability, therefore double layer PCS on SOI substrate with an oxide buffer layer is also discussed for easy implementation.

6.1.2 Fabrication of PCS

In chapter 3 of this dissertation, the fabrication process is discussed in detail. EBL is used to pattern the PCS and RIE etching is employed to have straight sidewall with anisotropic etching. Chlorine and bromine based gas composition Cl_2/HBr is chosen to have high selectivity of silicon to silicon dioxide. Therefore, the buried oxide will be a perfect stop layer for the dry etching.

We can use thermal oxidation to thin down the top silicon layer to the desired thickness. For double layer PCS, the top silicon layer was deposited by LPCVD and annealed to form poly-Si. All the fabrication is compatible with the micro fabrication CMOS process, and the patterning can be made with deep ultraviolet (DUV) lithography for mass production.

6.1.3 Liquid sensing with PCS

In chapter 4 of this work, different configurations were discussed for bulk liquid sensing, including bright guided resonance and symmetry-protected quasi-BIC modes in single layer, and bright guided resonance in double-layer PCS.

Bright guided resonance in 156 nm thick single layer PCS on SOI was utilized to perform bulk liquid sensing. A quality factor of 2,828 and sensitivity of 264 nm/RIU was achieved in liquid, with a detection limit of 2.3×10^{-5} RIU. Ethanol/DI water mixture was chosen to characterize the sensing performance by varying the volume ratio, thus changing the refractive index.

Symmetry protected quasi-BIC modes in single layer PCS was demonstrated for bulk liquid sensing with a high Q factor of 32,000 in air, and 18,000 in water. The sensitivity is measured to be 94 nm/RIU which matches with the simulation result. This design is not the optimal design to achieve high sensitivity, but it is sufficient to be used as a proof-of-concept experiment. The advantage for this non-optimal design is that the thickness of 250 nm is the same as the thickness of the SOI wafer in stock. The fabrication process is much simplified and there is no need to tune the thickness of the top silicon layer.

For bulk liquid sensing with double-layer PCS, one non-optimal design was used partly because of the difficulty to control the thickness of three layer quite tightly. And to have a resonance in our tunable laser source range, the buffer oxide thickness is also taken as a compromised value 160 nm instead of the optimal 120 nm. We demonstrated a quality factor of 2,490 and a sensitivity of 62.8 nm/RIU. The double layer tends to have smaller sensitivity than the single layer PCS because most of the light will be confined in the two PCS labs and also the buffer oxide layer, leaving less optical field above the top silicon PCS to interact with the analyte.

6.1.4 Vapor sensing with PCS

In chapter 5 of the dissertation, a compact optical vapor sensor on silicon chip was demonstrated based on 2D defect-free Fano resonance PCS cavities, which can be used for industrial process control, environmental monitoring and biological research.

For the vapor sensing, we choose single-layer PCS for the test. Both bright guided resonance and symmetry-protected quasi-BIC modes can be used for sensing. A non-polar OV-101 polymer layer was coated onto the PCS device to capture vapor molecules. The polymer thickness or refractive index will be modified by vapor molecule adsorption. We investigated the PCS with different polymer thickness to compare the refractive index sensitivity and thickness sensitivity.

Hexane vapor and ethanol vapor are chosen to represent the non-polar and polar vapor, respectively. We tested the sensitivity and response time of these two vapors with three different thickness of polymer coating. A linear dependence of the sensitivities for the polymer thickness less than 54 nm is found. The sensor showed four times higher sensitivity for the hexane vapor than that for the ethanol vapor, mainly because we were using a non-polar polymer coating as transduction layer.A trade-off between the sensitivity and the response time need to be considered when choosing the thickness of polymer coating. Thicker polymer tends to have higher sensitivity but responds much slower to the vapors.

The PCS sensor is integrated with separation column for a proof-of-concept demonstration of GC system. Different vapors are tested with the integrated sample, exhibiting different retention time from the separation column and different vapor sensitivity for the PCS sensor.

6.2 Suggestions for Future Work

Vapor sensing has been demonstrated in this dissertation. The integration of separation column and PCS sensor has also been demonstrated. Four vapors were utilized to characterize the gas separation and detection. It would be interesting to further test mixtures of multiple volatile organic compounds (VOC) to have an on-chip GC system. To achieve this integration scheme, two aspects need to be considered. The first one is to further optimize the separation column to separate multiple VOCs more efficiently. Polymer coating process might also need to be optimized. Secondly, the PCS sensor need to be improved to have high stability, quick response and high sensitivity in order to test the small concentration of vapors in real time.

Another interesting direction to pursue is the on-chip integration of light source and detector with the sensor. In the experiment of this thesis, the PCS sensor was tested with an expensive and bulky tunable laser, which prevents the sensor being deployed in some field test where a small portable system is preferred. On-chip integration of light source and photo detector has been explored for fluorescence-based sensor [115-117]. However, most of the integration of resonance-based sensor with light source and detector are off-chip integration where the light source and detectors are aligned and assembled with the sensor [118-121]. Using on-chip light emitting diode (LED) as a light source and on-chip photo detector for resonance-based sensor would provide a much cheaper and convenient solution for label-free sensing.

Appendix A

ABBREVIATIONS

2D PCS	Two-dimensional photonic crystal slab
BIC	Bound state in the continuum
BOX	Buried oxide layer
BS	Beam splitter
CMOS	Complementary metal–oxide–semiconductor
DL	Detection limit
DRIE	Deep-reactive-ion-etching
EBL	Electron beam lithography
FDTD	Finite-difference time-domain
FMM	Fourier modal method
FWHM	Full width half maximum
GMR	Guided-mode resonance
LED	Light emitting diode
LPCVD	Low pressure chemical vapor deposition
MEMS	Microelectromechanical systems
OSA	Optical spectrum analyzer
PBC	Periodic boundary conditions
PCS	Photonic crystal slab
PCF	Photonic crystal fiber
PDMS	Polydimethylsiloxane
PhC	Photonic crystals
PML	Perfectly matched layers
Q	Quality factor
RCWA	Rigorous coupled-wave analysis
RI	Refractive index

RIU	Refractive index unit
RIE	Reactive ion etching
SEM	Scanning electron micrograph
SNR	Signal noise ratio
SOI	Silicon-on-insulator
SPR	Surface plasma resonance
S	Sensitivity
S4	Stanford Stratified Structure Solver
TE	Transverse-electric
TM	Transverse-magnetic
TLS	Tunable laser source

Appendix B

ANODIC BONDING SETUP

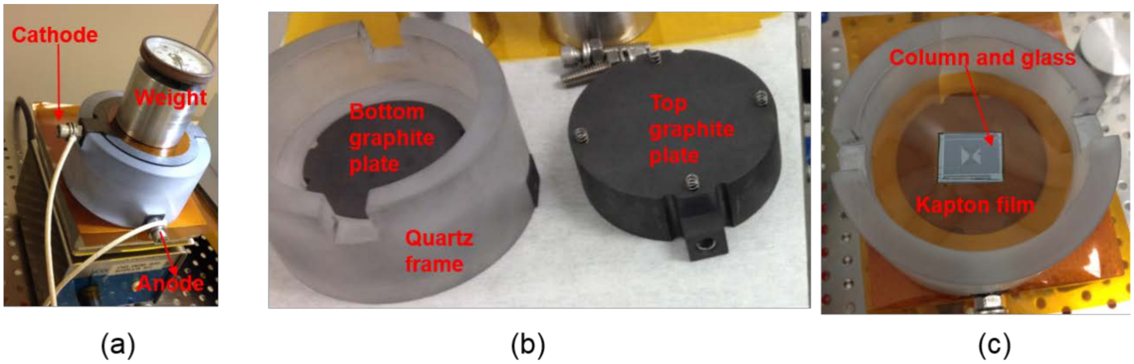

Fig. 1: (a) Home-built anodic bonding setup. (b) Individual parts of the setup. (c) GC column and transferred PCS on glass are placed at the center of the bottom plate, surrounded by a piece of kapton film for insulation.

A home-made anodic bonding setup is shown in Fig. 1. Two graphite plates are used as anode and cathode, respectively (shown in Fig. 1(b)). On the top graphite plate, there are four springs to hold the top plate after being placed on the quartz frame, when a weight is placed on the top plate, it will bring the top plate in contact with the top surface of the samples. These springs will minimize the lateral shift during bonding, because the alignment of the PCS to the sensing chamber is very critical. A kapton film is used to insulate the top plate and bottom plate. The column and transferred PCS sample will be placed at the center of the bottom plate, as shown in Fig. 1(c). The kapton film has been cut with an opening to match with the sample size and shape. Silicon column sample is in contact with the bottom anode graphite plate, and then the borofloat glass with transferred PCS is placed on top of the silicon column with good alignment under microscope. The whole setup was placed on a hotplate for the anodic bonding. The bonding is done with T = 350 C, voltage = 900 V for 0.5 hour. The sample yielded good bonding strength as tested with pressure nitrogen.

Appendix C

PUBLICATIONS

Journal papers

1. **Yonghao Liu**, Shuling Wang, Deyin Zhao, Weidong Zhou, and Yuze Sun. "High quality factor photonic crystal filter at k≈ 0 and its application for refractive index sensing." ***Optics Express*** 25, no. 9 (2017).
2. **Yonghao Liu**, Weidong Zhou, Yuze Sun, "Optical refractive index sensing based on high-Q bound states in the continuum in free-space coupled photonic crystal slabs", ***Sensors,*** 17, 1861 (2017).
3. Shuling Wang, **Yonghao Liu**, Deyin Zhao, Hongjun Yang, Weidong Zhou, and Yuze A. Sun, "Optofluidic Fano resonance photonic crystal refractometric sensors." ***Applied Physics Letters.*** 110, 091105 (2017)
4. Yichen Shuai, Deyin Zhao, **Yonghao Liu**, C. Stambaugh, J. Lawall, Weidong Zhou, "Coupled Bi-layer Photonic Crystal Slab Electro-optic Spatial Light Modulators", *IEEE **Photonics Journal** 9 (2), 1-11, 2017*.
5. Shih-Chia Liu, Deyin Zhao, **Yonghao Liu**, Hongjun Yang, Yuze Sun, Zhenqiang Ma, Carl Reuterskiöld-Hedlund, Mattias Hammar, and Weidong Zhou*, Photonic Crystal Bandedge Membrane Lasers on Bulk Si Substrate, ***Appl. Opt.*** 56, H67-H73 (2017).
6. Cho, Minkyu and Seo, Jung-Hun and Zhao, Deyin and Lee, Jaeseong and Xiong, Kanglin and Yin, Xin and **Yonghao Liu**, et al, "Amorphous Si/SiO2 distributed Bragg reflectors with transfer printed single-crystalline Si nanomembranes", ***Journal of Vacuum Science & Technology B***, 34, 040601 (2016).
7. Liu, Shihchia, Deyin Zhao, Jung-Hun Seo, **Yonghao Liu**, Zhenqiang Ma, and Weidong Zhou. "Athermal photonic crystal membrane reflectors on diamond." ***Photonics Technology Letters**, IEEE* 27, no. 10 (2015): 1072-1075.
8. Yang, Hongjun, Deyin Zhao, Shihchia Liu, **Yonghao Liu**, Jung-Hun Seo, Zhenqiang Ma, and Weidong Zhou. "Transfer Printed Nanomembranes for Heterogeneously

Integrated Membrane Photonics." ***Photonics***, vol. 2, no. 4, pp. 1081-1100. Multidisciplinary Digital Publishing Institute, 2015.

9. Kim, Munho, Wenjuan Fan, Jung-Hun Seo, Namki Cho, Shih-Chia Liu, Dalong Geng, **Yonghao Liu** et al. "Polycrystalline GeSn thin films on Si formed by alloy evaporation." ***Applied Physics Express*** 8, no. 6 (2015): 061301.
10. **Yonghao Liu**, Arvinder Chadha, Deyin Zhao, Jessica R. Piper, Yichen Jia, Yichen Shuai, Laxmy Menon et al. "Approaching total absorption at near infrared in a large area monolayer graphene by critical coupling." ***Applied Physics Letters*** 105, no. 18 (2014): 181105.
11. **Yonghao Liu**, Shuling Wang, Priyanka Biswas, Prithviraj Palit, Weidong Zhou, and Yuze Sun, "Optofluidic photonic crystal vapor sensors", in preparation.

Conference proceedings and presentations

1. **Yonghao Liu,** Wang, Shuling , Weidong Zhou, and Yuze Sun. “High-Q resonance near zero wave vector in photonic crystal slab for label-free sensing”, ***Proc. of SPIE,*** Vol 10108, 2017.
2. **Yonghao Liu**, Deyin Zhao, Weidong Zhou, Yuze Sun, “Refractive index liquid sensing based on bound states in photonic crystal slabs”, ***Frontiers in Optics***, OSA 2017.
3. **Yonghao Liu+**, Priyanka Biswas+, Weidong Zhou, Yuze Sun (+: equal contribution), “Chemical vapor sensing in photonic crystal slabs”, ***Frontiers in Optics***, OSA 2017.
4. Yuze Sun, **Yonghao Liu**, Weidong Zhou, “Free-Space Coupled Photonic Crystal Refractometric Membrane Sensors (Invited)”, ***IEEE Group IV Photonics Conference 2017***, Berlin, Germany (23 - 25, Aug. 2017).
5. Afshin Shamsshooli, Chen Zhang, **Yonghao Liu**, Prithviraj Palit, Yuze Sun, Michael Vasilyev, “Toward a Multi-Species Gas Sensor on a Chip”, ***Frontiers in Optics***, OSA 2017.

6. Wang, Shuling+, **Yonghao Liu+,** Weidong Zhou, and Yuze Sun. (+: equal contribution) “Chemical Vapor Sensing with Fano Resonance Photonic Crystal Slab”, ***NANOSMAT***, May 18 to May 20, 2016.
7. Yang, Hongjun, Deyin Zhao, Shih-Chia Liu, **Yonghao Liu**, Jung-Hun Seo, Matt Hodek, Zhenqiang Ma, John Albrecht, Baxter Moody, and Weidong Zhou. "High-Reflectivity DUV Mirrors Prepared by Direct Sputtering." ***CLEO***: Optical Society of America, 2016.
8. W. D. Zhou, **Yonghao Liu**, X. Ge, X. Li, and S. Fan, “Approach total absorption in critically coupled photonic crystal structures with monolayer 2D materials (Invited)”, ***META’16***, the 7th International Conference on Metamaterials, Photonic Crystals and Plasmonics, Convention & Exhibition Centre, Torremolinos (Malaga), Spain, July 25, 2016 – July 28, 2016.
9. W. D. Zhou, Y. Sun, Z. Ma,L. Menon, **Yonghao Liu**, H. Yang, and D. Zhao, “Hybrid Flexible Membrane Multi-Band Imagers and Optical Membrane Sensors (Invited)”, Symposium BM5: Materials for Bio-integrated Photonic Systems, ***MRS 2016 Fall Meeting***, Nov. 27-Dec. 2, 2016, Boston, Massachusetts, USA
10. Wang, Shuling, **Yonghao Liu**, Deyin Zhao, Yichen Shuai, Hongjun Yang, Weidong Zhou, and Yuze A. Sun. "Optofluidic Double-layer Fano Resonance Photonic Crystal Slab Liquid Sensors." ***CLEO**: Science and Innovations*, Optical Society of America, 2015.
11. Liu, Shihchia, Deyin Zhao, Jung-Hun Seo, **Yonghao Liu**, Zhenqiang Ma, and Weidong Zhou. "Thermally engineered photonic crystal membrane reflectors based on transferred nanomembranes on diamond." ***IEEE Photonics Conference***. 2014.

References

[1] I. M. White and X. Fan, "On the performance quantification of resonant refractive index sensors," *Optics Express,* vol. 16, pp. 1020-1028, 2008/01/21 2008.

[2] X. Fan, I. M. White, S. I. Shopova, H. Zhu, J. D. Suter, and Y. Sun, "Sensitive optical biosensors for unlabeled targets: A review," *Analytica Chimica Acta,* vol. 620, pp. 8-26, 2008.

[3] F. Vollmer and L. Yang, "Label-free detection with high-Q microcavities: a review of biosensing mechanisms for integrated devices," *Nanophotonics,* vol. 1, pp. 267-291, 2012/12// 2012.

[4] M. Lee and P. M. Fauchet, "Two-dimensional silicon photonic crystal based biosensing platform for protein detection," *Optics Express,* vol. 15, pp. 4530-4535, 2007/04/16 2007.

[5] B. Cunningham, B. Lin, J. Qiu, P. Li, J. Pepper, and B. Hugh, "A plastic colorimetric resonant optical biosensor for multiparallel detection of label-free biochemical interactions," *Sensors and Actuators B: Chemical,* vol. 85, pp. 219-226, 2002.

[6] I. D. Block, L. L. Chan, and B. T. Cunningham, "Photonic crystal optical biosensor incorporating structured low-index porous dielectric," *Sensors and Actuators B: Chemical,* vol. 120, pp. 187-193, 2006.

[7] Y. Guo, J. Y. Ye, C. Divin, B. Huang, T. P. Thomas, J. J. R. Baker, and T. B. Norris, "Real-Time Biomolecular Binding Detection Using a Sensitive Photonic Crystal Biosensor," *Analytical Chemistry,* vol. 82, pp. 5211-5218, 2010/06/15 2010.

[8] R. Magnusson, D. Wawro, S. Zimmerman, and Y. Ding, "Resonant Photonic Biosensors with Polarization-Based Multiparametric Discrimination in Each Channel," *Sensors,* vol. 11, p. 1476, 2011.

[9] L. L. Chan, S. L. Gosangari, K. L. Watkin, and B. T. Cunningham, "Label-free imaging of cancer cells using photonic crystal biosensors and application to cytotoxicity screening of a natural compound library," *Sensors and Actuators B: Chemical,* vol. 132, pp. 418-425, 2008.

[10] Y. Sun and X. Fan, "Analysis of ring resonators for chemical vapor sensor development," *Optics Express,* vol. 16, pp. 10254-10268, 2008/07/07 2008.

[11] Y. Sun, S. I. Shopova, G. Frye-Mason, and X. Fan, "Rapid chemical-vapor sensing using optofluidic ring resonators," *Optics Letters,* vol. 33, pp. 788-790, 2008/04/15 2008.

[12] W.-C. Lai, S. Chakravarty, X. Wang, C. Lin, and R. T. Chen, "On-chip methane sensing by near-IR absorption signatures in a photonic crystal slot waveguide," *Optics Letters,* vol. 36, pp. 984-986, 2011/03/15 2011.

[13] M. El Beheiry, V. Liu, S. Fan, and O. Levi, "Sensitivity enhancement in photonic crystal slab biosensors," *Optics Express,* vol. 18, pp. 22702-22714, 2010/10/25 2010.

[14] C. Nicolaou, W. T. Lau, R. Gad, H. Akhavan, R. Schilling, and O. Levi, "Enhanced detection limit by dark mode perturbation in 2D photonic crystal slab refractive index sensors," *Optics Express,* vol. 21, pp. 31698-31712, 2013/12/16 2013.

[15] S. Wang, Y. Liu, D. Zhao, Y. Shuai, H. Yang, W. Zhou, and Y. A. Sun, "Optofluidic Double-layer Fano Resonance Photonic Crystal Slab Liquid Sensors," in *CLEO: 2015*, San Jose, California, 2015, p. STu1F.6.

[16] S. Wang, Y. Liu, D. Zhao, H. Yang, W. Zhou, and Y. Sun, "Optofluidic Fano resonance photonic crystal refractometric sensors," *Applied Physics Letters,* vol. 110, p. 091105, 2017.
[17] Y. Liu, S. Wang, D. Zhao, W. Zhou, and Y. Sun, "High quality factor photonic crystal filter at k~0 and its application for refractive index sensing," *Optics Express,* vol. 25, pp. 10536-10545, 2017/05/01 2017.
[18] Y. Liu, W. Zhou, and Y. Sun, "Optical Refractive Index Sensing Based on High-Q Bound States in the Continuum in Free-Space Coupled Photonic Crystal Slabs," *Sensors,* vol. 17, p. 1861, 2017.
[19] J. D. Joannopoulos, S. G. Johnson, J. N. Winn, and R. D. Meade, *Photonic crystals: molding the flow of light*: Princeton university press, 2011.
[20] J. E. Baker, R. Sriram, and B. L. Miller, "Two-dimensional photonic crystals for sensitive microscale chemical and biochemical sensing," *Lab on a Chip,* vol. 15, pp. 971-990, 2015.
[21] Z. Qiang, H. Yang, L. Chen, H. Pang, Z. Ma, and W. Zhou, "Fano filters based on transferred silicon nanomembranes on plastic substrates," *Applied Physics Letters,* vol. 93, p. 061106, 2008.
[22] Y. Liu, A. Chadha, D. Zhao, J. R. Piper, Y. Jia, Y. Shuai, L. Menon, H. Yang, Z. Ma, and S. Fan, "Approaching total absorption at near infrared in a large area monolayer graphene by critical coupling," *Applied Physics Letters,* vol. 105, p. 181105, 2014.
[23] S. Fan and J. D. Joannopoulos, "Analysis of guided resonances in photonic crystal slabs," *Physical Review B,* vol. 65, p. 235112, 2002.
[24] W. Zhou, D. Zhao, Y.-C. Shuai, H. Yang, S. Chuwongin, A. Chadha, J.-H. Seo, K. X. Wang, V. Liu, Z. Ma, and S. Fan, "Progress in 2D photonic crystal Fano resonance photonics," *Progress in Quantum Electronics,* vol. 38, pp. 1-74, 2014.
[25] U. Fano, "Effects of configuration interaction on intensities and phase shifts," *Physical Review,* vol. 124, p. 1866, 1961.
[26] Y. Shuai, D. Zhao, Z. Tian, J.-H. Seo, D. V. Plant, Z. Ma, S. Fan, and W. Zhou, "Double-layer Fano resonance photonic crystal filters," *Optics Express,* vol. 21, pp. 24582-24589, 2013/10/21 2013.
[27] C. W. Hsu, B. Zhen, A. D. Stone, J. D. Joannopoulos, and M. Soljačić, "Bound states in the continuum," vol. 1, p. 16048, 2016.
[28] S. G. Johnson, S. Fan, P. R. Villeneuve, J. D. Joannopoulos, and L. A. Kolodziejski, "Guided modes in photonic crystal slabs," *Physical Review B,* vol. 60, pp. 5751-5758, 1999.
[29] R. Magnusson and S. S. Wang, "New principle for optical filters," *Applied Physics Letters,* vol. 61, pp. 1022-1024, 1992.
[30] B. Zhen, C. W. Hsu, L. Lu, A. D. Stone, and M. Soljačić, "Topological Nature of Optical Bound States in the Continuum," *Physical Review Letters,* vol. 113, p. 257401, 2014.
[31] C. W. Hsu, B. Zhen, J. Lee, S.-L. Chua, S. G. Johnson, J. D. Joannopoulos, and M. Soljacic, "Observation of trapped light within the radiation continuum," *Nature,* vol. 499, pp. 188-191, 2013.
[32] J. Lee, B. Zhen, S.-L. Chua, W. Qiu, J. D. Joannopoulos, M. Soljačić, and O. Shapira, "Observation and Differentiation of Unique High-Q Optical Resonances Near Zero Wave Vector in Macroscopic Photonic Crystal Slabs," *Physical Review Letters,* vol. 109, p. 067401, 2012.
[33] J. W. Yoon, S. H. Song, and R. Magnusson, "Critical field enhancement of asymptotic optical bound states in the continuum," vol. 5, p. 18301, 2015.

[34] L. Li and H. Yin, "Bound States in the Continuum in double layer structures," *Scientific Reports,* vol. 6, p. 26988, 2016.
[35] V. Liu, M. Povinelli, and S. Fan, "Resonance-enhanced optical forces between coupled photonic crystal slabs," *Optics Express,* vol. 17, pp. 21897-21909, 2009/11/23 2009.
[36] H. H. Nguyen, J. Park, S. Kang, and M. Kim, "Surface plasmon resonance: a versatile technique for biosensor applications," *Sensors,* vol. 15, pp. 10481-10510, 2015.
[37] R. Slavík, J. Homola, and J. Čtyroký, "Single-mode optical fiber surface plasmon resonance sensor," *Sensors and Actuators B: Chemical,* vol. 54, pp. 74-79, 1999.
[38] J. Homola, "Present and future of surface plasmon resonance biosensors," *Analytical and bioanalytical chemistry,* vol. 377, pp. 528-539, 2003.
[39] J. Dostálek, J. Homola, and M. Miler, "Rich information format surface plasmon resonance biosensor based on array of diffraction gratings," *Sensors and Actuators B: Chemical,* vol. 107, pp. 154-161, 2005.
[40] J. Homola, "Surface plasmon resonance sensors for detection of chemical and biological species," *Chemical reviews,* vol. 108, pp. 462-493, 2008.
[41] J. N. Anker, W. P. Hall, O. Lyandres, N. C. Shah, J. Zhao, and R. P. Van Duyne, "Biosensing with plasmonic nanosensors," *Nat Mater,* vol. 7, pp. 442-453, 2008.
[42] D. R. Shankaran, K. V. Gobi, and N. Miura, "Recent advancements in surface plasmon resonance immunosensors for detection of small molecules of biomedical, food and environmental interest," *Sensors and Actuators B: Chemical,* vol. 121, pp. 158-177, 2007.
[43] Y. Sun and X. Fan, "Optical ring resonators for biochemical and chemical sensing," *Analytical and bioanalytical chemistry,* vol. 399, pp. 205-211, 2011.
[44] K. De Vos, I. Bartolozzi, E. Schacht, P. Bienstman, and R. Baets, "Silicon-on-Insulator microring resonator for sensitive and label-free biosensing," *Optics Express,* vol. 15, pp. 7610-7615, 2007.
[45] M. Iqbal, M. A. Gleeson, B. Spaugh, F. Tybor, W. G. Gunn, M. Hochberg, T. Baehr-Jones, R. C. Bailey, and L. C. Gunn, "Label-free biosensor arrays based on silicon ring resonators and high-speed optical scanning instrumentation," *IEEE Journal of Selected Topics in Quantum Electronics,* vol. 16, pp. 654-661, 2010.
[46] B. T. Cunningham, P. Li, S. Schulz, B. Lin, C. Baird, J. Gerstenmaier, C. Genick, F. Wang, E. Fine, and L. Laing, "Label-free assays on the BIND system," *Journal of Biomolecular Screening,* vol. 9, pp. 481-490, 2004.
[47] M. Huang, A. A. Yanik, T.-Y. Chang, and H. Altug, "Sub-wavelength nanofluidics in photonic crystal sensors," *Optics Express,* vol. 17, pp. 24224-24233, 2009.
[48] O. Levi, M. M. Lee, J. Zhang, V. Lousse, S. R. Brueck, S. Fan, and J. S. Harris, "Sensitivity analysis of a photonic crystal structure for index-of-refraction sensing," in *Proc. SPIE*, 2007, p. 64470P.
[49] Y. Liu and H. Salemink, "All-optical on-chip sensor for high refractive index sensing in photonic crystals," *EPL (Europhysics Letters),* vol. 107, p. 34008, 2014.
[50] W.-C. Lai, S. Chakravarty, Y. Zou, Y. Guo, and R. T. Chen, "Slow light enhanced sensitivity of resonance modes in photonic crystal biosensors," *Applied Physics Letters,* vol. 102, p. 041111, 2013.
[51] C. Kang, C. T. Phare, Y. A. Vlasov, S. Assefa, and S. M. Weiss, "Photonic crystal slab sensor with enhanced surface area," *Optics Express,* vol. 18, pp. 27930-27937, 2010/12/20 2010.

[52] Y. Liu and H. Salemink, "All-optical on-chip sensor for high refractive index sensing," *Applied Physics Letters,* vol. 106, p. 031116, 2015.

[53] D. Dorfner, T. Zabel, T. Hürlimann, N. Hauke, L. Frandsen, U. Rant, G. Abstreiter, and J. Finley, "Photonic crystal nanostructures for optical biosensing applications," *Biosensors and Bioelectronics,* vol. 24, pp. 3688-3692, 2009.

[54] D. Yang, S. Kita, F. Liang, C. Wang, H. Tian, Y. Ji, M. Lončar, and Q. Quan, "High sensitivity and high Q-factor nanoslotted parallel quadrabeam photonic crystal cavity for real-time and label-free sensing," *Applied Physics Letters,* vol. 105, p. 063118, 2014.

[55] M. G. Scullion, A. Di Falco, and T. F. Krauss, "Slotted photonic crystal cavities with integrated microfluidics for biosensing applications," *Biosensors and Bioelectronics,* vol. 27, pp. 101-105, 2011.

[56] A. Di Falco, L. O'faolain, and T. Krauss, "Chemical sensing in slotted photonic crystal heterostructure cavities," *Applied Physics Letters,* vol. 94, p. 063503, 2009.

[57] V. Liu and S. Fan, "S4 : A free electromagnetic solver for layered periodic structures," *Computer Physics Communications,* vol. 183, pp. 2233-2244, 2012.

[58] M. Moharam and T. Gaylord, "Rigorous coupled-wave analysis of planar-grating diffraction," *JOSA,* vol. 71, pp. 811-818, 1981.

[59] H. Kogelnik, "Coupled wave theory for thick hologram gratings," in *Landmark Papers On Photorefractive Nonlinear Optics*, ed: World Scientific, 1995, pp. 133-171.

[60] M. Moharam, T. Gaylord, D. A. Pommet, and E. B. Grann, "Stable implementation of the rigorous coupled-wave analysis for surface-relief gratings: enhanced transmittance matrix approach," *JOSA A,* vol. 12, pp. 1077-1086, 1995.

[61] D. Whittaker and I. Culshaw, "Scattering-matrix treatment of patterned multilayer photonic structures," *Physical Review B,* vol. 60, p. 2610, 1999.

[62] K. Yee, "Numerical solution of initial boundary value problems involving Maxwell's equations in isotropic media," *IEEE Transactions on antennas and propagation,* vol. 14, pp. 302-307, 1966.

[63] A. Taflove and S. C. Hagness, *Computational electrodynamics: the finite-difference time-domain method*: Artech house, 2005.

[64] K. S. Kunz and R. J. Luebbers, *The finite difference time domain method for electromagnetics*: CRC press, 1993.

[65] A. F. Oskooi, D. Roundy, M. Ibanescu, P. Bermel, J. D. Joannopoulos, and S. G. Johnson, "Meep: A flexible free-software package for electromagnetic simulations by the FDTD method," *Computer Physics Communications,* vol. 181, pp. 687-702, 2010.

[66] B. Luk'yanchuk, N. I. Zheludev, S. A. Maier, N. J. Halas, P. Nordlander, H. Giessen, and C. T. Chong, "The Fano resonance in plasmonic nanostructures and metamaterials," *Nat Mater,* vol. 9, pp. 707-715, 2010.

[67] V. Lousse, W. Suh, O. Kilic, S. Kim, O. Solgaard, and S. Fan, "Angular and polarization properties of a photonic crystal slab mirror," *Optics Express,* vol. 12, pp. 1575-1582, 2004/04/19 2004.

[68] S. Arnold, M. Khoshsima, I. Teraoka, S. Holler, and F. Vollmer, "Shift of whispering-gallery modes in microspheres by protein adsorption," *Optics Letters,* vol. 28, pp. 272-274, 2003/02/15 2003.

[69] (2017). Available: https://www.jawoollam.com/

[70] B. E. Deal and A. Grove, "General relationship for the thermal oxidation of silicon," *Journal of Applied Physics,* vol. 36, pp. 3770-3778, 1965.

[71] P.-C. Hui, D. Woolf, E. Iwase, Y.-I. Sohn, D. Ramos, M. Khan, A. W. Rodriguez, S. G. Johnson, F. Capasso, and M. Loncar, "Optical bistability with a repulsive optical force in coupled silicon photonic crystal membranes," *Applied Physics Letters,* vol. 103, p. 021102, 2013.

[72] D. Kwong, J. Covey, A. Hosseini, Y. Zhang, X. Xu, and R. T. Chen, "Ultralow-loss polycrystalline silicon waveguides and high uniformity 1x12 MMI fanout for 3D photonic integration," *Optics Express,* vol. 20, pp. 21722-21728, 2012/09/10 2012.

[73] Z. Wang, A. A. Volinsky, and N. D. Gallant, "Crosslinking effect on polydimethylsiloxane elastic modulus measured by custom-built compression instrument," *Journal of Applied Polymer Science,* vol. 131, 2014.

[74] D. J. Campbell, K. J. Beckman, C. E. Calderon, and P. W. Doolan, "Replication and compression of bulk and surface structures with polydimethylsiloxane elastomer," *Journal of Chemical Education,* vol. 76, p. 537, 1999.

[75] L. Xiong, P. Chen, and Q. Zhou, "Adhesion promotion between PDMS and glass by oxygen plasma pre-treatment," *Journal of Adhesion Science and Technology,* vol. 28, pp. 1046-1054, 2014/06/03 2014.

[76] I. Alvarado-Rodriguez and E. Yablonovitch, "Separation of radiation and absorption losses in two-dimensional photonic crystal single defect cavities," *Journal of Applied Physics,* vol. 92, pp. 6399-6402, 2002.

[77] T. Xu, M. S. Wheeler, H. E. Ruda, M. Mojahedi, and J. S. Aitchison, "The influence of material absorption on the quality factor of photonic crystal cavities," *Optics Express,* vol. 17, pp. 8343-8348, 2009/05/11 2009.

[78] G. M. Hale and M. R. Querry, "Optical Constants of Water in the 200-nm to 200-μm Wavelength Region," *Applied Optics,* vol. 12, pp. 555-563, 1973/03/01 1973.

[79] K. A. Tetz, L. Pang, and Y. Fainman, "High-resolution surface plasmon resonance sensor based on linewidth-optimized nanohole array transmittance," *Optics Letters,* vol. 31, pp. 1528-1530, 2006/05/15 2006.

[80] Y. Nazirizadeh, U. Lemmer, and M. Gerken, "Experimental quality factor determination of guided-mode resonances in photonic crystal slabs," *Applied Physics Letters,* vol. 93, p. 261110, 2008.

[81] J.-N. Liu, M. V. Schulmerich, R. Bhargava, and B. T. Cunningham, "Optimally designed narrowband guided-mode resonance reflectance filters for mid-infrared spectroscopy," *Optics Express,* vol. 19, pp. 24182-24197, 2011.

[82] H. Jane and P. T. Ralph, "Optical gas sensing: a review," *Measurement Science and Technology,* vol. 24, p. 012004, 2013.

[83] Y. Sun, J. Liu, G. Frye-Mason, S.-j. Ja, A. K. Thompson, and X. Fan, "Optofluidic ring resonator sensors for rapid DNT vapor detection," *Analyst,* vol. 134, pp. 1386-1391, 2009.

[84] J. T. Robinson, L. Chen, and M. Lipson, "On-chip gas detection in silicon optical microcavities," *Optics Express,* vol. 16, pp. 4296-4301, 2008/03/17 2008.

[85] R. P. Podgorsek and H. Franke, "Optical determination of molecule diffusion coefficients in polymer films," *Applied Physics Letters,* vol. 73, pp. 2887-2889, 1998.

[86] R. P. Podgorsek and H. Franke, "Selective optical detection of aromatic vapors," *Applied Optics,* vol. 41, pp. 601-608, 2002/02/01 2002.

[87] N. Aguirre, L. Pérez, J. Colín, and E. Buenrostro-Gonzalez, "Development of a Surface Plasmon Resonance n-dodecane Vapor Sensor," *Sensors,* vol. 7, p. 1954, 2007.

[88] J. Liu, Y. Sun, and X. Fan, "Highly versatile fiber-based optical Fabry-Pérot gas sensor," *Optics Express,* vol. 17, pp. 2731-2738, 2009/02/16 2009.

[89] K. Reddy and X. Fan, "Self-referenced composite Fabry-Pérot cavity vapor sensors," *Optics Express,* vol. 20, pp. 966-971, 2012/01/16 2012.

[90] K. Reddy, Y. Guo, J. Liu, W. Lee, M. K. Khaing Oo, and X. Fan, "On-chip Fabry–Pérot interferometric sensors for micro-gas chromatography detection," *Sensors and Actuators B: Chemical,* vol. 159, pp. 60-65, 2011/11/28/ 2011.

[91] X. Ning, J. Yang, C. L. Zhao, and C. C. Chan, "PDMS-coated fiber volatile organic compounds sensors," *Applied Optics,* vol. 55, pp. 3543-3548, 2016/05/01 2016.

[92] Y. L. Hoo, W. Jin, H. L. Ho, D. N. Wang, and R. S. Windeler, "Evanescent-wave gas sensing using microstructure fiber," *Optical Engineering,* vol. 41, pp. 8-9, 2002.

[93] T. Ritari, J. Tuominen, H. Ludvigsen, J. C. Petersen, T. Sørensen, T. P. Hansen, and H. R. Simonsen, "Gas sensing using air-guiding photonic bandgap fibers," *Optics Express,* vol. 12, pp. 4080-4087, 2004/08/23 2004.

[94] Ł. Kornaszewski, N. Gayraud, J. M. Stone, W. N. MacPherson, A. K. George, J. C. Knight, D. P. Hand, and D. T. Reid, "Mid-infrared methane detection in a photonic bandgap fiber using a broadband optical parametric oscillator," *Optics Express,* vol. 15, pp. 11219-11224, 2007/09/03 2007.

[95] J. Villatoro, M. P. Kreuzer, R. Jha, V. P. Minkovich, V. Finazzi, G. Badenes, and V. Pruneri, "Photonic crystal fiber interferometer for chemical vapor detection with high sensitivity," *Optics Express,* vol. 17, pp. 1447-1453, 2009/02/02 2009.

[96] D. Monzón-Hernández, V. P. Minkovich, J. Villatoro, M. P. Kreuzer, and G. Badenes, "Photonic crystal fiber microtaper supporting two selective higher-order modes with high sensitivity to gas molecules," *Applied Physics Letters,* vol. 93, p. 081106, 2008.

[97] H. Xu, P. Wu, C. Zhu, A. Elbaz, and Z. Z. Gu, "Photonic crystal for gas sensing," *Journal of Materials Chemistry C,* vol. 1, pp. 6087-6098, 2013.

[98] Y. Zhao, Y.-N. Zhang, and Q. Wang, "Research advances of photonic crystal gas and liquid sensors," *Sensors and Actuators B: Chemical,* vol. 160, pp. 1288-1297, 2011/12/15/ 2011.

[99] J. Jágerská, H. Zhang, Z. Diao, N. L. Thomas, and R. Houdré, "Refractive index sensing with an air-slot photonic crystal nanocavity," *Optics Letters,* vol. 35, pp. 2523-2525, 2010/08/01 2010.

[100] T. Sünner, T. Stichel, S.-H. Kwon, T. W. Schlereth, S. Höfling, M. Kamp, and A. Forchel, "Photonic crystal cavity based gas sensor," *Applied Physics Letters,* vol. 92, p. 261112, 2008.

[101] C. L. C. Smith, J. U. Lind, C. H. Nielsen, M. B. Christiansen, T. Buss, N. B. Larsen, and A. Kristensen, "Enhanced transduction of photonic crystal dye lasers for gas sensing via swelling polymer film," *Optics Letters,* vol. 36, pp. 1392-1394, 2011/04/15 2011.

[102] H. Clevenson, P. Desjardins, X. Gan, and D. Englund, "High sensitivity gas sensor based on high-Q suspended polymer photonic crystal nanocavity," *Applied Physics Letters,* vol. 104, p. 241108, 2014.

[103] D. Pergande, T. M. Geppert, A. v. Rhein, S. L. Schweizer, R. B. Wehrspohn, S. Moretton, and A. Lambrecht, "Miniature infrared gas sensors using photonic crystals," *Journal of Applied Physics,* vol. 109, p. 083117, 2011.

[104] S. Reidy, G. Lambertus, J. Reece, and R. Sacks, "High-Performance, Static-Coated Silicon Microfabricated Columns for Gas Chromatography," *Analytical Chemistry,* vol. 78, pp. 2623-2630, 2006/04/01 2006.

[105] S. Narayanan and M. Agah, "Fabrication and characterization of a suspended TCD integrated with a gas separation column," *Journal of Microelectromechanical Systems,* vol. 22, pp. 1166-1173, 2013.

[106] S. Ali, M. Ashraf-Khorassani, L. T. Taylor, and M. Agah, "MEMS-based semi-packed gas chromatography columns," *Sensors and Actuators B: Chemical,* vol. 141, pp. 309-315, 2009.

[107] G. Lambertus, A. Elstro, K. Sensenig, J. Potkay, M. Agah, S. Scheuering, K. Wise, F. Dorman, and R. Sacks, "Design, fabrication, and evaluation of microfabricated columns for gas chromatography," *Analytical Chemistry,* vol. 76, pp. 2629-2637, 2004.

[108] A. D. Radadia, R. I. Masel, M. A. Shannon, J. P. Jerrell, and K. R. Cadwallader, "Micromachined GC columns for fast separation of organophosphonate and organosulfur compounds," *Analytical Chemistry,* vol. 80, pp. 4087-4094, 2008.

[109] C.-J. Lu, W. H. Steinecker, W.-C. Tian, M. C. Oborny, J. M. Nichols, M. Agah, J. A. Potkay, H. K. Chan, J. Driscoll, and R. D. Sacks, "First-generation hybrid MEMS gas chromatograph," *Lab on a Chip,* vol. 5, pp. 1123-1131, 2005.

[110] A. Ayon, R. Bayt, and K. Breuer, "Deep reactive ion etching: a promising technology for micro-and nanosatellites," *Smart materials and structures,* vol. 10, p. 1135, 2001.

[111] I. R. Saraf, M. J. Goeckner, B. E. Goodlin, K. H. Kirmse, C. T. Nelson, and L. J. Overzet, "Kinetics of the deposition step in time multiplexed deep silicon etches," *Journal of Vacuum Science & Technology B, Nanotechnology and Microelectronics: Materials, Processing, Measurement, and Phenomena,* vol. 31, p. 011208, 2013.

[112] R. L. Bates, P. Stephan Thamban, M. J. Goeckner, and L. J. Overzet, "Silicon etch using SF6/C4F8/Ar gas mixtures," *Journal of Vacuum Science & Technology A: Vacuum, Surfaces, and Films,* vol. 32, p. 041302, 2014.

[113] B. Wu, A. Kumar, and S. Pamarthy, "High aspect ratio silicon etch: A review," *Journal of Applied Physics,* vol. 108, p. 9, 2010.

[114] M. A. Meitl, Z.-T. Zhu, V. Kumar, K. J. Lee, X. Feng, Y. Y. Huang, I. Adesida, R. G. Nuzzo, and J. A. Rogers, "Transfer printing by kinetic control of adhesion to an elastomeric stamp," *Nature materials,* vol. 5, pp. 33-38, 2006.

[115] M. L. Adams, M. Enzelberger, S. Quake, and A. Scherer, "Microfluidic integration on detector arrays for absorption and fluorescence micro-spectrometers," *Sensors and Actuators A: Physical,* vol. 104, pp. 25-31, 2003.

[116] T. Kamei, B. M. Paegel, J. R. Scherer, A. M. Skelley, R. A. Street, and R. A. Mathies, "Integrated hydrogenated amorphous Si photodiode detector for microfluidic bioanalytical devices," *Analytical Chemistry,* vol. 75, pp. 5300-5305, 2003.

[117] E. Thrush, O. Levi, W. Ha, G. Carey, L. J. Cook, J. Deich, S. J. Smith, W. Moerner, and J. S. Harris, "Integrated semiconductor vertical-cavity surface-emitting lasers and PIN photodetectors for biomedical fluorescence sensing," *IEEE Journal of Quantum Electronics,* vol. 40, pp. 491-498, 2004.

[118] M. Paulsen, S. Jahns, and M. Gerken, "Intensity-based readout of resonant-waveguide grating biosensors: Systems and nanostructures," *Photonics and Nanostructures-Fundamentals and Applications,* vol. 26, pp. 69-79, 2017.

[119] Y. Nazirizadeh, U. Bog, S. Sekula, T. Mappes, U. Lemmer, and M. Gerken, "Low-cost label-free biosensors using photonic crystals embedded between crossed polarizers," *Optics Express,* vol. 18, pp. 19120-19128, 2010.

[120] S. Jahns, M. Bräu, B.-O. Meyer, T. Karrock, S. B. Gutekunst, L. Blohm, C. Selhuber-Unkel, R. Buhmann, Y. Nazirizadeh, and M. Gerken, "Handheld imaging photonic crystal biosensor for multiplexed, label-free protein detection," *Biomedical optics express,* vol. 6, pp. 3724-3736, 2015.

[121] D. Gallegos, K. D. Long, H. Yu, P. P. Clark, Y. Lin, S. George, P. Nath, and B. T. Cunningham, "Label-free biodetection using a smartphone," *Lab on a Chip,* vol. 13, pp. 2124-2132, 2013.

Biographical Information

Yonghao Liu is from Hunan, China. He is a student member of OSA and SPIE. He received his Bachelor degree from Huazhong University of Science and Technology in Wuhan, Hubei. He came to UT Arlington in 2012 Fall to join Prof. Weidong Zhou’s group. And he has been co-advised by Prof. Yuze Sun since 2014 Fall.

He has research interest in optical sensors, silicon photonics, optical devices such as light sources, modulators, detectors, gratings, waveguide, etc. He has broad interest in optics, electronics, and semiconductor and will pursue his career in these areas.